DOE/JPL-956766/02
9950-971

SECOND QUARTERLY REPORT

DOE/JPL Contract Co., 956766

Electrical Research on Solar Cells and Photovoltaic Materials

This effort is being conducted persuant to an Interagency Agreement between the Department of Engineering (DOE) and the National Aeronautics and Space Administration (NASA) and in furtherance of work under Prime Contract NAS 7-918 between NASA and the California Institute of Technology.

John Orehotsky
Professor of Engineering
and Physics
Wilkes College
Wilkes-Barre, PA 18766

Project Identification - FSA Reliability and Engineering Science Area
August 31, 1984

DRL No. 213

This work was performed for the Jet Propulsion Laboratory, California Institute of Technology, and was sponsored by the United States Department of Energy through an agreement with the National Aeronautics and Space Administration.

INTRODUCTION

An important objective of the Flat-Plate Solar Cell Array Program is to increase the service lifetime of the photovoltaic modules used for terrestrial energy applications. The current—voltage response characteristics of the solar cells encapsulated in the modules is found to degrade with service time and this degratation places a limitation on the useful lifetime of the modules.

Corrosion appears to be one important physical mechanism that degrades the current-voltage response of the solar cells, and any effort that increases the lifetime by stopping the I-V degradation must address the question of minimizing the corrosion activity associated with the composite metallurgy, anti-reflection coating and p-n semiconductor materials that comprise a typical solar cell.

Minimizing the corrosion activity involves a consideration of both the electrochemical characteristics of the various composite materials in the cells and the ionic conductive properties of the pottant polymer used to encapsulate the cells. Consequently, the most desirable flat-plate array system would involve solar cells consisting of highly polarizable materials with similar electrochemical potentials where the cells would be encapsulated in polymers whose ionic concentrations and mobilities are negligibly small. Specifying a suitable polymer for pottant use is not an easy task since cross-linking agents, plasticizers, absorbed water and other ingredients can contribute significantly to the concentration of ions in the polymer.

Another possible mechanism limiting the service lifetime of the photovoltaic modules is the gradual loss of the electrical insulation characteristics of the polymer pottant due to water absorption or due to polymer degradation from light or heat effects.

A systematic study of the properties of various polymer pottant materials and of the electrochemical corrosion mechanisms in solar cell materials is required for advancing the technology of terrestrial photovoltaic modules. The items of specific concern in the sponsored research activity at Wilkes College involve:

- Electrical and ionic resistivity of various polymer pottant materials when subjected to temperature, humidity, and UV irradiation.
- Water absorption kinetics and water solubility limits in various pottant polymers at selected temperatures and humidities.
- Corrosion characterization of the various metallization systems used in solar cell construction.

QUARTERLY RESULTS/JUNE TO AUGUST, 1984

The work activity in the June, July, and August focused on:

(I) Electrical Properties of polyvinyl butyral (PVB) and ethylene vinyl acetate (EVA) as a function of temperature and humidity.

(II) The kinetics of water absorption and water desorption in EVA.

(III) Ultra violet (UV) light effects on water absorption in PVB and EVA.

(IV) Influence of plasticizer on water absorption in PVB.

(V) Corrosion effects in solar cells.

I. Electrical Properties of EVA and PVB

Experimental Procedure

Selected a.c. and d.c. electrical properties of PVB and EVA are being evaluated as a function of temperature and humidity. The properties being investigated are the:

(i) absorption current (d.c.)

(ii) ionic resistance (d.c.)

(iii) capacitance (a.c.)

(iv) dissipation factor (a.c.)

The experimental procedure consists of encapsulating 200 mesh phosphorous bronze screening as parallel electrodes in PVB and EVA samples. The samples are then immersed in water for several weeks to obtain saturation equilibrium. Previous results (June Progress Report—Figure 2) show that the water saturation equilibrium can be achieved in several weeks when the samples are immersed in water. The samples are then transferred to the temperature/humidity chamber at a selected termperature and at 100% humidity. After equilibrating for an additional twenty-four hours, the electrical properties were measured and then the humidity is lowered. Since the deabsorption kinetics are rapid (Quarterly Progress Report), twenty-four hours are allowed to achieve equilibrium at the lower humidity level and then the electrical properties are measured again. This experimental procedure is repeated at progressively lower humidity levels, and the electrical properties are determined isothermally as a function of the relative humidity. The absorption current and ionic resistivity d.c. electrical properties and the capacitance and dissipation factor a.c. electrical properties were measured.

The capitance and dissipation factor of the samples were measured on a General Radio Capacitance Bridge. The absorption current was evaluated by applying a 390 d.c. voltage driving step to the samples and monitoring the time dependence of the d.c. current response function. When the current response became relatively time independent, the current-voltage characteristics were measured to determine the ionic resistivity.

Experimental Results: PVB -- d.c. Properties

The time dependence of the current response to a step 390 volts d.c. forcing function for a PVB sample at 80°C and at 68°C are presented as a function of the relative humidity in Figures 1 and 2 respectively. An examination of these two figures shows that when the humidity is high (> 90%) the current response obeys a single power law time dependency:

$$I = I_0 t^{-\alpha} \qquad (1)$$

over the entire time frame of the experiment until the current response becomes relatively time independent. At intermediate humidity levels, (40% to 80%), the current response exhibits a two-stage power law time dependency where an exponentially decaying initial transient stage

$$I = I_0 \exp(-t/\tau) \qquad (2)$$

is evident in the data at 68°C for 79%, 67% and 46% humidity levels (Figs. 2 and 3). This initial transient is not apparent in the 77%, and 64% humidity data at 80°C. At low humidities, (< 30%), a single power law time dependency preceeded by a exponentially decaying transient is exhibited (Figs 1 to 4)

when the sample is at both 80°C and 68°C. Tables I and II present a summary of these various time dependencies, their characterizing coefficients and the time range associated with each response curve.

Model for Response Current

A model that accounts for these observed features of the experimental data, suggests that the d.c. current (I) response is the sum of four major contributing current components: I_c, I_p, I_w, and I_i (as shown in Figure 6)

$$I = I_c + I_p + I_w + I_i \tag{3}$$

where the individual mechanisms responsible for these component currents are:

(i) I_c (capacitance charging current)—The samples are simple capacitors and, if they can be represented by a lumped series capacitor—resistor circuit, the d.c. current response I_c to a step d.c. voltage forcing function will be exponentially time dependent

$$I_c = I_{c_0} \exp(-t/\tau) \tag{4}$$

through an R_0C time constant.

$$\tau = R_0 C \tag{5}$$

(ii) I_w (water dipole relaxation charging current)—Orientational polarization of absorped water molecule dipoles in the polymer when subjected to an applied d.c. field is expected to be time sensitive where this sensitivity should yield an exponential time dependent charging current response (I_w):

$$I_w \sim \exp(-t/\tau_w) \tag{6}$$

where τ_w is the dielectric relaxation time. Experimentally, the response current is frequently observed to obey a power law time dependency:

$$I_w = I_{w_o} t^{-\alpha_w} \tag{7}$$

where the α_w coefficient is believed to be related to the orientational mobility of the water molecule dipole in the presence of an electric field. Since absorbed water molecules are not incorporated into the polymer structure by strong primary bonds, the orientation mobility of the water molecular dipole is expected to be large and this large mobility for the dipoles should result in a relatively large value for the α_w coefficient if a power law charging current is the characterizing response. Since dipole orientation mobility is expected to be sensitive to temperature but not to the number of water molecules (n_w) absorbed in the polymer, the coefficient will be temperature (T) dependent but not humidity (H) dependent:

$$\alpha_w = fct(T) \tag{8}$$

$$\alpha_w \neq fct(H) \tag{9}$$

The value of the I_{w_o} factor in the power law expression is dependent on the number of absorbed water molecules and should then be a function of humidity and temperature:

$$I_{w_o} = fct(T, H) \tag{10}$$

(iii) I_p (polymer dipole relaxation charging current) — Polar polymer molecules will also experience a time dependent orientational polarization when subjected to an applied electric field and this time dependence can result in a power law time dependence response current (I_p):

$$I_p = I_{p_o} t^{-\alpha_p} \tag{11}$$

where both α_p and I_{p_o} are expected to be temperature dependent but not humidity dependent:

$$\alpha_p = fct(T) \quad (12)$$

$$\alpha_p \neq fct(H) \quad (13)$$

$$I_{p_o} = fct(T) \quad (14)$$

$$I_{p_o} \neq fct(H) \quad (15)$$

Since polymer molecules are locked into an amorphous crystal structure by strong primary bonds, the orientational mobility of the polymer dipoles is less than that of absorbed water dipoles. The α_p coefficient should then be relatively small compared to α_w

$$\alpha_p < \alpha_w \quad (16)$$

(iv) I_i (ion transport current) — Ions from impurities (absorbed water plasticizer, etc.) or from disassociated polymer, are mobile in an applied field and should initially contribute a time independent current response (I_i):

$$I_i \neq fct(t) \quad (17)$$

where this corrosion type current frequently obeys a Butler-Volmer dependency on the applied voltage V.

$$I_i = 2 I_{i_o} \sinh (FV/2RT) \quad (18)$$

where F is the Faraday equivalent. This dependency for polymer samples is usually most evident at very large applied fields.

For the typical low fields used in this experiment, the Butler-Volmer equation becomes:

$$I_i \simeq I_{i_o} FV/RT \quad (19)$$

$$I_i \simeq \sigma_i V \quad (20)$$

suggesting that an ohmic I-V response is expected where σ_i is the ionic conductance whose magnitude FI_{i_o}/RT can also be expressed as

$$\sigma_i = q\left[n_{H^+}\mu_{H^+} + n_{OH^-}\mu_{OH^-} + n_p\mu_p\right] \tag{21}$$

where n_{H^+} and n_{OH^-} and n_p are the number of ions from ionized water molecules and disassociated polymer molecules respectively, and where μ_{H^+}, μ_{OH^-} and μ_p are the respective mobilities of these ions. The ionic current component then becomes:

$$I_i \simeq q\left[n_{H^+}\mu_{H^+} + n_{OH^-}\mu_{OH^-} + n_p\mu_p\right]V \tag{22}$$

Assuming that the mobilities of all ionic species are approximately equal ($\mu_{H^+} = \mu_{OH^-} = \mu_p \equiv \mu$) , the ionic current becomes

$$I_i \simeq q\mu\left[2k n_w + n_p\right]V \tag{23}$$

where k is the ionization constant of water and n_w is the equilibrium number of impurity water molecules absorbed in the polymer at a given value of relative humidity and temperature. The ionic resistance would then be given by:

$$R_i \simeq \left[2k n_w + n_p\right]^{-1} \tag{24}$$

Thermodynamic considerations require that the equilibrium number of impurity water molecules absorbed in the polymer will be determined by the partial pressure of water vapor in the surrounding ambient so n_w will be proportioned to relative humidity and temperature:

$$n_w = fct\,(T, H) \tag{25}$$

Both the ionic resistance (Eq. 24) and the ionic current (Eq. 23) are then functionally dependent on both temperature and humidity:

$$R_i = fct\,(T, H)\,; \quad R_i \sim H^{-1} \tag{26}$$

$$I_i = fct\,(T, H)\,; \quad I_i \sim H \tag{27}$$

Predictions of Model

When these component currents (Eqs. 4, 7, 11 and 22) are substituted into Equation 3, the time dependent current response to a step d.c. applied voltage becomes

$$I = I_{c_o} \exp(-t/\tau) + I_{w_o} t^{-\alpha_w} + I_{p_o} t^{-\alpha_p} + q[2kn_w + n_p]\mu V \qquad (28)$$

where, at a sufficiently long time, the ionic current alone can be evaluated. This equation as illustrated in Figure 5, is the basis upon which the experiemental results were analyzed.

Some of the contributing current components in this equation may be small enough to be neglected depending upon the temperature and humidity conditions. When the humidity is high, the equilibrium impurity water content in the absorbing polymer may be large enough so that

$$I_{w_o} > I_{p_o} \qquad (29)$$

since I_{w_o} is expected to be humidity dependent (Eg. 10) while I_{p_o} is believed to be insensitive to the humidity (Eg 15). Almost all of the dipole relaxation current is then expected to result from the orientational polarization of water molecules

$$I_{w_o} t^{-\alpha_w} > I_{p_o} t^{-\alpha_p} \qquad (30)$$

and with this assumption, Equation 28 becomes

$$I = I_{c_o} \exp(-t/\tau) + I_{w_o} t^{-\alpha_w} + q\mu[2kn_w + n_p]V \qquad (31)$$

If the resistance of the polymer is low at high humidity levels, the RC time constant τ will be small. When τ is small enough, the exponential

decay term will be too fast to be recorded by the experimental arrangement and the capacitive charging component current can be neglected. Equation 31, the apparent d.c. current response to a step voltage forcing function, will then be given a single power law expression characterized by α_w plus a time independent ionic current contribution:

$$I = I_{w_0} t^{-\alpha_w} + q\mu[2kn_w + n_p]V \qquad (32)$$

This predicted single stage power law response is consistent with the experimental data observed at high humidity (> 90%) levels at both 80 °C and at 68 °C (Figs. 1 and 2) where the slope for each single stage power law response was evaluated numerically and taken to be the α_w coefficient. The approach to a time independent ionic current in Figures 1 and 2 appears to occur after a run time of 100 minutes. Because of the long time involvement, the ionic current was not recorded in great detail. In general, the ionic current was taken to be the current value after 120 minutes of run time. Ionic current values extracted from the experimental data by this procedure, are recorded in Tables I and II.

At intermediate humidity levels where the amount of absorbed water may be sufficiently small, the orientational polarization of both water molecules and polymer molecules may contribute comparably to the dipole relaxation current components. This suggests that at intermediate humidity levels:

$$I_{w_0} \simeq I_{p_0} \qquad (33)$$

The dipole relaxation would then be the sum of the two power law time dependencies:

$$I_{w_0} t^{-\alpha_w} + I_{p_0} t^{-\alpha_p} \qquad (34)$$

and neither contributing factor may be neglected. At these intermediate humidity levels, capacitive charging may be appreciable since the resistance of the polymer sample may be sufficiently large that the RC time constant is long enough to permit a measurement of this current component due to capacitive changing. The total current response to a d.c. step forcing voltage function would then be given by Equation 28 in its full form:

$$I = I_{c_0} \exp(-t/\tau) + I_{w_0} t^{-\alpha_w} + I_{p_0} t^{-\alpha_p} + q\mu [2k n_w + n_p] V$$

and the experimental data should display a exponentially decaying transient followed by a two stage power law time dependency which eventually approaches a time independent ionic current. These features are evident in the intermediate humidity (79, 67, and 46%) data at 68°C shown in Figures 2 and 3. Again, the approach to the ionic current contribution is not recorded in great detail because of a limited time factor. Except for the inability to record the initial transient, the two stage power law feature is also apparent in the 77 and 64% intermediate humidity data at 80°C for PVB (Figure 1).

Equation 16 requires that the first stage power law behavior with its large slope be associated with the orientation polarization of water molecules while the second stage power law behavior results from the orientation polarization of polar polymer molecules. The slope of each first stage power law response is taken to be the α_w coefficent while the slope of each second stage power law response is assigned to the α_p coefficient as shown in Figures 1 & 2.

At low humidity levels where the number of water molecules n_w absorbed in the polymer is probably small, the resistance of the polymer sample and the associated RC time constant of the sample are both expected to be large. The result is a possible measurable capacitance changing current component. Also at low humidities, the dipole relaxation current is expected to be dominated by the relaxation of the polymer molecules.

$$I_{p_0} t^{-\alpha_p} > I_{w_0} t^{-\alpha_w} \tag{35}$$

Equations 28 then simplifies to an expression that contains only one power law time dependence

$$I = I_{c_0} \exp(-t/\tau) + I_{p_0} t^{-\alpha_p} + q\mu [2kn_w + n_p] V \tag{36}$$

where this power law is characterized by the α_p coefficient and where the ionic current contribution is expected to be very small. The experimental data at humidities less than 30% appear to be in reasonable agreement with these predicted features. A single power law time dependency with its assigned α_p slope, is evident at 80°C for a 30% relative humidity (Figure 1) and at 68°C for a 28% relative humidity (Figures 2). An exponential transient is prominent in the 80°/30% data (Figure 4), but not as prominent in the 68°/28% data (Figure 3). With one exception (80°/30%), the apparent time independent ionic current gets progressively smaller as the humidity decreases in both the 80°C and 68°C data. (Figures 1 and 2).

Based upon these predictions resulting from the proposed model for current response in water absorbing polymers, the data in Figures 1 and 2 can be analyzed for the various current components in the response characteristics and the results are presented in Tables I and II for various conditions of temperature and humidity.

Data Analysis Results

The values of the assigned α_w and α_p power law coefficients at various temperature/humidity conditions are shown in Figures 1 and 2 and in Tables I and II. These coefficients are found to be dependent on both humidity and temperature (Fig. 6). The α_p coefficient increases with temperature and decreases with humidity while the α_w coefficient decreases with increasing temperature and humidity. The mechanisms responsible for these dependencies remain a mystery particularly since both α_p and α_w were expected to remain relatively independent of humidity and were expected to increase with temperature.

From the proposed model, the dipole relaxation currents I_{p_o} and I_{w_o} and the ionic current I_i can be obtained from the data. The I_{w_o} and I_{p_o} currents could be most easily extracted from the d.c. response current data (Fig. 1) at 80 ^{o}C for humidity runs where no exponentially decaying transient was apparent in the data. As suggested previously, the ionic current was evaluated from the apparent approach to time independence for the response current, and the results for I_i, I_{w_o}, and I_{p_o} are given in Table I. After properly compensating for the ionic current, the relaxation currents I_{w_o} and I_{p_o} were determined by extrapolation of their respective defining power law dependencies to the t=1 axis in Figure 1. A comparison of these I_{w_o} and I_{p_o} values with the I_i values in Table I clearly shows that the ionic currents are usually almost an order of magnitude smaller than the initial dipole relaxation currents. A plot of these component currents as a function of the relative humidity (Figure 7) shows that: I_{w_o} is dependent on the relative humidity as suggested in Equation 10; I_{p_o} is relatively indepen-

dent of the relative humidity as suggested in Equation 15; and I_i is a strong function of the relative humidity as suggested in Equation 27. The data in Figure 7 suggests that the humidity dependence of I_{w_o} and I_i can be expressed as

$$I_{w_o} = 1.24(10^{-8}) \exp(.12H) \quad (37)$$

$$I_i = 5(10^{-10}) \exp(.15H) \quad (38)$$

The ionic resistance (R_i) of PVB as a function of temperature and humidity was also evaluated, but the evaluation did not involve a simple application of the relationship:

$$R_i = 390 \text{ volts} / I_i \quad (39)$$

To evaluate the ionic resistance, the I-V characteristic response of the PVB samples was determined after the d.c. current response to the 390 volt step decreased to its time independent ionic current value. Typical I-V characteristic curves at 80°C and 68°C for various humidities are shown in Figures 8 and 9; the ohmic response predicted by Equation 23 is apparent. The ionic resistance is determined from the slopes of these curves:

$$R_i = dV/dI \quad (40)$$

and the results at 68°C and 80°C as a function of humidity are shown in Figure 10. These results suggest that the ionic resistance is exponentially related to the relative humidity by the equation:

$$R_i(68°C) = 1.1(10^{10}) \exp(-.078H) \quad (41)$$

$$R_i(80°C) = 1.5(10^{8}) \exp(-.15H) \quad (42)$$

While the ionic resistance was expected (Eq. 26) to be a function of the humidity, the exponential nature of this relationship was unexpected.

The final aspect of the d.c. current data that requires some comment is the features associated with the exponentially time decaying initial transient that is apparent in the data at 68°C (Figures 2 and 3 and Tables II). This exponential behavior was attributed to capacitive charging, and the experimentally determined R_oC time constants (τ):

$$\tau = R_o C \quad (43)$$

are found to be slightly dependant (Fig. 11) on the humidity:

$$\gamma = .033H + .3 \tag{44}$$

This experimentally determined relationship suggests that both the initial resistance (R_o) and the capacitance (C) of the polymer are only slighlty humidity sensitive where R_o is expected to decrease with increasing humidity while C is expected to increase with increasing humidity according to the approximate relationships:

$$R_o \simeq [\alpha H + \beta]^{-1} \tag{45}$$

$$C \simeq \gamma H + \delta \tag{46}$$

Numerical values for the initial resistance can be evaluated from the experimentally determined pre-exponential factors (B) listed in Table II since, for a 390 voltage drive function:

$$R_o = 390 \text{ volts} / B \tag{47}$$

These initial resistance values as a function of humidity for PVB at 68°C are presented in Table II and Figure 12 where a strong humidity dependence of

$$R_o = 1.1(10^9) \exp(-.078H) \tag{48}$$

is apparent. This humidity dependence is considerably stronger than predicted by Equation 45.

Results: PVB - a.c. properties

The capacitance (C) and dissipation factor ($\tan\delta$) for PVB at 68°/95% as a function of frequency are shown in Figure 13. In the 500 to 5KHz range, both C and $\tan\delta$ are highly dependent on the frequency, and PVB appears to a high loss material. The humidity dependence of C and $\tan\delta$ at 68°C and 500Hz are shown in Figure 14. Both C and $\tan\delta$ increase with humidity according to the functional relationships:

$$C(\text{pfds}) = 2.8H + 190 \tag{49}$$

$$\tan\delta = 5(10^{-3})H \tag{50}$$

These capacitance values at 500 Hz and the inital resistance values for PVB at 68°C can be employed to calculate the time constant for charging the capacitive sample. These time constants are compared in Table III with the experimentally measured values. Significant differences exist between the two sets of values.

The differences would be considerably less if the frequency dependance of the capacitive values were taken into account. Even with this possible correction, the calculated and measured values cannot be reconciled because the measured time constants increase with humidity while the calculated time constants decrease with humidity.

Results: EVA - d.c. properties

The time dependence of the d.c. current response in EVA to a step 390 volts forcing function is shown in Figure 15 for various humidity values. The response involves an initial transient (Figure 16) that, except for very short times, is an exponential decay. This exponential decay is followed by a single stage power law time dependence and then by an apparent approach to a time independent current value (Fig. 15).

The two stage power law time dependency apparent in the PVB data at intermediate humidity levels is not evident in EVA. The single stage power law dependency in EVA at all humidity levels can be justified from the basic equation (Eq. 28) for the current response. Assuming that EVA absorbs relatively small amounts of water even at elevated temperatures and humidities, the water dipole relation current contribution (I_{w_o}) will be small compared to I_{p_o} at all humidity levels:

$$I_{w_o} < I_{p_o} \tag{51}$$

From Equation 28, the anticipated current response for EVA would then be given by

$$I = I_{c_o} \exp(-t/\tau) + I_{p_o} t^{-\alpha_p} + I_i \tag{52}$$

which involves a single power law time dependency as evident in the experimental data of Figure 15. The slopes of the power law dependence in Figure 15 can then be equated to the α_p coefficient, and α_p as a function of humidity can be evaluated. The results are presented in both Table IV and Figure 15, and are plotted in Figure 17 where it is apparent that α_p is weakly dependent on the humidity

$$\alpha_p = -1.5(10^{-3})H + .43 \tag{53}$$

Table IV presents the current response behavior, the characterizing time constants and coefficients for the exponential transient and the power law behavior respectively, and the evaluated initial resistances (R_o) and ionic resistance (R_i) as a function of the relative humidity. The time constant (τ) is found to increase as the humidity decreases (Fig. 17)

$$\tau = -.19H + 31 \tag{54}$$

The initial resistance at the various humidity levels is determined from Equation 47. The results expressed as the initial conductance G_o where

$$G_o = 1/R_o \tag{55}$$

are found to be linearly related (Fig. 18) to the relative humidity:

$$G_o = 8(10^{-12})H + 4(10^{-11}) \tag{56}$$

The inital resistance would then be given by

$$R_o = [8(10^{-12})H + 4(10^{-11})]^{-1} \tag{57}$$

which is consistent with expectations (Eq. 26) based upon ionic resistance considerations.

The ionic resistance (R_i) was also evaluated after the termination of the time dependent absorption current. The procedure to obtain R_i was identical to that already described for the PVB data analysis. The characterizing I-V response for EVA at 68° and various humidity levels was also ohmic (Fig. 19) and the slope was used to evaluate R_i. The ionic resistance was found to decrease linearly (Fig. 18) with increasing humidity:

$$R_i = -11.3(10^7)H + 1.4(10^{10}) \tag{58}$$

Results: EVA - a.c. properties

The capacitance (C) and dissipation factor ($\tan\delta$) were measured at 68°C/95% as a function of frequency and at 68°C/500Hz as a function of humidity. The C and $\tan\delta$ for EVA are relatively independent of the frequency (Fig. 13) and are only slightly dependent on the humidity (Fig. 14):

$$C(\mu fds) = 0.15H + 102 \tag{59}$$

$$\tan\delta = 7(10^{-5})H \tag{60}$$

when compared with the humidity dependence of C and $\tan\delta$ for PVB (Fig. 14). Also, the magnitudes of the C and $\tan\delta$ values were considerably smaller for EVA than for PVB, and EVA appears to be a low loss polymer.

These capacitive values and the initial resistance values for EVA at 68°C. and various humidities were used to calculate the RC time constants, and these calculated values were significantly smaller than the measured time constants (Table III). The only apparent agreement between measured and calculated values was in their humidity dependencies.

Summary and Future Work

A summary of the expected and the experimentally observed dependence of R_i, R_o, C, $\tan\delta$, α_ρ, α_ω and τ parameters on humidity is presented in Table V. The thrust of future work will be to resolve some of the unexpected features that are apparent in this comparative summary. Theoretical models for describing the detailed dependence of many of these parameters on humidity are required. Future work must also resolve some of the anomalous features evident in the experimental data as such:

(i) The current response data at 30% humidity in Figure 1 is not systematically consistent with the data at other humidity levels.

(ii) The ionic resistance data at 80°C in Fig. 10 exhibits several disturbed features that may result from possible thermal aging effects.

Another aspect of the future work will be to determine experimentally and theoretically the temperature dependence of these parameters for comparative purposes.

TABLE I

D.C. current response characteristics of PVB at 80°C

RELATIVE HUMIDITY (%)	TIME RANGE (min.)	CURRENT COMPONENTS	TIME DEPENDENCE $I = A\,t^{-\alpha}$		I_{w_0}	I_{p_0}	I_i
			$A\,(=I_{w_0}+I_{p_0}+I_i)$	α			
92	$0<t<100$	$I_w + I_i$	$1.3(10^{-3})$	$.43(=\alpha_w)$	$1.2(10^{-3})$	—	—
	$t>100$	I_i	—	—	—	—	$1.7(10^{-4})$
77	$0<t<10$	$I_w + I_p + I_i$	$2.1(10^{-4})$	$.78(=\alpha_w)$	$1.5(10^{-4})$	—	—
	$10<t<100$	$I_p + I_i$	$6.5(10^{-5})$	$.23(=\alpha_p)$	—	$4.1(10^{-5})$	—
	$t>100$	I_i	—	—	—	—	$2.5(10^{-5})$
64	$0<t<7$	$I_w + I_p + I_i$	$9.5(10^{-5})$	$.85(=\alpha_w)$	$4(10^{-5})$	—	—
	$7<t<100$	$I_p + I_i$	$5.0(10^{-5})$	$.52(=\alpha_p)$	—	$4.6(10^{-5})$	—
	$t>100$	I_i	—	—	—	—	$4(10^{-6})$
30	$20<t<100$	$I_p + I_i$	$9.7(10^{-5})$	$.52(=\alpha_p)$	—	$9(10^{-5})$	—
	$t>100$	I_i	—	—	—	—	$7(10^{-6})$

PVB - 80°C

TABLE II

D.C. current response characteristics of PVB at 68°C

RELATIVE HUMIDITY (%)	TIME RANGE (min.)	CURRENT COMPONENTS	I_i (amps)	R_i ($=390/I_i$) (Ω)	TIME DEPENDENCE $I = At^{-\alpha}$ A (amps)	α	$I = B[\exp(-t/\tau)]$ B (amps) ($=390/R_o$)	$R_o(\Omega)$	τ (min)
95	$0<t<100$ $t>100$	I_w+I_i I_i	$2(10^{-4})$	$1.9(10^6)$	$1.9(10^{-3})$	.56 ($=\alpha_w$)	—	—	—
79	$0<t<4$ $2<t<6$ $10<t<100$ $t>100$	$I_c+I_w+I_p+I_i$ $I_w+I_p+I_i$ I_p+I_i I_i	$1.5(10^{-5})$	$2.6(10^7)$	— $1.4(10^{-4})$ $3.2(10^{-5})$	— 1.0 ($=\alpha_w$) 0.17 ($=\alpha_p$)	$1.4(10^{-4})$ — —	$2.8(10^6)$ — —	2.9 — —
67	$0<t<4$ $2<t<6$ $10<t<100$ $t>100$	$I_c+I_w+I_p+I_i$ $I_w+I_p+I_i$ I_p+I_i I_i	$3(10^{-6})$	$1.3(10^8)$	— $3.9(10^{-5})$ $8.0(10^{-6})$	— 1.1 ($=\alpha_w$) 0.19 ($=\alpha_p$)	$4.3(10^{-5})$ — —	$9.0(10^6)$ — —	2.4 — —
46	$0<t<2$ $2<t<10$ $10<t<100$ $t>100$	$I_c+I_w+I_p+I_i$ $I_w+I_p+I_i$ I_p+I_i I_i	$8(10^{-7})$	$4.9(10^8)$	— $9.4(10^{-6})$ $4.5(10^{-6})$	— 0.72 ($=\alpha_w$) 0.36 ($=\alpha_p$)	$1.4(10^{-5})$ — —	$2.8(10^7)$ — —	1.9 — —
28	$0<t<1$ $2<t<50$ $t>50$	$I_c+I_p+I_i$ I_p+I_i I_i	$4(10^{-7})$	$9.8(10^8)$	— $2.4(10^{-6})$	— 0.45 ($=\alpha_p$)	$4.2(10^{-6})$ —	$9.2(10^7)$ —	1.2 —

PVB – 68°C

ORIGINAL PAGE IS OF POOR QUALITY

TABLE III

MEASURED AND CALCULATED TIME CONSTANTS FOR CAPACITIVE CHARGING OF EVA AND PVB SAMPLES AT 68°C

Humidity (%)	Time Constants (min.)			
	PVB		EVA	
	measured	calculated	measured	calculated
79	2.9	$1(10^{-5})$	17	$3.5(10^{-3})$
67	2.4	$5(10^{-5})$	17	$3.5(10^{-3})$
46	1.9	$1.4(10^{-4})$	23	$4.2(10^{-3})$
28	1.2	$4(10^{-4})$	26	$7.9(10^{-3})$

TABLE III

D.C. current response characteristics of EVA at 68°C

RELATIVE HUMIDITY (%)	TIME RANGE (min.)	CURRENT COMPONENTS	I_i (amps)	R_i ($=390/I_i$) (Ω)	TIME DEPENDENCE $I = At^{-\alpha_p}$ A (amps)	α_p	TIME DEPENDENCE $I = [B][\exp(-t/\tau)]$ B (amps) ($=390/R_o$)	$R_o(\Omega)$	τ (min)
79	$1<t<6$ $6<t<100$ $t>100$	$I_c+I_p+I_i$ I_p+I_i I_i	$\sim 7(10^{-8})$	$\sim 55(10^9)$	— $2.6(10^{-7})$	— .28	$2.2(10^{-7})$ —	$1.8(10^9)$ —	17 —
67	$1<t<6$ $6<t<100$ $t>100$	$I_c+I_p+I_i$ I_p+I_i I_i	$\sim 6(10^{-8})$	$6.5(10^9)$	— $3.0(10^{-7})$	— .36	$2.2(10^{-7})$ —	$1.8(10^9)$ —	17 —
46	$1<t<6$ $6<t<100$ $t>100$	$I_c+I_p+I_i$ I_p+I_i I_i	$4.2(10^{-8})$	$9.2(10^9)$	— $2.3(10^{-7})$	— .37	$1.6(10^{-7})$ —	$2.4(10^9)$ —	23 —
28	$1<t<6$ $6<t<100$ $t>100$	$I_c+I_p+I_i$ I_p+I_i I_i	$\sim 2.5(10^{-8})$		— $1.5(10^{-7})$	— .38	$8.8(10^{-8})$ —	$44(10^9)$ —	26 —
		EVA - 68°C							

TABLE IV

COMPARISON OF HUMIDITY DEPENDENCIES OF SELECTED PROPERTIES OF PVB AND EVA AT 68°C

Property	Expected Dependency	Experimentally Observed Dependencies	
		PVB	EVA
$R_D(\Omega)$	$=[\gamma H+\beta]^{-1}$	$=1.1(10^{9})\exp(-.078H)$	$=[8(10^{-12})H+4(10^{-11})]^{-1}$
$R_I(\Omega)$	$=[\gamma H+\beta]^{-1}$	$=1.1(10^{10})\exp(-.078H)$	$=-1.13(10^{8})H+1.4(10^{9})$
α_w	$\neq f(H)$	?	—
α_p	$\neq f(H)$	$=-6.4(10^{-3})H+.64$	$=-1.5(10^{-3})H+.43$
$T_{(min)}$	$=[\delta H+\eta]/[\gamma H+\beta]$	$=.033H+0.3$	$=-.19H+31$
C (pfds)	$=\delta H+\eta$	$=2.8H+190$	$=0.15H+102$
$\tan\delta$	$=\delta H+\eta$	$=5(10^{-3})H$	$=.7(10^{-4})H$

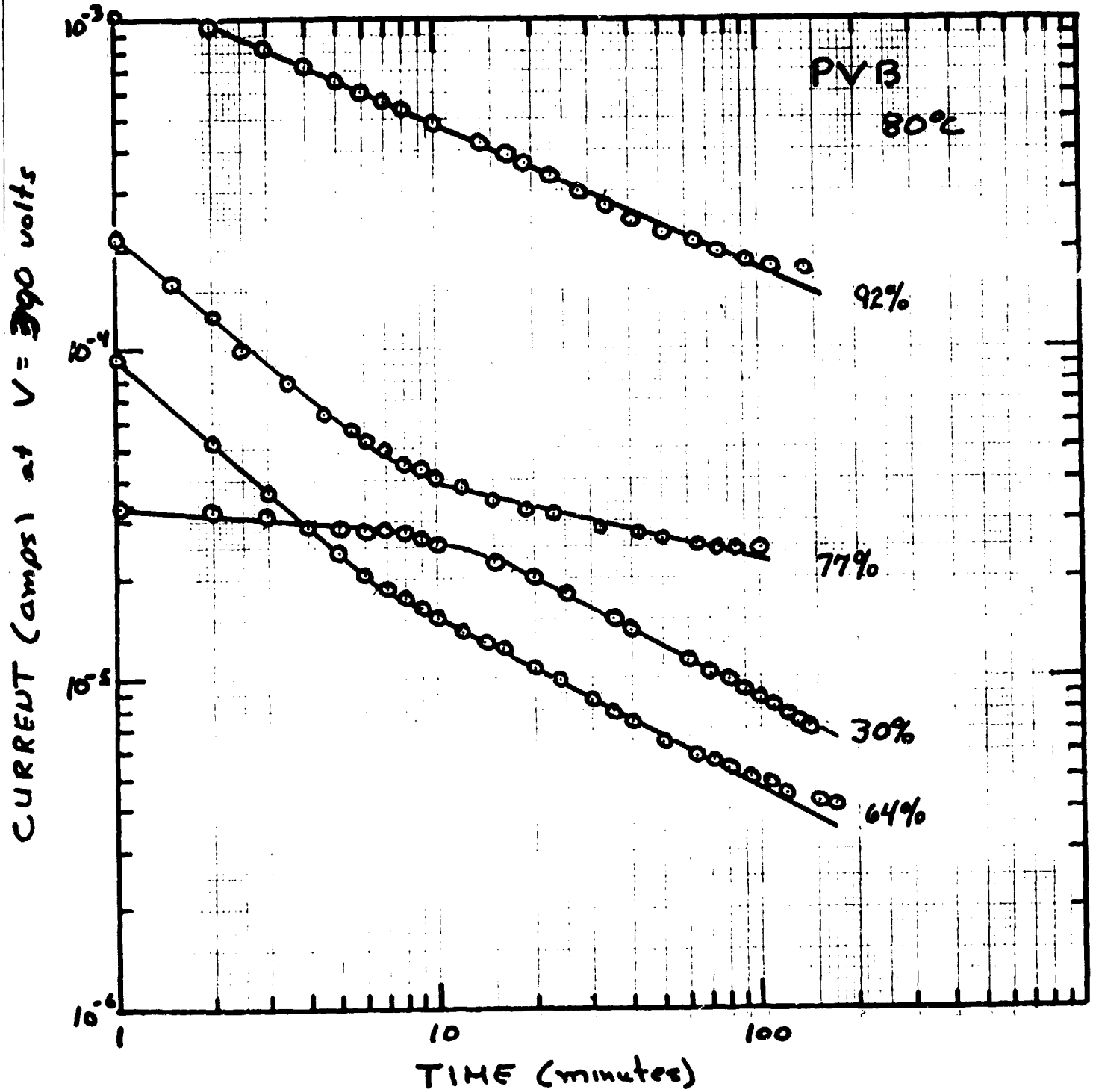

FIGURE 1

Time dependence of the d.c. response current resulting from a 390 volt step forcing function applied to PVB at 80°C and various relative humidity levels.

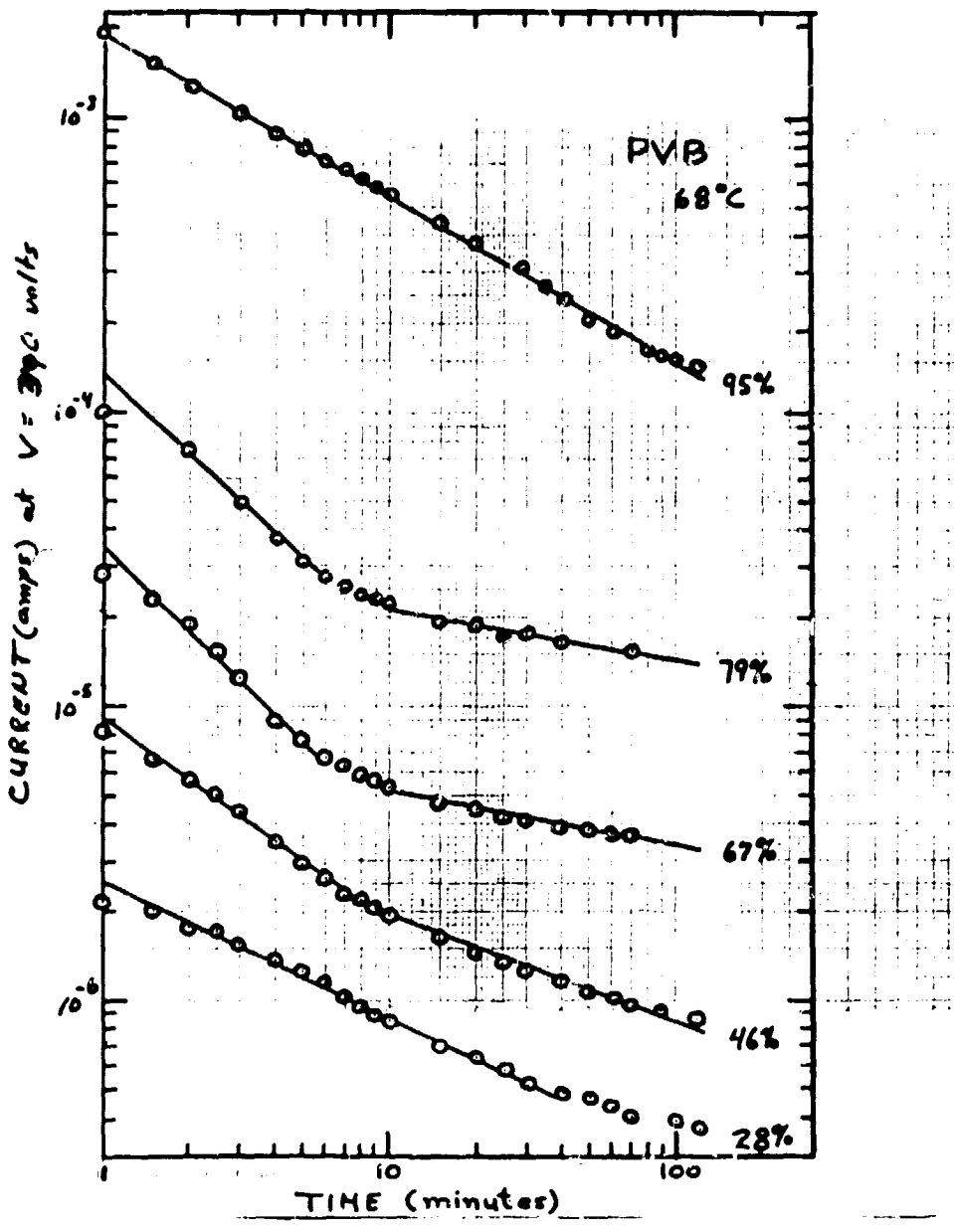

FIGURE 2

Time dependence of the d.c. response current resulting from a 390 volt step forcing function applied to PVB at 68°C and various relative humidity levels.

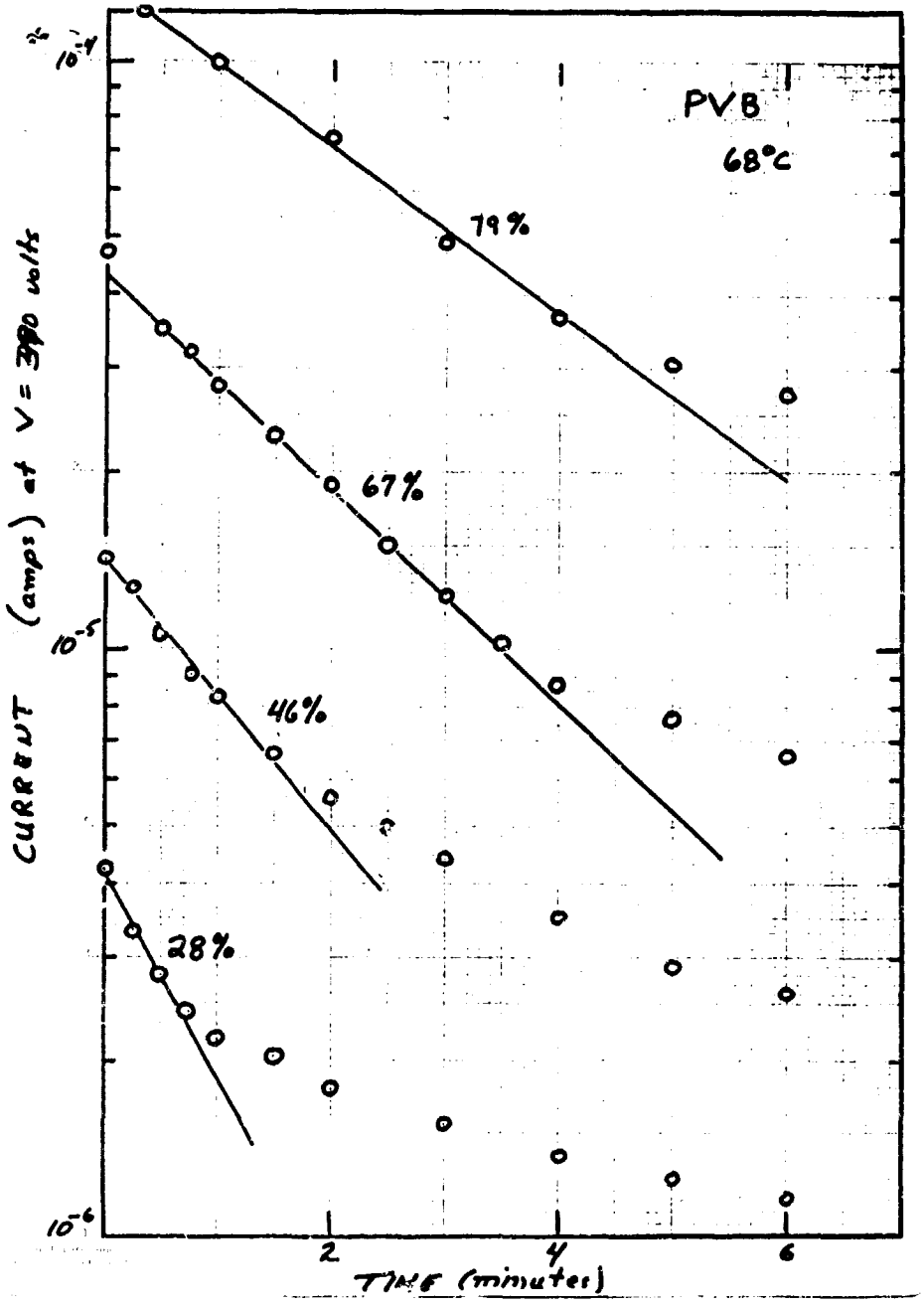

FIGURE 3

Initial transient behavior for the d.c. current response data shown in Figure 2.

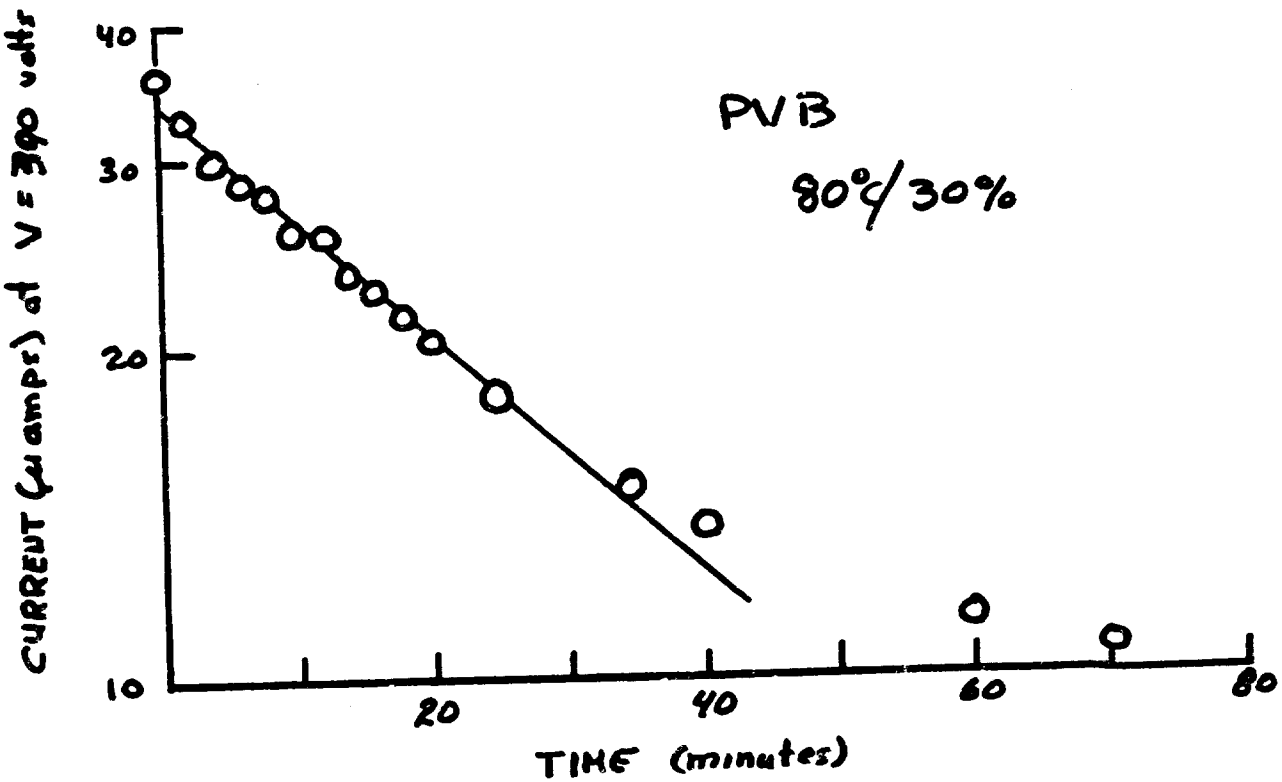

FIGURE 4

Initial transient behavior for the d.c. current response data at 30% relative humidity shown in Figure 1.

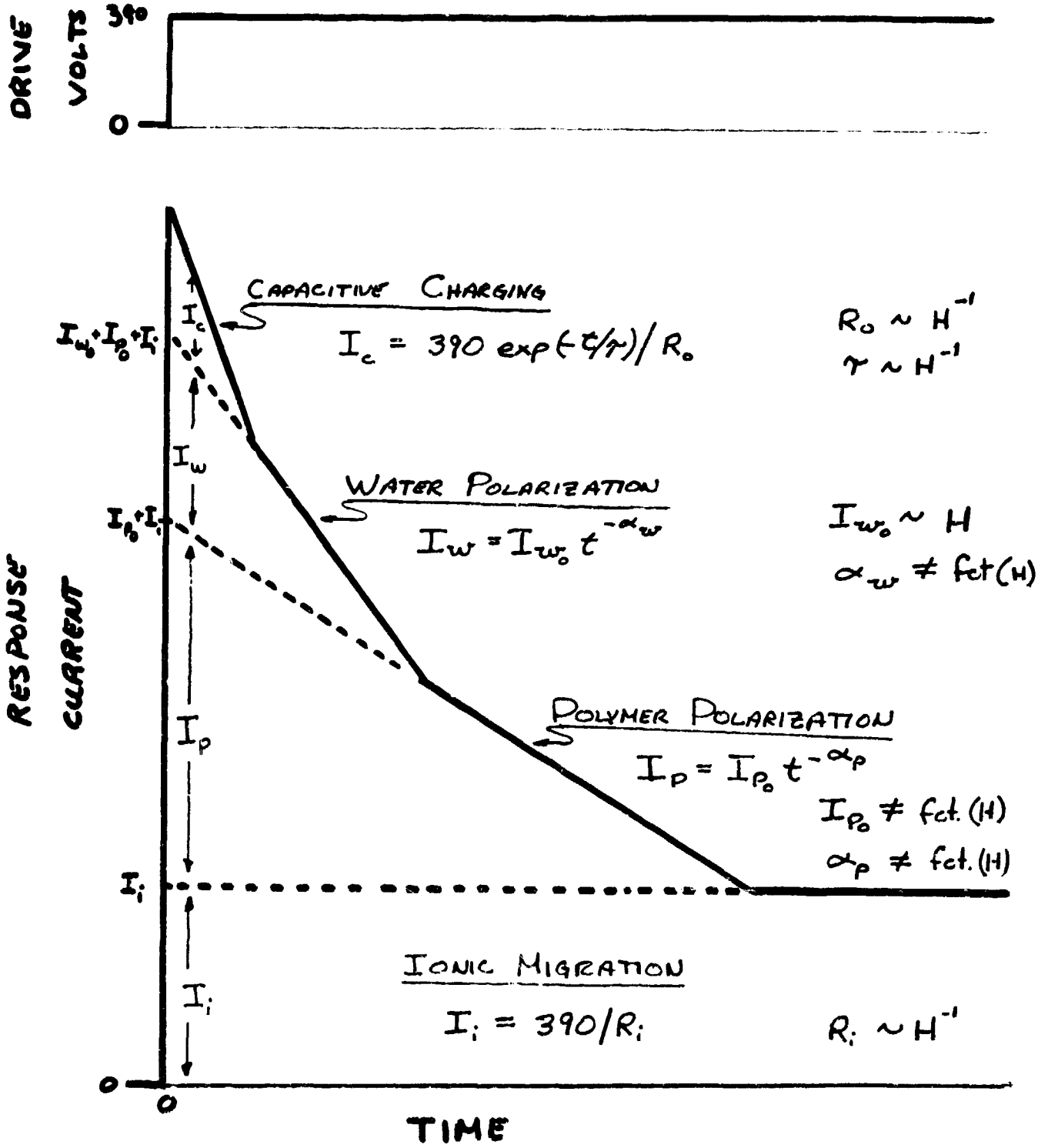

FIGURES

Proposed current response mechanisms and associated time dependencies in a water absorbing polymer when subjected to a 390 d.c. voltage step forcing function.

FIGURE 6

Relative humidity dependence of the coefficients α_p and α_w characterizing the power law d.c. current response data shown in figures 1 and 2.

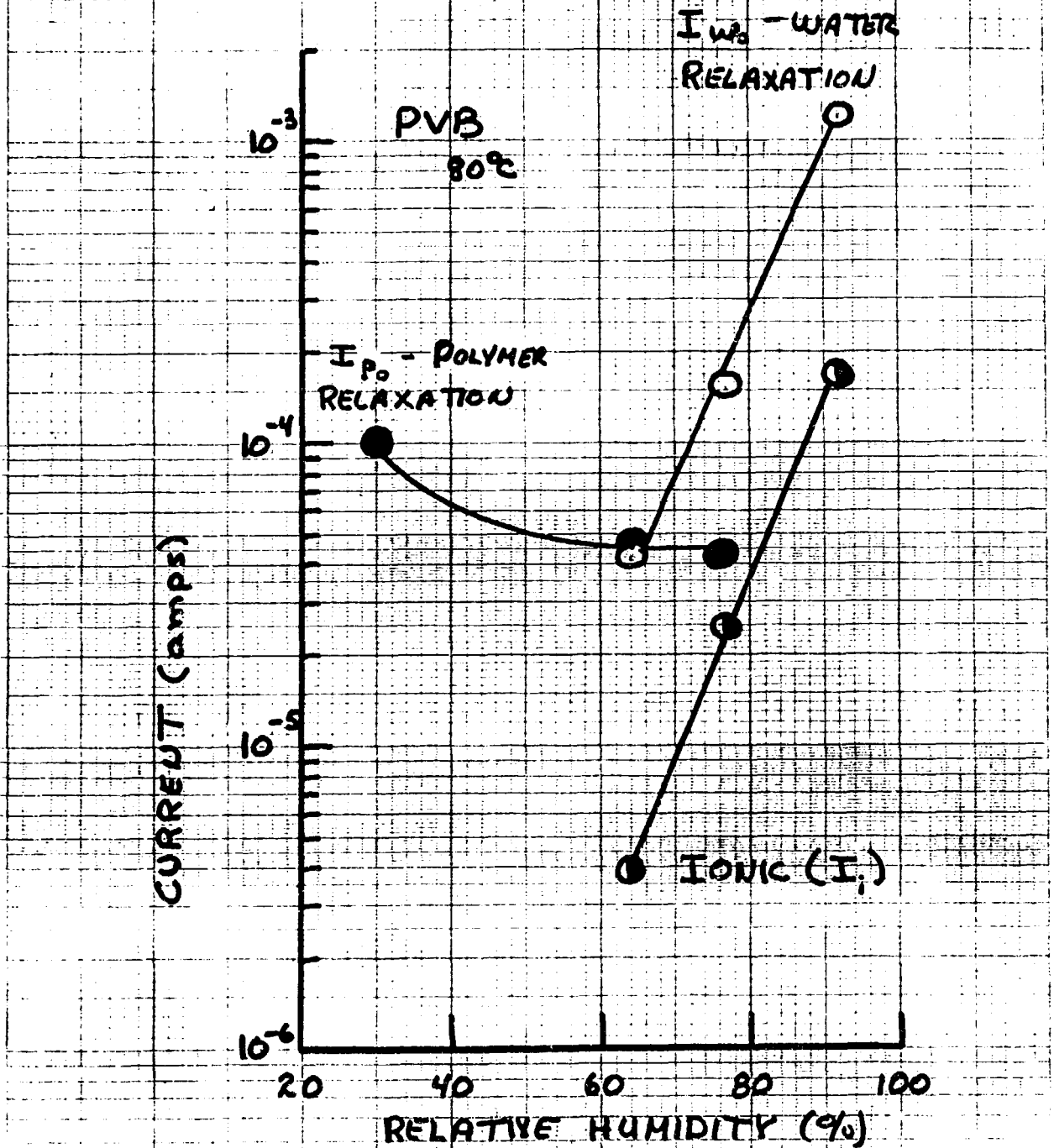

FIGURE 7

Relative humidity dependence of the ionic (I_i), water dipole orientational polarization relaxation (I_{w_o}), and polymer dipole orientation polarization (I_{P_o}) relaxation current contributions to the d.c. current response characteristics of PVB at 80°C.

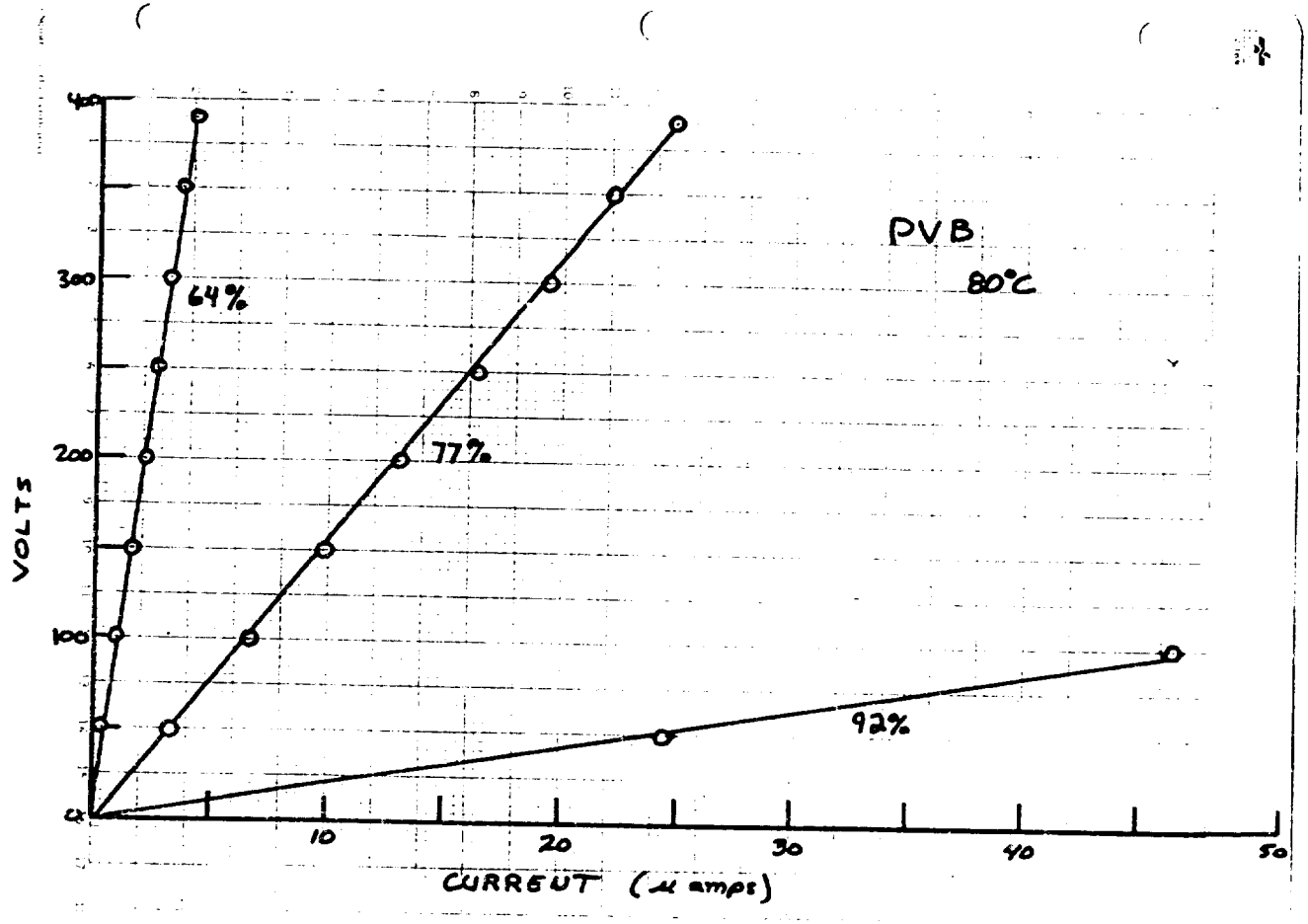

FIGURE 8

Current-voltage characteristics curves for ionic transport in PVB at 80°and various values of the relative humidity.

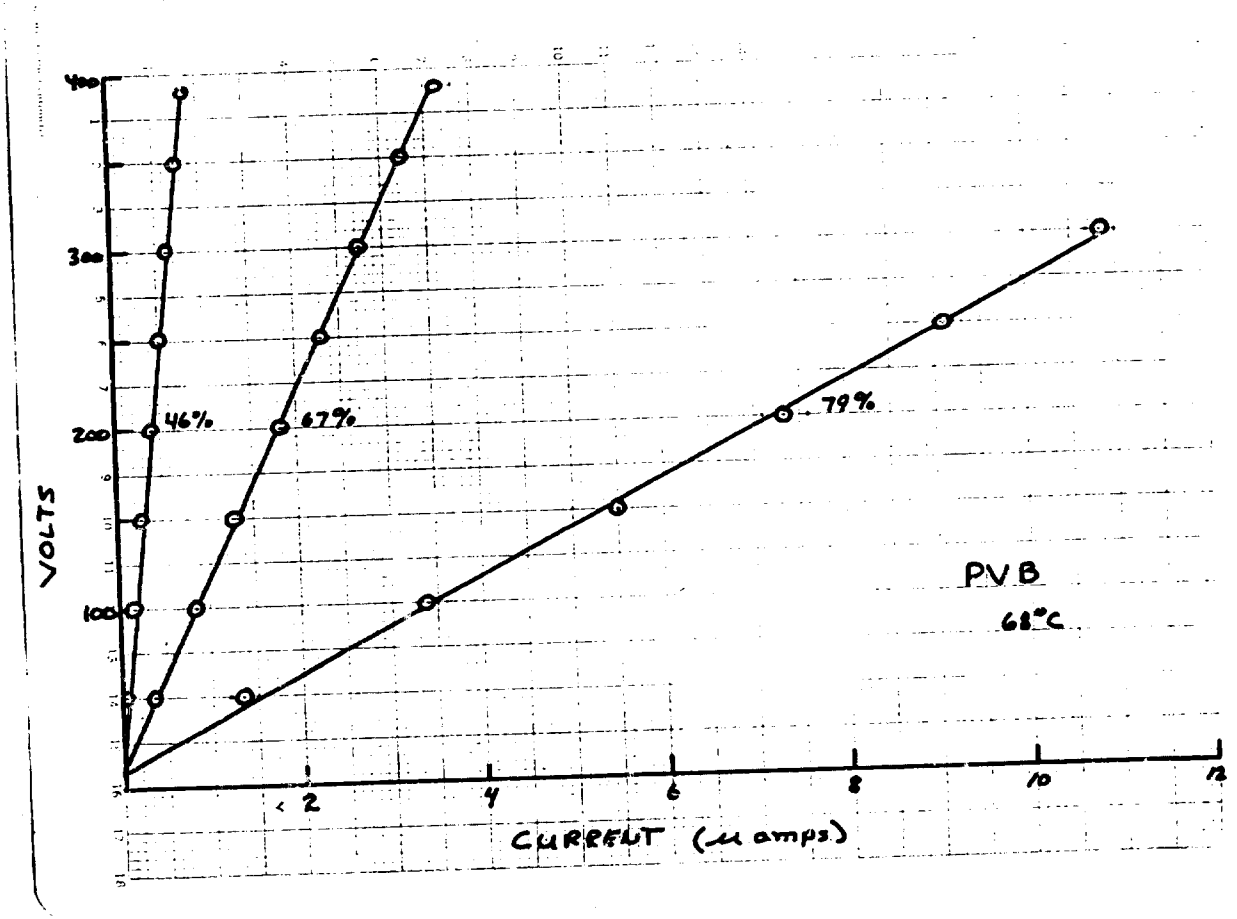

FIGURE 9

Current-voltage characteristics curves for ionic transport in PVB at 68°C and various values of the relative humidity.

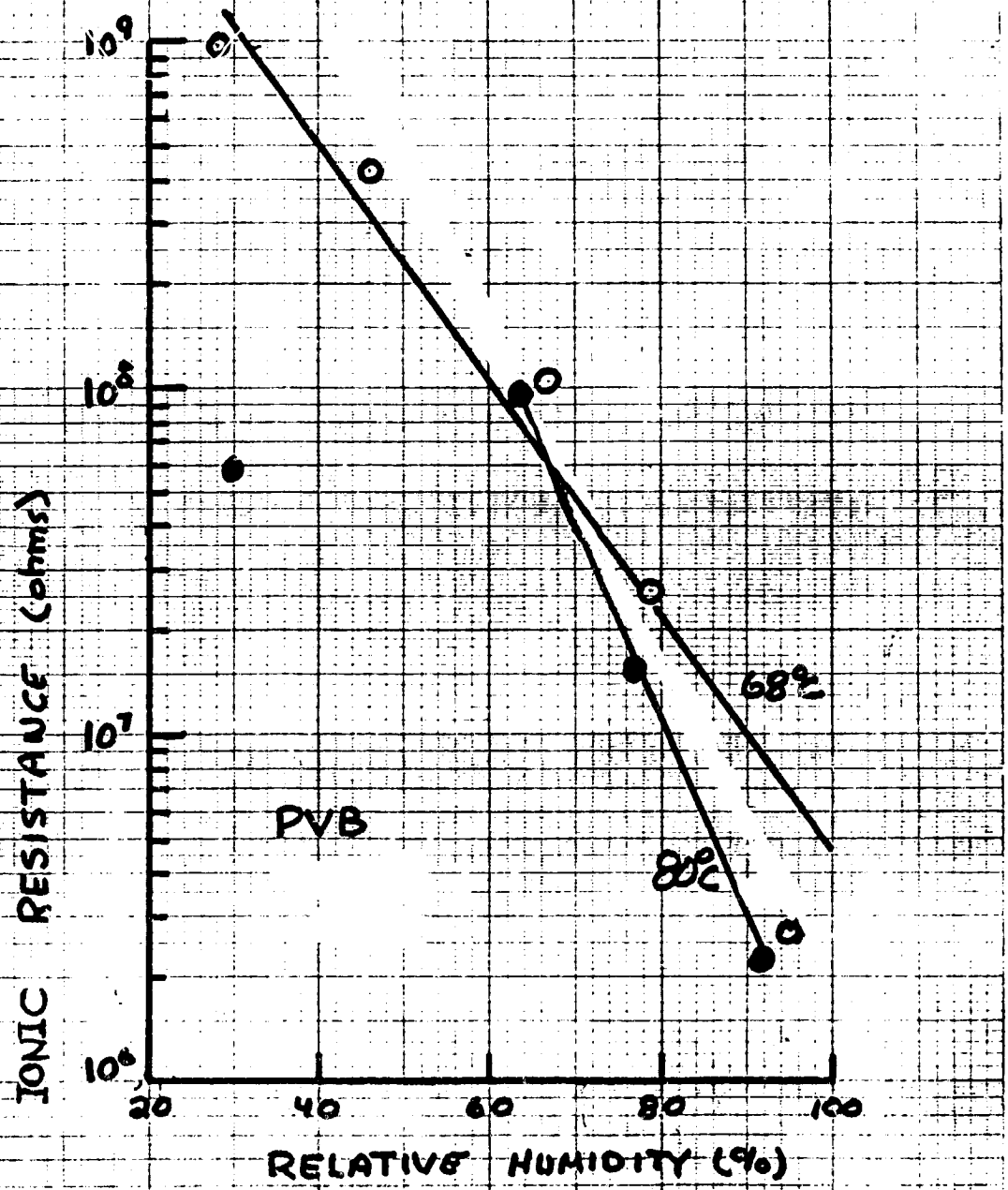

FIGURE 10

Relative humidity dependence of the ionic (R_i) resistance of PVB at 80°C and 68°C.

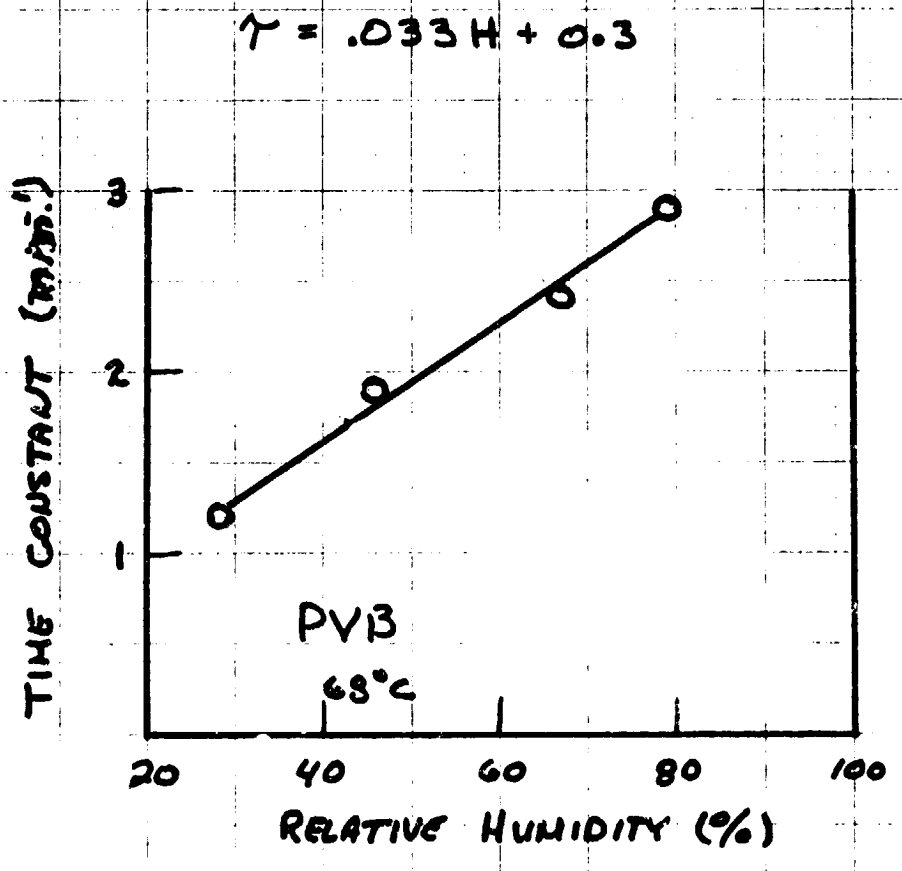

FIGURE 11

Humidity dependence of the time constant characterizing the initial transient behavior in the d.c. response current data for PVB at 68°C

$68°C: \quad R_o = 1.1(10^9)\exp(-.078H)$

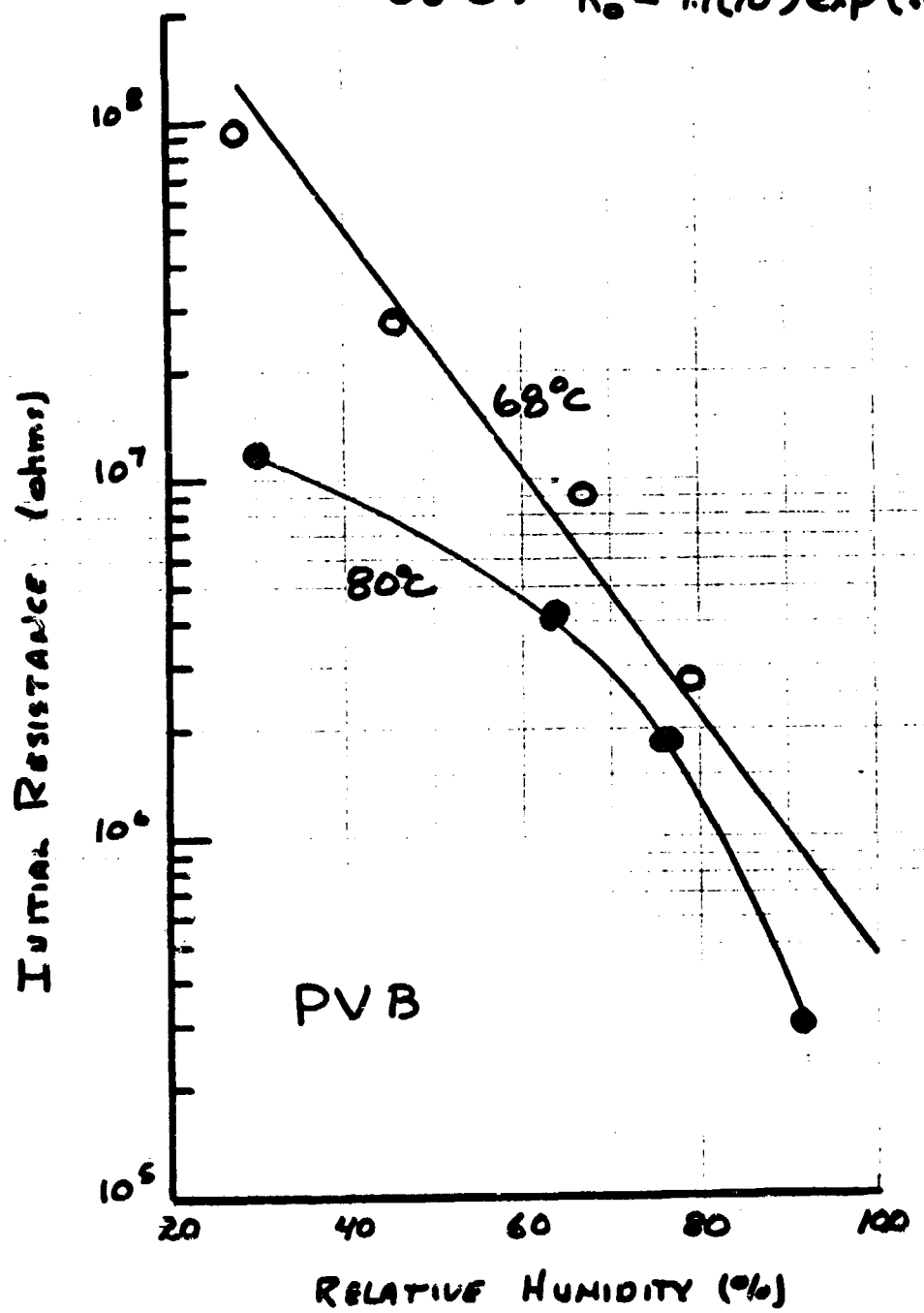

FIGURE 12

Humidity dependence of the initial resistance (R_o) of PUB at 68° and 80°C.

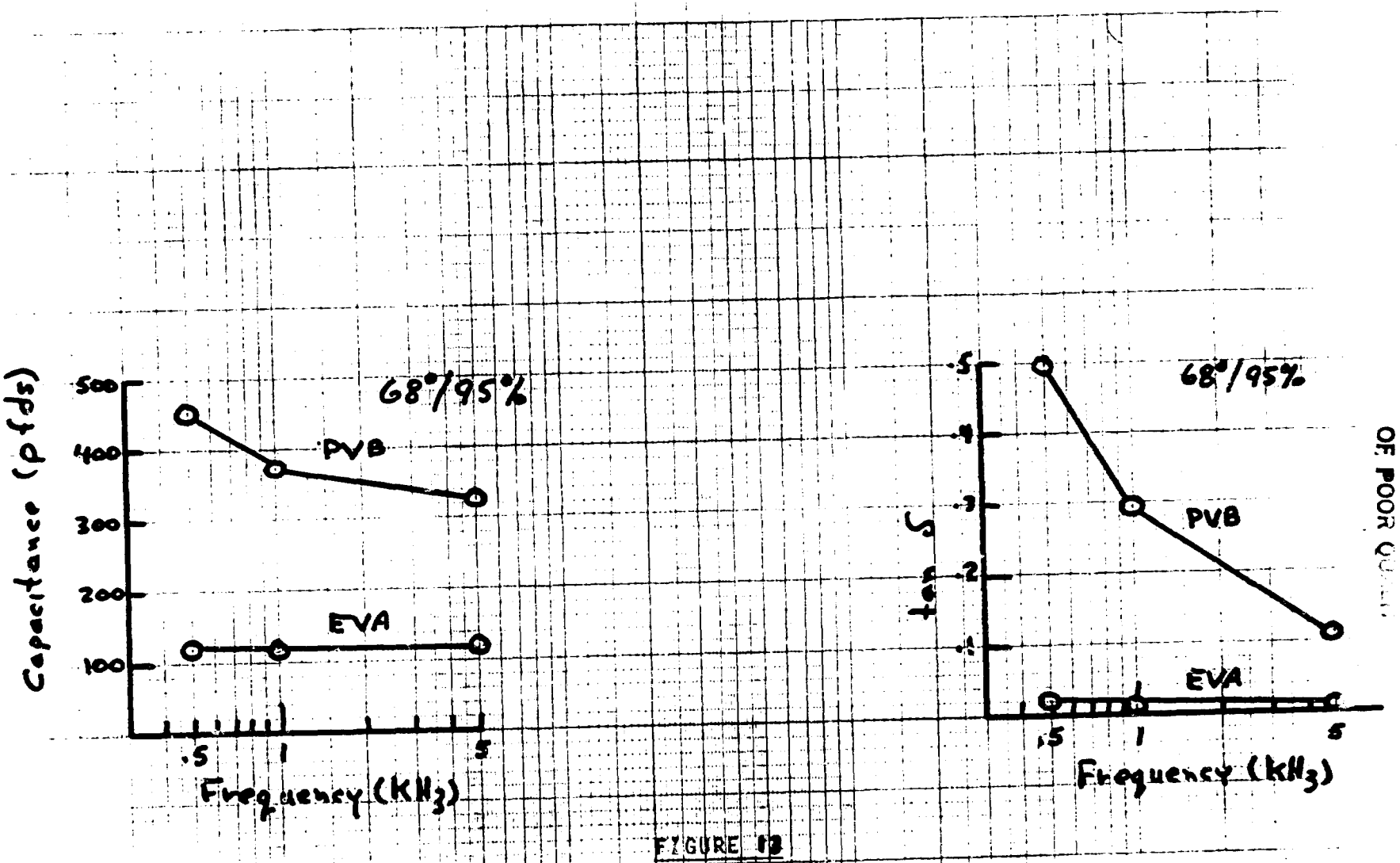

FIGURE 12

Capacitance and tan δ dissipation factor as a function of frequency for PVB and EVA at 68°C and 95% relative humidity.

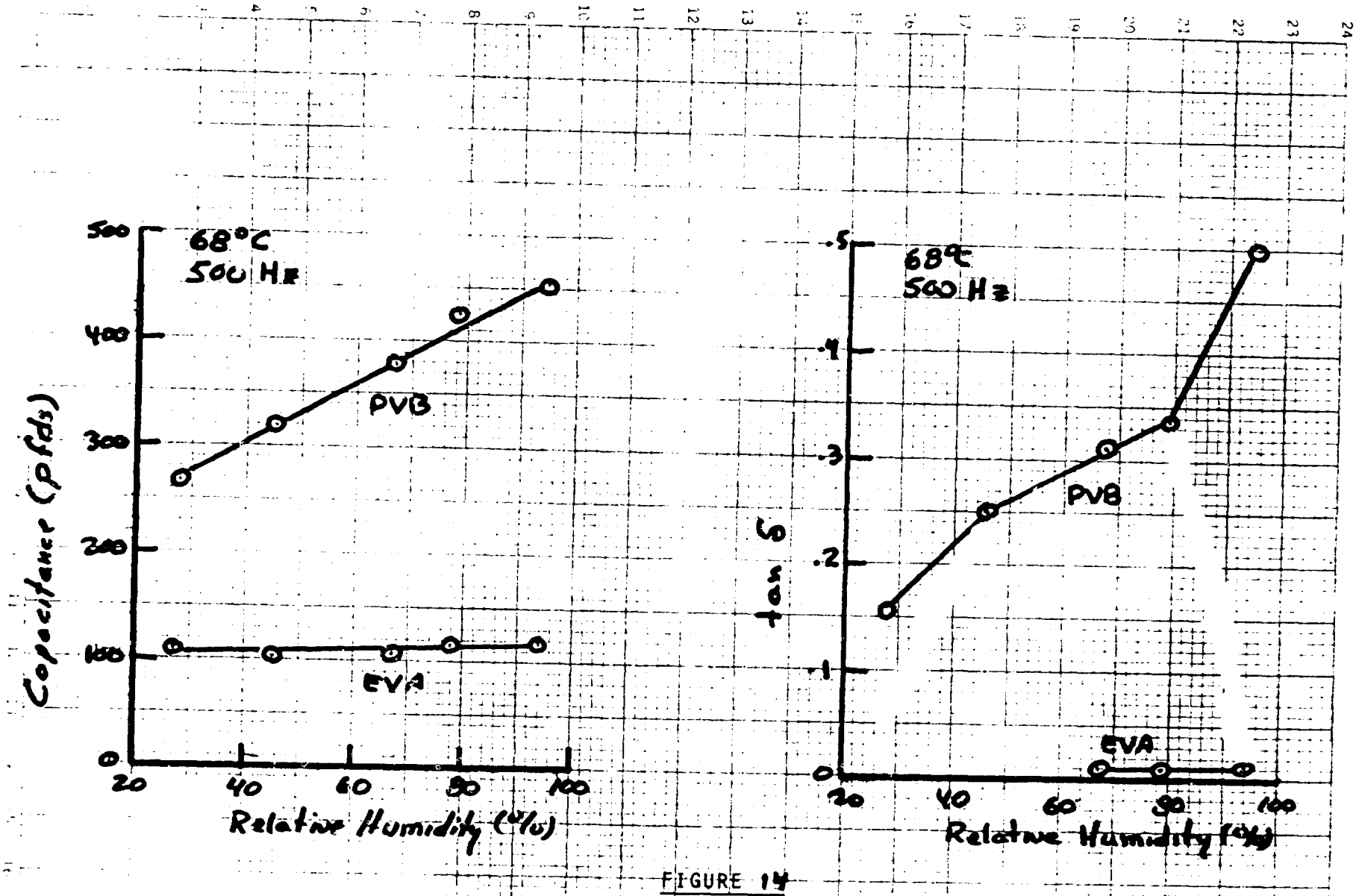

FIGURE 14

Capacitance and ~~tan δ~~ dissipation factor at 500Hz as a function of the relative humidity for PVB and EVA at 68°C.

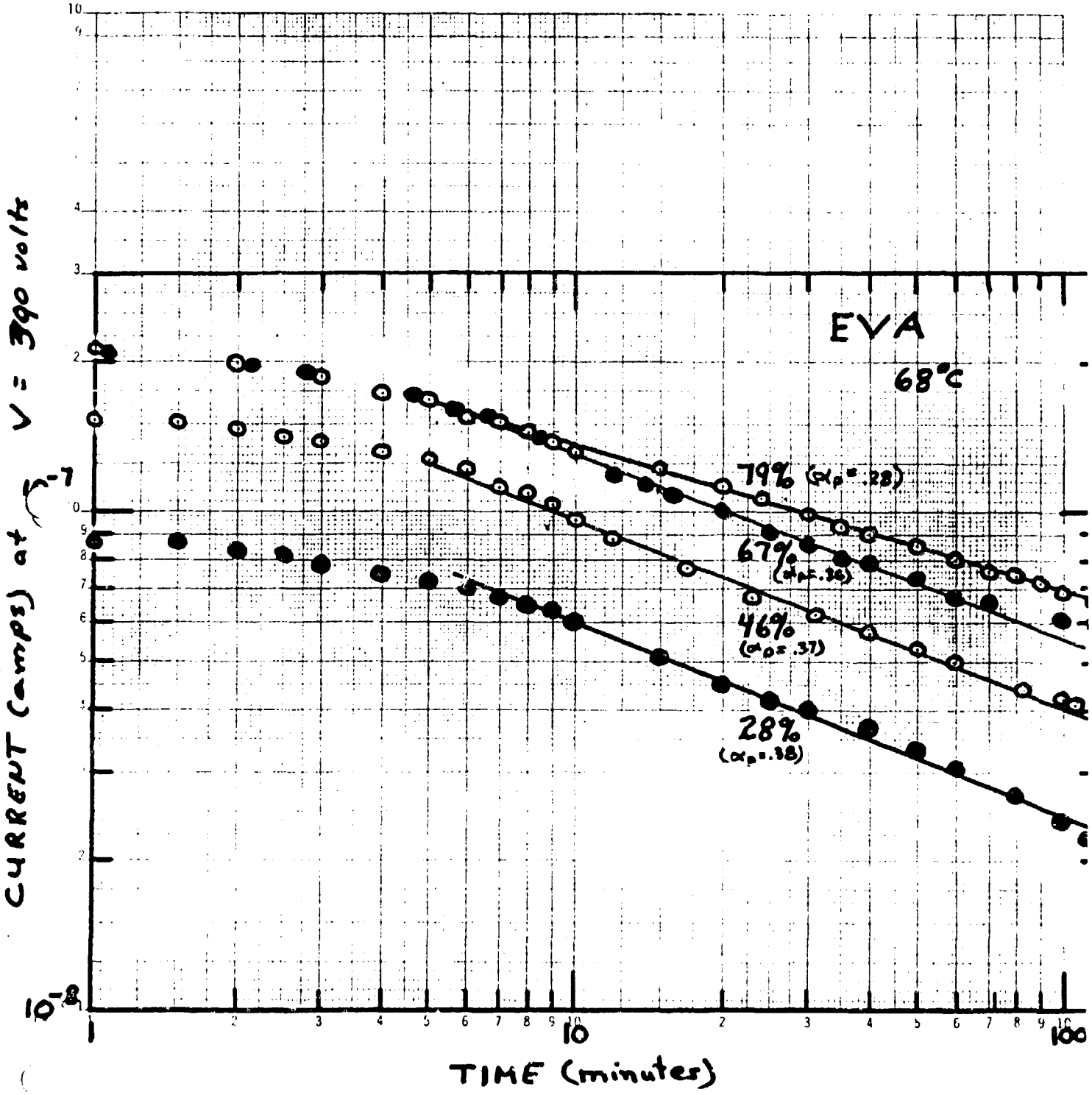

FIGURE 15

Time dependence of the d.c. response current resulting from a 390 volt step forcing function applied to EVA at 68°C and various relative humidity levels.

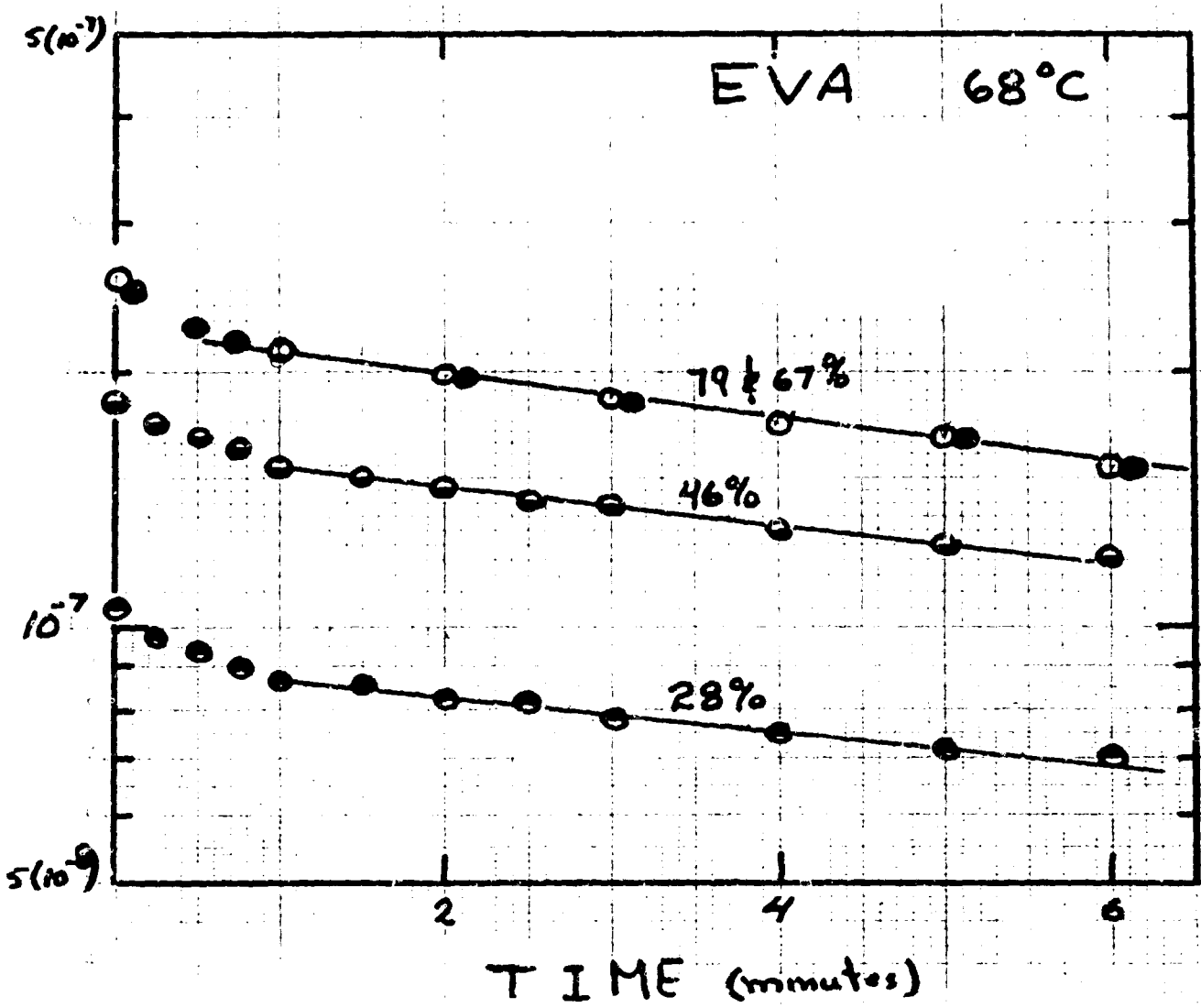

FIGURE 16

Initial transient behavior for the d.c. response data shown in Figure 14.

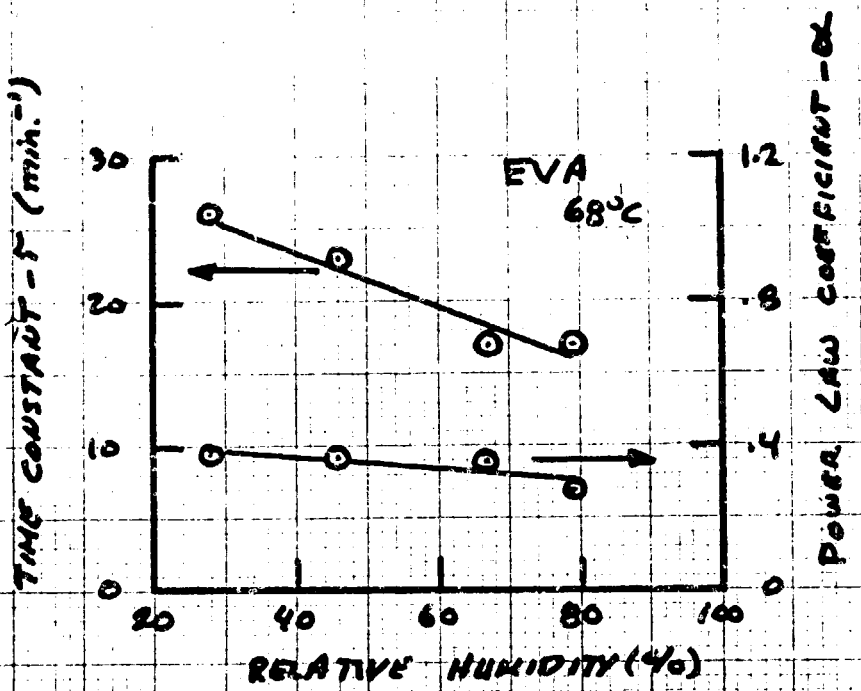

FIGURE 17

Relative humidity dependence of the time constant and the power law coefficient characterizing the d.c. response data shown in Figures 16 and 15 respectively.

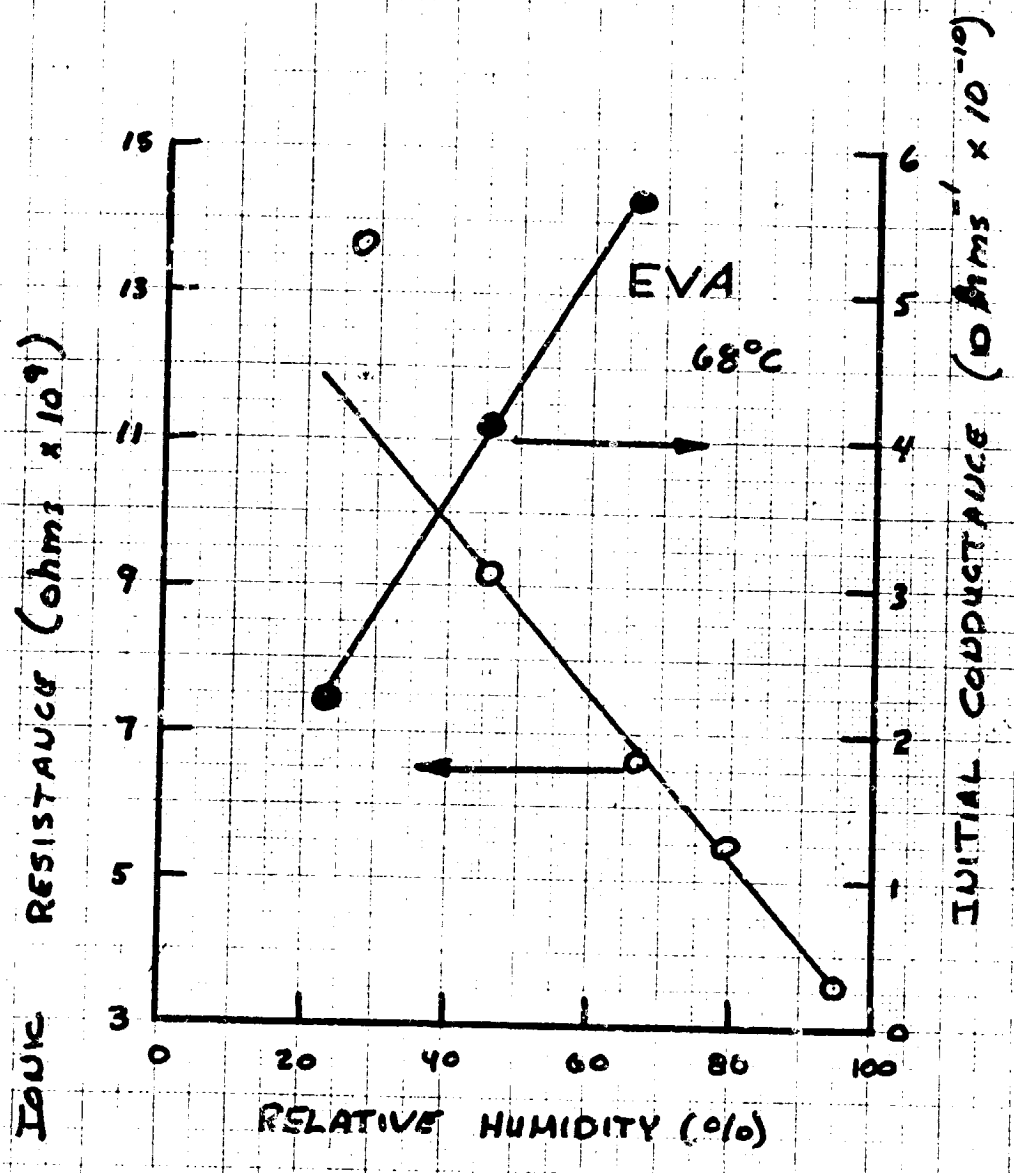

FIGURE 18

Relative humidity dependence of the R_i ionic resistance and the initial conductance I_o of EVA at 68°C.

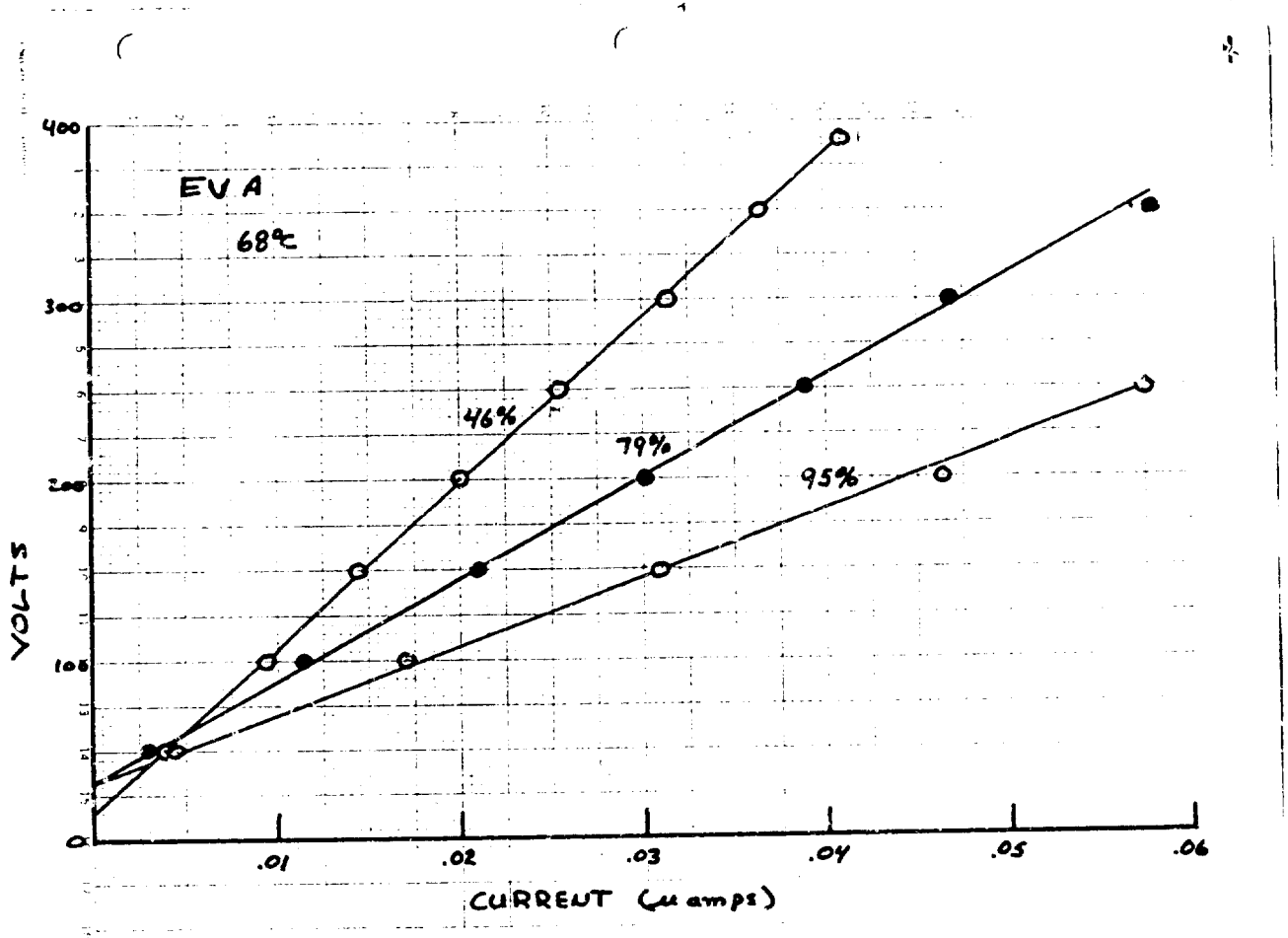

FIGURE 19

Current-voltage characteristics curves for ionic transport in EVA at 68°C and various relative humidity levels.

I. Kinetics of Water Absorption and Desorption in EVA

Results:

The kinetics of water absorption and the kinetics of water desorption in EVA were evaluated gravimetrically at various temperatures between 40°C and 88°C. The experimental procedure consisted of weighing EVA samples that had been dried in a desiccator for several weeks. The samples were of constant thickness, and represented a semi-infinite plate geometry. Each dried sample was "quenched" into a temperature-humidity chamber operating at a 100% humidity level and at a selected temperature between 40°C and 88°C. The weight gain of each sample was monitored continuously as water was absorped from the surrounding ambient. A comparison of the weight w_{o_e} of the desiccated dried sample and the measured starting weight w_{o_a} at zero time of the sample in the temperature—humidity chamber is shown in Table I where it is apparent that the measured starting weight is considerably larger than the dessicated dried weight which is the expected starting weight of the sample. This comparison suggests that EVA surface absorbs a layer of water immediately upon insertion into the temperature-humidity chamber. The weights $(w_{o_a} - w_{o_e})$ of these initially formed layers at the various temperatures for water absorption are listed in Table I. To correct for variations in sample size, the weight of this initially formed surface layer is normalized by the w_{o_e} expected starting weight, and the resulting normalized $[w_{o_a} - w_{o_e}]/w_{o_e}$ values (Table I) are found to be temperature dependent (Figure 1) according to the relationship:

$$\frac{w_{o_a} - w_{o_e}}{w_{o_e}} = 8(10^{-4})T + 15 \qquad (1)$$

where T is the temperature in degrees centigrade. An attempt is currently being made to justify this linear temperature dependence. The feature that the intercept is 15°C rather than 0°C defies explanation.

The time dependence of the apparent normalized weight gain w_t/w_{o_a} due to water absorption at 40°, 50°, 60°, 75°, and 88°C in a 100% humid environment is shown in Figure 2 while Figures 3 to 7 present a more detailed analysis of the data at the various temperatures. This detailed analysis shows that water absorption in EVA occurs in two stages. The initial stage (Stage I) displays a linear time dependence for the normalized weight gain:

$$\frac{w_t}{w_{o_a}} = At + B \tag{2}$$

where the rate constant A and the intercept B determined at the various run temperatures are presented in Table II. The rate constant A is found to be exponentially temperature dependent (Figure 8):

$$A = 0.2 \exp(-350/T) \tag{3}$$

which when expressed in Arrhenius form:

$$A = A_o \exp(-\varphi_A^I/RT)$$

gives an activation energy Q_A^I for this Stage I absorption of 0.7 Kcal./mole and a pre-exponential value of 0.2 hrs. as shown in Table III. This initial stage of water absorption is followed by a second kinetic stage (Stage II) where the normalized weight gain appears to obey (Figures 3 to 7) a square root of time kinetic response:

$$\frac{w_t}{w_{o_a}} = Ct^{1/2} + D \tag{4}$$

The rate constant C and the intercept D determined at the various run temperatures are shown in Table II. The rate constant C is exponentially temperature dependent (Figure 9):

$$C = 23 \exp(-2550/T) = C_o \exp(-\Phi_A^{II}/RT) \quad (5)$$

giving an associated activation energy Φ_A^{II} of 5.1 kcal./mode and a pre-exponential C_o value of 23 $hr.^{-\frac{1}{2}}$ (Table III).

The Stage II kinetic response concludes when the monitored weight becomes time independent and the EVA is saturated with its equilibrium amount of absorbed water. Reaching equilibrium is a time consuming experimental process that could not be completely justified for the amount of useful information that could be obtained. As a result, equilibrium was never unambiguously achieved before the experimental absorption runs at the various temperatures were terminated. However, the runs were terminated when the experimental weight gain results clearly indicated that equilibrium was being approached. The final measured sample weight w_∞ shown in Table I for each run temperature is believed to be representative of the equilibrium water saturated EVA sample weight. From these values of the final measured weights, the true weight change $w_\infty - w_{o_e}$ of each water saturated sample at their respective absorption run temperatures can be evaluated. The results are presented in Table I. This true weight change is believed to represent the sum of weights of both the water absorbed inside the EVA sample and the water film absorbed on the surface of the EVA sample.

The water desorption kinetic run started with the termination of each absorption kinetic run. The experimental procedure consisted of removing the water saturated sample from the temperature-humidity chamber and "quenching" the sample in a dry box maintained at the same temperature and at a 0% humidity.

The weight of the sample was monitored continuously during this quenching-deabsorption process. The final measured weights during the absorption runs were the expected starting weights for the desorption runs as indicated in Table I. The measured starting weights w_{o_a} of the desorbing samples were significantly smaller than the expected starting weights as indicated in Table I. The difference between the expected and measured starting weights $(w_{o_e} - w_{o_a})$ shown in Table I, is believed to represent some surface film water that is instantaneously evaporated when the quenching operation is consumated. When normalizing this $w_{o_e} - w_{o_a}$ weight difference by the expected starting weight to correct for differences in sample area, the true weight change ratio $[w_{o_e} - w_{o_a}] / w_{o_e}$ of this instanteously lost surface layer can be evaluated at each run temperature. The results (Table I) when plotted against the run temperature (Figure 10) exhibit a considerable amount of scatter from a linear type of dependence that was evident (Figure 1) in the absorption data.

The time dependence of the normalized weight loss due to water desorption from water saturated EVA samples at 40°, 50°, 60°, 75° and 88°C in a zero percent humidity environment is comparatively displayed in Figure 2 with the analogous normalized weight gain absorption data. Desorption is clearly a faster kinetic process than absorption.

The details of the time dependence for the water desorption process in EVA at each run temperature is shown in Figures 11 to 15. Similar to abosrption, water desorption in EVA is also a two stage kinetic process where the first stage is linear with time (Eg. 2) and the second stage is linear with the square root of time (Eg. 4). The characterizing rate constants A and C and intercepts B and D for Stage I and Stage II behavior respectively for the desorption process are presented in Table II for the various run temperatures. The Stage I rate constant A is exponentially temperature dependent (Fig. 8):

$$A = 167 \exp(-3050/T) \qquad (6)$$

which yields a characterizing activation energy Q_D^I for Stage I water desorption of 6.1 Kcal/mole. The Stage II desorption rate constant C can be represented by an exponential temperature dependency (Fig. 9— dotted line) provided one data print is neglected, and this particular temperature dependency is given by the relationship:

$$C = 159 \exp(-2050/T) = C_o \exp(-Q_D^{II}/RT) \qquad (7)$$

where the characterizing activation energy Q_D^{II} is 5100 Kcal/mole. Table III presents a comparative summary of the activation energies and the pre-exponential rate constant factors for the Stage I and Stage II absorption and desorption kinetics processes.

Discussion of Results

The two stage kinetic response evident for both water absorption and desorption in EVA is identical to the kinetic response previously observed in PVB (Quarterly Report—May 31, 1984). The model previously employed to explain the kinetic behavior in PVB would also be appropriate for EVA. In the absorption process, this model suggests that water in the atmosphere reacts with a dehydrated polymer by being absorbed into the polymer and by being adsorbed as a layer on the surface of the polymer. The final result is a hydrated polymer covered by a surface water film as shown in Figure 16. The overall reaction for water would then be:

$$H_2O\ (\text{in atmos.}) \longrightarrow H_2O\ (\text{in polymer and in surface film}) \qquad (8)$$

This overall reaction can be expressed as the sum of several component sequential reaction steps as is also illustrated schematically in Figure 16. These reaction steps with their associated rate constants k_1^A, k_{2a}^A, and k_{2b}^A are:

Step 1:

$$H_2O\ (\text{in atmos.}) \xrightarrow{k_1^A} H_2O\ (\text{monolayer on surface}) \qquad (9)$$

Step 2a:

$$H_2O\ (\text{in atmos.}) + H_2O\ (\text{monolayer on surface}) \xrightarrow{k_{2a}^A} H_2O\ (\text{surface film}) \qquad (10)$$

Step 2b:

$$H_2O\ (\text{monolayer on surface}) \xrightarrow{k_{2b}^A} H_2O\ (\text{in polymer}) \qquad (11)$$

where Step 1 corresponds to the condensation of atmospheric water as a monolayer on the surface of the polymer; Step 2a corresponds to the condensation of successive monolayers to form a film of water on the polymer surface; and Step 2b which occurs simultaneously with Step 2a corresponds to the water molecules on the surface diffusing into the polymer sample. The absorption kinetics of the polymer will then be determined by the rate constant k of the slowest sequential reaction step. When the slowest sequential reaction step involves two simultaneously occuring reactions, the absorption kinetics can exhibit a two-stage kinetic response where the first stage is governed to the faster of the two reactions while the second stage, governed by the slower of the two reactions, becomes evident in the experimental data when the first stage reaction has gone to completion. If the rate constants for the component reaction steps lie in the sequence

$$k_1^A > k_{2a}^A > k_{2b}^A \qquad (12)$$

the model would predict a two-stage kinetic response where the first stage corresponds to the building up of successive monolayers (Step 2a--Equation 10) to form a surface film. The surface film will continue to grow in thickness until an equilibrium thickness is achieved and then the second stage simultaneously occuring kinetic response, corresponding to water molecules, diffusing into the polymer from the surface (Step 2b - Equation 11), will

become apparent. The kinetic theory of gases suggests that the growth of a film of water on the polymer surface during the first kinetic stage of water absorption will result in a weight gain that is linear with time while simple diffusion theory with the appropriate boundary conditions predicts that the second kinetic stage for diffusing water into the polymer will result in a weight gain that is linear with the square root of time. The fact that these predictions are consistent with the experimental observations (Figures 3 to 7) provides credibility to the proposed model for water absorption in EVA.

While the kinetic theory of gases predicts the experimentally observed linear time dependence for weight gain during the first stage behavior, the theory also predicts that the weight gain rate should be much more temperature sensitive than is observed experimentally, and that the activation energy should be significantly larger than the experimentally obtained value of 0.7 Kcal/mole.

The desorption kinetics can also be modeled by a sequence of reactions involving a rate limiting step, as was suggested in the previous PVB work. The overall reaction is given by:

$$H_2O \text{ (in polymer and in surface film)} \longrightarrow H_2O \text{ (in atmos.)} \qquad (13)$$

and this reaction is proposed to be the sum of the sequential component reactions:

Step 1:

$$H_2O \text{ (in polymer and in surface film)} \xrightarrow{k_1^D} H_2O \text{ (in polymer)} + H_2O \text{ (in atmos.)} \quad (14)$$

Step 2:

$$H_2O \text{ (in polymer)} \xrightarrow{k_2^D} H_2O \text{ (monolayer on surface)} \quad (15)$$

Step 3:

$$H_2O \text{ (monolayer on surface)} \xrightarrow{k_3^D} H_2O \text{ (in atmos.)} \quad (16)$$

These reactions are presented schematically in Figure 17 where the first step in the reaction sequence (Equation 14) involves the evaporation of the absorbed layer of water on the surface of the polymer. This reaction must go to completion before the necessary boundary conditions are established for the second reaction step (Equation 15) to be activated. In the second reaction step, water molecules in the interior of the polymer diffuse out to the surface where they form a molecular monolayer which then evaporates (Step 3) into the atmosphere.

This reaction sequence is consistent with experimental weight loss desorption observations if the rate constants for the desorption component reaction steps is smallest for Step 1 and largest for Step 3:

$$k_3^D > k_2^D > k_1^D \quad (17)$$

Initially the weight loss kinetics would then be determined by Step 1 (Equation 14) until this evaporation reaction goes to completion. Upon completion, the weight loss kinetics would then be given by diffusion of water out of the polymer (Step 2--Equation 15) until the polymer is completely dehydrated. The weight loss kinetics would then occur in two stages where the first stage is due to evaporation of a surface film and is expected to be linear with time, while the second stage results from volume diffusion of water out of the polymer, and is expected to be linear with the square root of time. These expected features for the weight loss kinetics are evident in the experimental desorption data (Figures 11 to 15). This two stage behavior with its associated time dependencies for desorption kinetics is the reverse equivalent to the absorption kinetic response but an important distinction exists. If the proposed reaction mechanisms correctly model the absorption and desorption processes, the Stage I and Stage II reaction mechanisms (Equations 9 and 10) occur concurrently in absorption where the Stage I reaction response is assumed to initially mask the Stage II reaction mechanism response. In desorption kinetics, the Stage I reaction and the Stage II reaction mechanisms (Equations 14 and 15) occur sequentially where the Stage II reaction initiates only after the Stage I reaction terminates. This very important distinction has considerable usefullness in a subsequent discussion of several anomalous features associated with the second stage rate constant data.

The suggestion that Stage I and Stage II behavior occur concurrently in absorption permits a more detailed analysis of the absorption data where this analysis will result in an indication of the solubility limit of water in EVA as a function of temperature. The solubility of water in EVA cannot be extracted from the true weight change given in Table I because this weight change is the sum of the weight of the water film adsorbed on the surface and the weight of the water absorbed into the EVA to its solubility limit. Since film formation and volume diffusion are occuring concurrently in water absorption, the Stage II — square root of time absorption kinetic response in Figures 3 to 7 can be extrapolated to a zero time intercept. The value of this intercept is the normalized weight gain w_s / w_{o_a}

due to forming a film of equilibrium final thickness. Table IV presents these intercepts along with the total normalized weight gain w_∞ / w_{o_a}

as determined from the time independent, saturated normalized weight gain values for each absorption run. From these values, the total weight gain w_∞, the weight gain w_s

due to surface film formation, the weight gain w_v due volume absorption,

and the solubility limit of water in EVA can be evaluated. The results are presented in Table IV and in Figure 18 where the temperature dependence for the limit of water solubility in EVA is displayed. The solubility increases

with increasing temperature up to approximately 80 °C. The retrograde solubility above 80°C suggests that the EVA water phase diagram is characterized by an invariant reaction at approximately 80 °C.

The other piece of information that can be extracted from the information in Table IV is the equilibrium thickness of the water film adsorbed to the EVA surface. This thickness can be easily calculated from the surface water weight (w_s) data, and the results as a function of temperature are presented in Figure 19. The explanation for this unexpected dependence continues to be mystifying.

The final aspect of the data that requires some discussion is rate constant data and their associated Q_D^I, Q_A^I, Q_D^{II}, and Q_A^{II} activation energies for the two-stage kinetics in both water absorption and water desorption. The Q_A^{II} and Q_D^{II} activation energies are associated with second stage behavior in absorption and desorption respectively. Since second stage behavior involves the bulk diffusion of water molecules into the polymer and out of the polymer in absorption and desorption respectively, the Q_A^{II} and Q_D^{II} activation energies should

be numerically equal. Numerical equality is suggested in Table III, but an examination of Figure 19 reveals a difficulty in unambiguously determining the value of the Q_D^{II} activation energy for Stage II desorption kinetics. The difficulty resides in the fact that the Stage II desorption rate constant data points do not obey a well-defined Arrhenius temperature dependency as expected for a volume diffusion controlled mechanism.

In contrast, the volume diffusion controlled Stage II absorption behavior rate constant data points do obey the Arrhenius Law (Figure 9) which yields a well defined value for the Q_A^{II} activation energy. This experimentally observed noncompliance with Arrhenius for Stage II desorption rate constant data and compliance for Stage II absorption rate constant data can be explained by appealing again to the proposed models where Stage II volume diffusion during absorption was suggested to occur concurrently with Stage I surface film formation while Stage II volume diffusion during desorption was suggested to occur sequentially after the Stage I surface film evaporation reaction goes to completion. The analysis for both absorption and desorption Stage II behavior consisted of analyzing the normalized weight change for a square root of time dependence where the time values were referenced to an origin at the instant of quenching. This origin is correct for the absorption run where volume diffusion occurs concurrently with surface film formation, and starts at the instant of quenching. This origin is not correct for the

desorption run where volume diffusion does not start at the instant of quenching, but rather starts at the time when the surface film is completely evaporated, and Stage I behavior terminates. The Stage II absorption analysis should then yield correct information and the resulting rate constants should obey an Arrhenius relationship as is observed experimentally. The Stage II desorption analysis is based on a time origin at the instant of quenching will not yield completely correct information about rate constants, and it is not surprising that an Arrhenius relationship is not strictly obeyed. These Stage II absorption rate constant data points, if not completely correct, are in approximate enough agreement with an Arrhenius slope of the 5.1 Kcal/mole (Fig. 9) activation energy to suggest that $Q_A^{II} \cong Q_D^{II}$

The observation of Arrhenius compliance and non-compliance for Stage II absorption and desorption rate constant data respectively as a result of choosing the time origin at the instant of quenching, provides a measure of indirect confirmation for the validity of the proposed models. Because of the uncertainty in choosing the appropriate time origin for the Stage II desorption data analysis, no attempt has been made yet to re-examine and correct this data.

While the Q_A^{II} and Q_D^{II} Stage II volume diffusion controlled activation energies are expected to be equal from volume diffusion considerations, the Q_A^{I} and Q_D^{I} activation energies associated the Stage I absorption condensation and desorption evaporation reactions respectively, are not expected to be equal particularly if the polymer is even slightly hydrophobic. If the polymer has hydrophobic tendencies, evaporation of a surface film will be much faster than condensation. The Stage I kinetics can then be represented by the typical energy barrier diagram shown in Figure 20 where the energy to climb over the barrier for the condensation reaction is significantly larger than the barrier clearing energy for the reverse evaporation reaction. The implications of this diagram are that the Stage I

desorption kinetics are faster than the absorption kinetics as is observed experimentally and that $Q_0^I > Q_1^I$ as seen in Table III.

The preceeding discussion does provide a reasonable explanation for the observed experimental results but the one feature associated with the rate constant data that has yet to be resolved is that the C_o pre-exponential factors for the Stage II volume diffusion mechanism in both absorption and desorption were expected to be equal and were found to differ (Table III) by almost two orders of magnitude.

Future Work

The kinetics of water absorption and desorption in EVA are completed. Except for several minor experiments to further evaluate the proposed models for absorption and desorption, the work effect is being terminated.

Temperature Humidity Conditions T (°C)/H (%)		Woe: Expected Starting Weight (gms)	Woe: Measured Starting Weight (gms)	Woe: Measured Final Weight (gms)	Woo-Woa: Apparent Weight Change (gms)	Woo-Woe: True Weight Change (gms)	Woa-Woe: Weight of Initially Formed Surface Layer (gms)	Woe-Woa: Weight of Initially Lost Surface Layer (gms)	Woe-Woa: / Woe Normalized Initial Surface Layer Weight
88/0 →88/100	abs.	1.600*	1.691	2.366	.675	.766	.091	—	.057
88/100 →88/0	des.	2.366	1.750	1.599	.151	.767	--	.616	.260
75/0 →75/100	abs.	1.821*	1.914	2.804	.890	.983	.093	--	.051
75/100 →75/0	des.	2.804	2.388	1.824	.564	.980	--	.416	.148
60/0 →60/100	abs.	1.520*	1.575	2.593	1.018	1.073	.55	--	.036
60/100 →60/0	des.	2.593	2.092	1.519	.573	1.074	--	.501	.193
50/0 →50/100	abs.	1.600*	1.647	2.565	.918	.965	.047	--	.029
50/100 →50/0	des.	2.565	2.198	1.602	.596	.963	--	.367	.143
40/0 →40/100	abs.	1.608*	1.613	2.295	.682	.695	.013	--	.008
40/100 →40/0	des.	2.295	2.149	1.603	.546	.692	—	.146	.063

* Original weight of desiccated dried sample.

abs. - absorption run

des. - desorption run

TABLE I

Weight characteristics of EVA during absorption and desorption.

	STAGE I		STAGE II	
	$\frac{Wt}{Woa} = At + B$		$\frac{W\phi}{W_{oa}} = Ct^{1/2} + D$	
Temp.	A	B	C	D
	Absorption			
	($hrs.^{-1}$)		($hrs.^{-1/2}$)	
88°C	.080	1.0	.0190	1.285
75°C	.080	1.0	.0125	1.460
60°C	.068	1.0	.010	1.570
50°C	.071	1.0	.0082	1.490
40°C	.031	1.0	.0062	1.335
	Desorption			
	($min.^{-1}$)		($min.^{-1/2}$)	
88°C	.030	1.0	-	-
75°C	.021	1.0	.0723	1.063
60°C	.0175	1.0	.0690	1.070
50°C	.0130	1.0	.0605	1.071
40°C	.0073	1.0	.441	1.066

TABLE II

Characterizing rate constants for Stage I and Stage II kinetic behavior for the normalized weight gain in water absorption and the normalized weight loss in water desorption in EVA.

STAGE I - Surface Film

	Q^I (kcal/mole)	A_o (min.$^{-1}$)
Absorption	0.7 ($=Q^I_A$)	.0033 (0.2 hrs.$^{-1}$)
Desorption	6.1 ($=Q^I_D$)	167

STAGE II - Volume Diffusion

	Q^{II} (Kcal/moie)	Co (min$^{-\frac{1}{2}}$)
Absorption	5.1 ($=Q^{II}_A$)	3 (23 hrs.$^{-\frac{1}{2}}$)
Desorption	5.1 ($=Q^{II}_D$)	159

TABLE III

Activation energies and pre-exponential factors for Stage I and Stage II kinetic response in water absorption and desorption in EVA.

Temperature	W_∞/W_{oa}: Total normalized weight gain	W_∞: total weight gain per gram EVA (gms)	W_s/W_{oa}: Total Normalized Weight Gain Due to Surface Film Formation (gms)	W_s: Weight Gain per Gram EVA due to Surface film Formation (gms)	W_v: Weight Gain per Gram EVA Due to Volume Absorption (gms)	$W\%$: Weight Percent Solubility of water In EVA (%)
88 °C	1.48+	.48	1.285*	.285	.195	16.3
75 °C	1.70+	.70	1.460*	.460	.240	19.3
60 °C	1.68+	.68	1.570*	.570	.110	9.9
50 °C	1.58+	.58	1.490*	.490*	.090	8.2
40 °C	1.42+	.42	1.335*	.335	.085	7.8

+ Determined from data in Table I

* Taken from extrapolated D intercept values in Table II

TABLE IV

Weight gain characteristics of EVA in water absorption due to surface film formation and volume absorption.

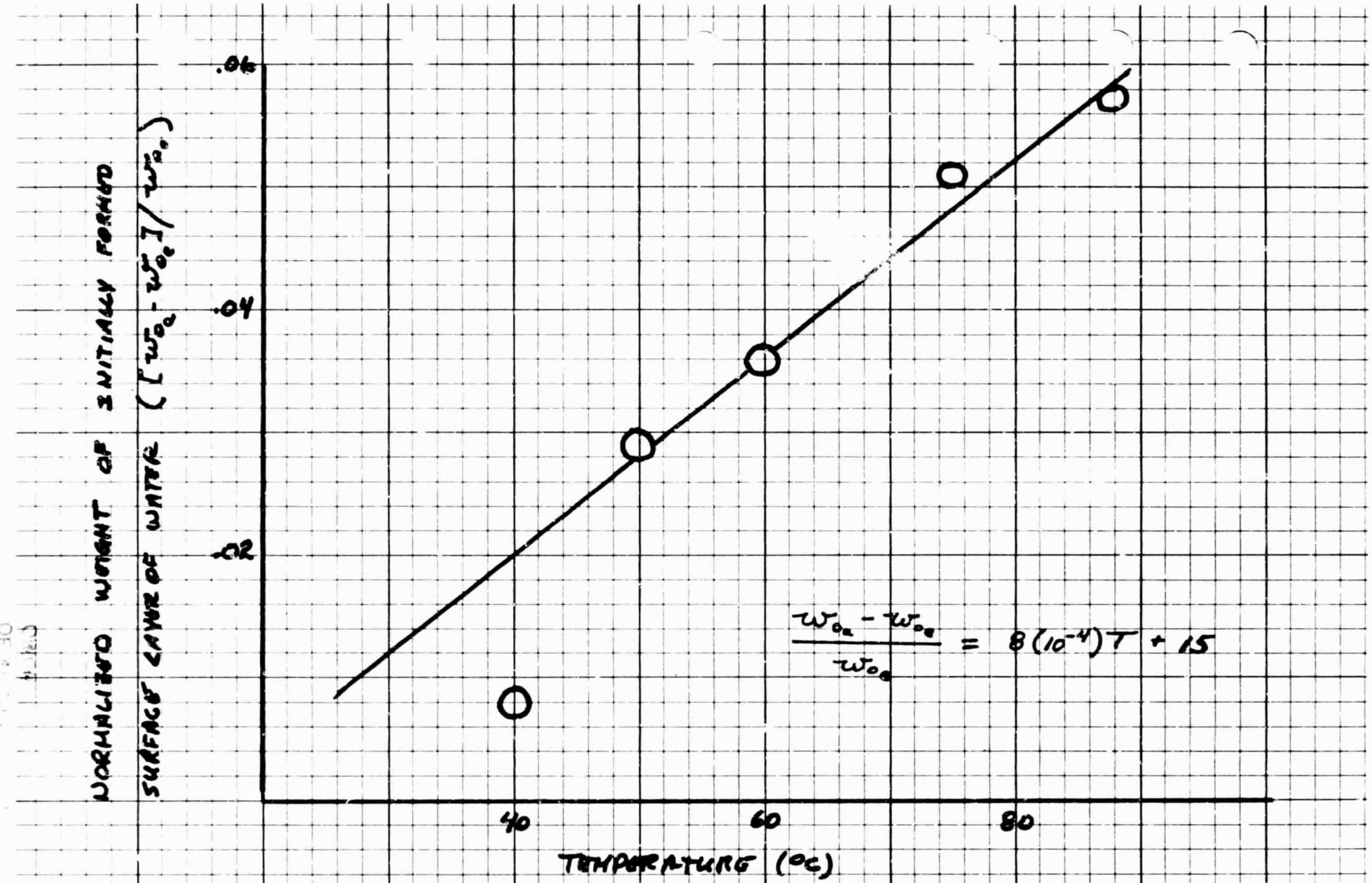

FIG. 1 — Temperature dependence of the normalized weight for the initially formed surface layer of water during water absorption in EVA

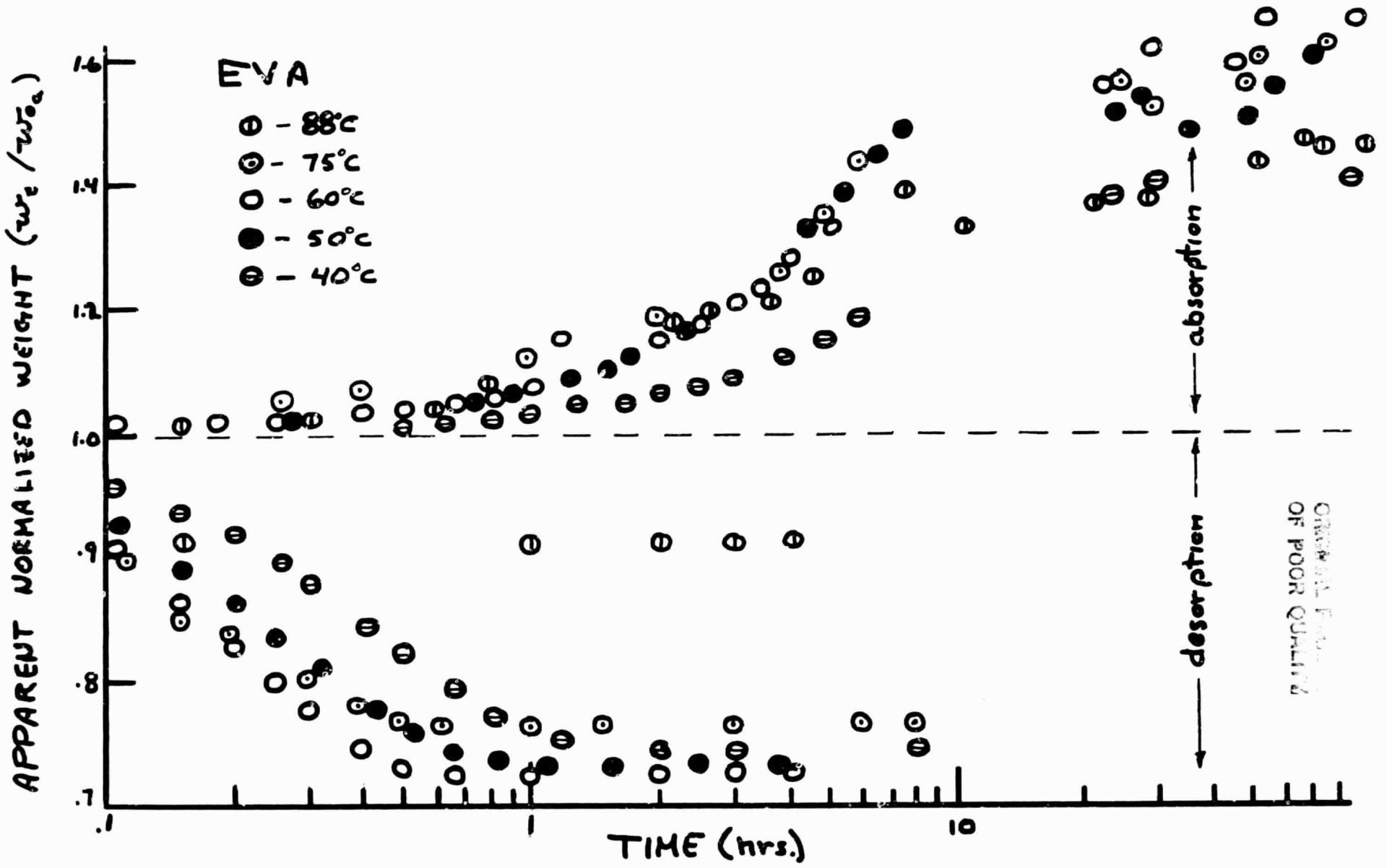

FIG. 2 – Time dependence of normalized weight change during absorption and desorption of water in EVA at selected temperatures

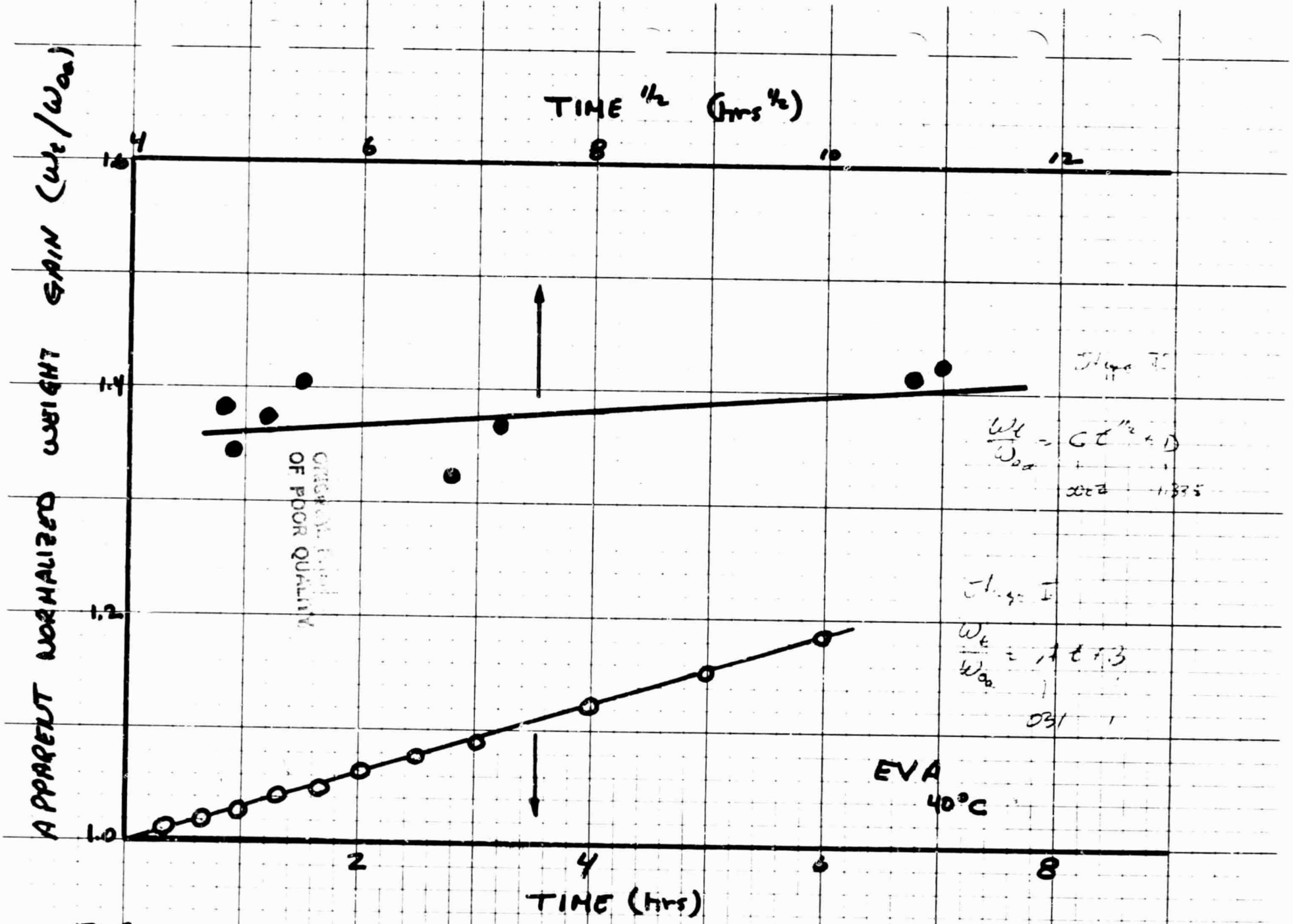

FIG. 3 — Time and Square Root of Time Dependence of Normalized Weight Gain in EVA due to water absorption

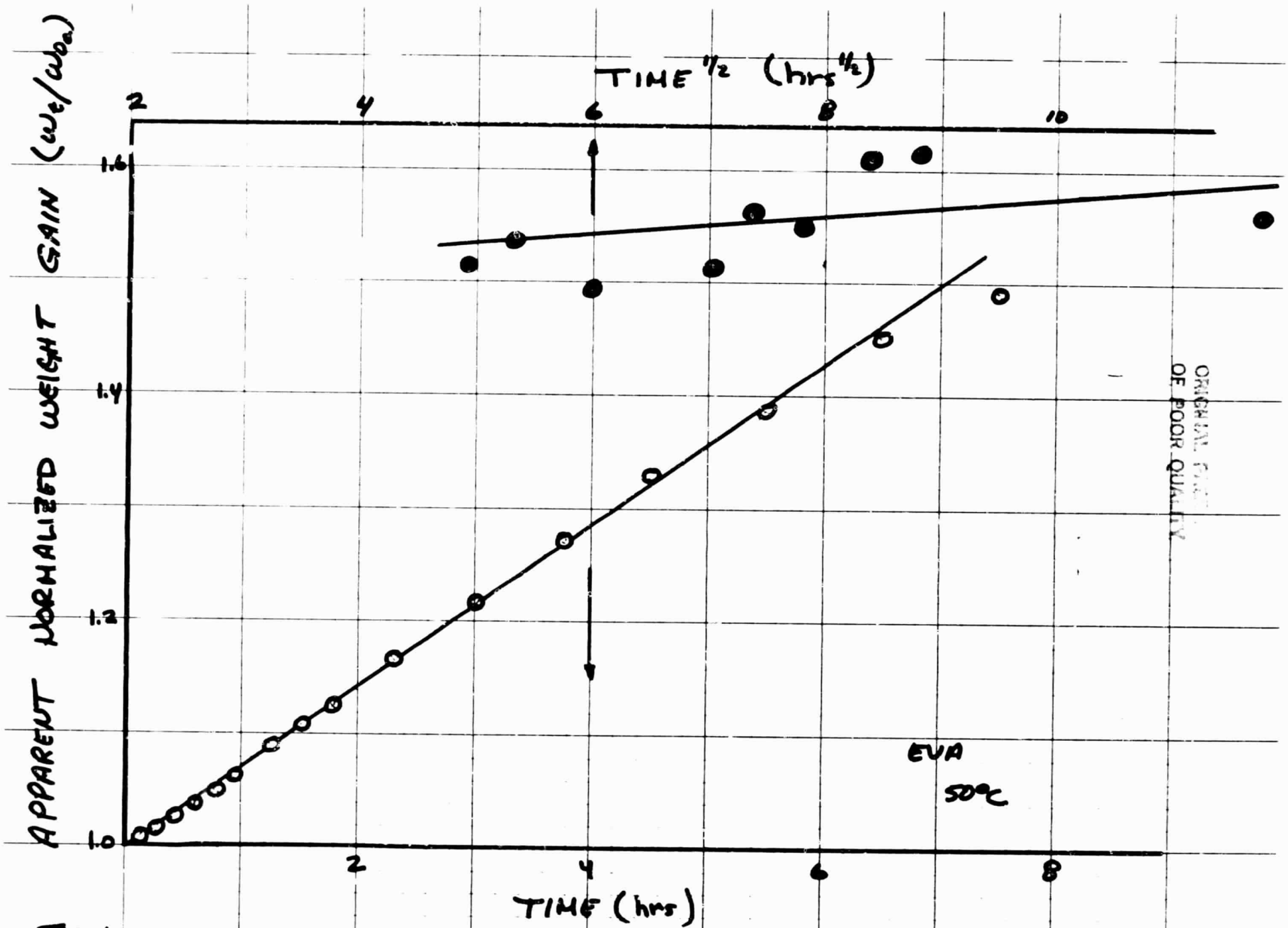

Fig. 4 — Time and square root of time dependencies of normalized weight gain in EVA due to water absorption at 50°C.

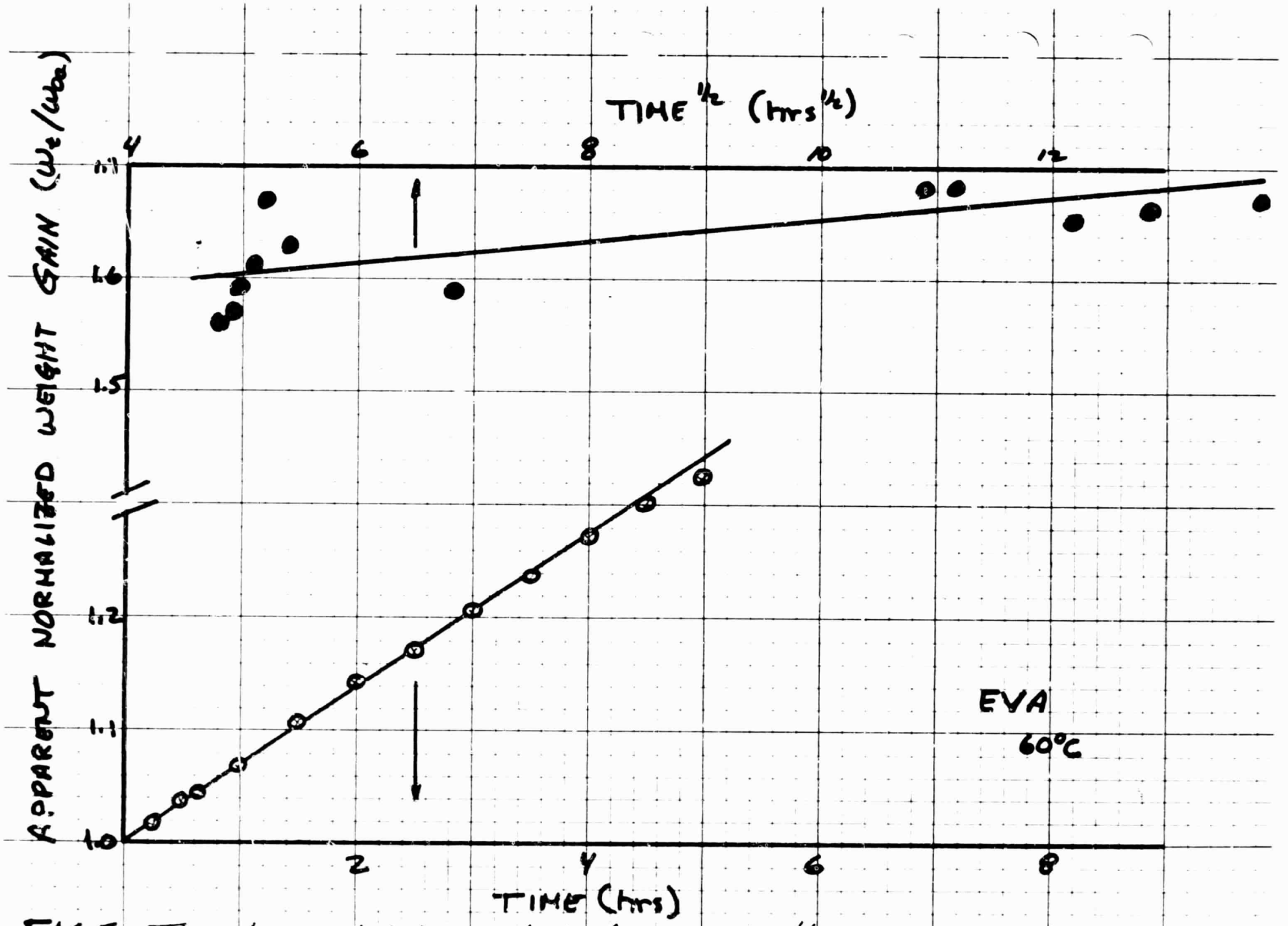

FIG. 5 – Time and square root of time dependencies of normalized weight gain in EVA due to water absorption at 60°

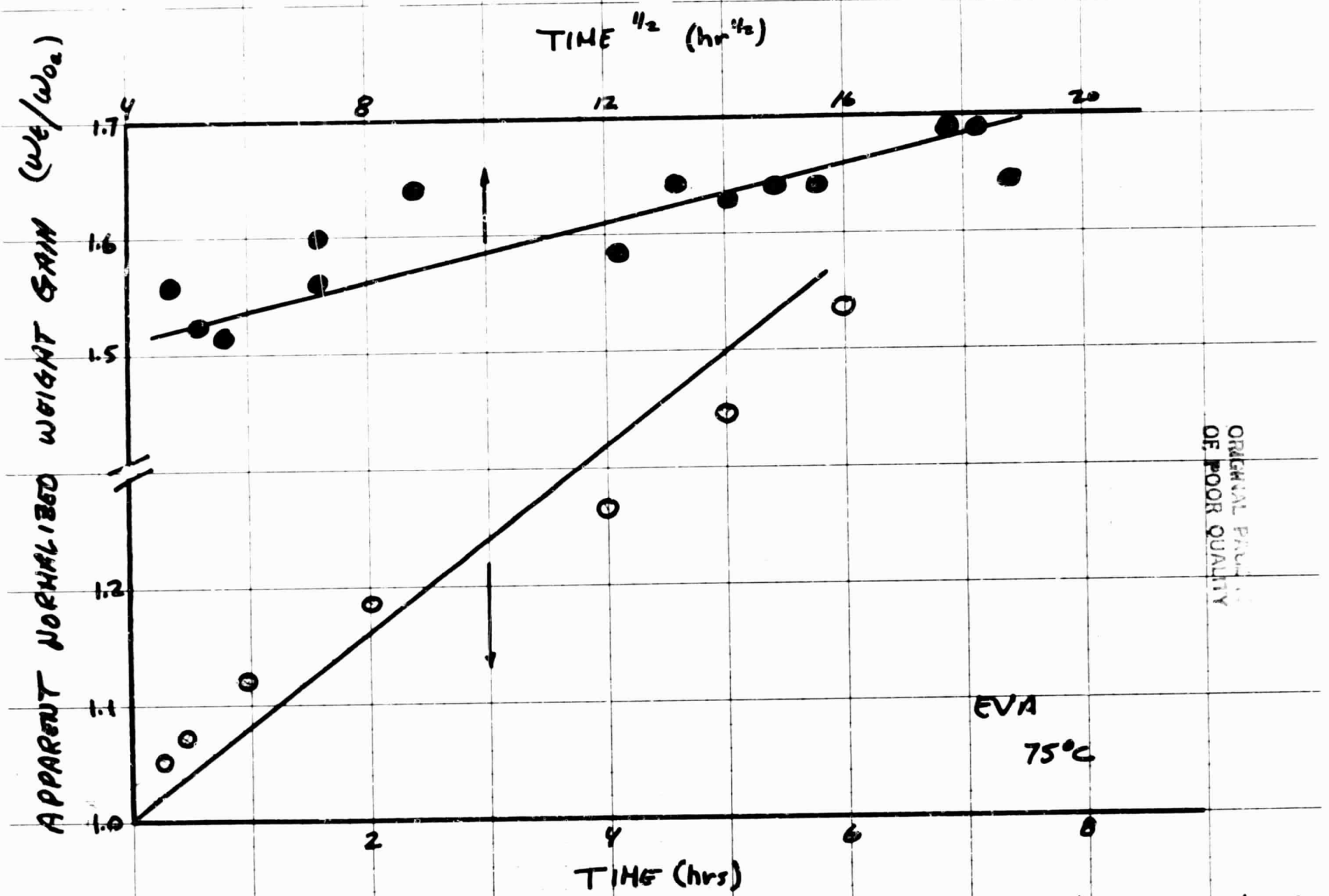

FIG. 6 – Time and square root of time dependencies of normalized weight gain in EVA due to water absorption at 75°C

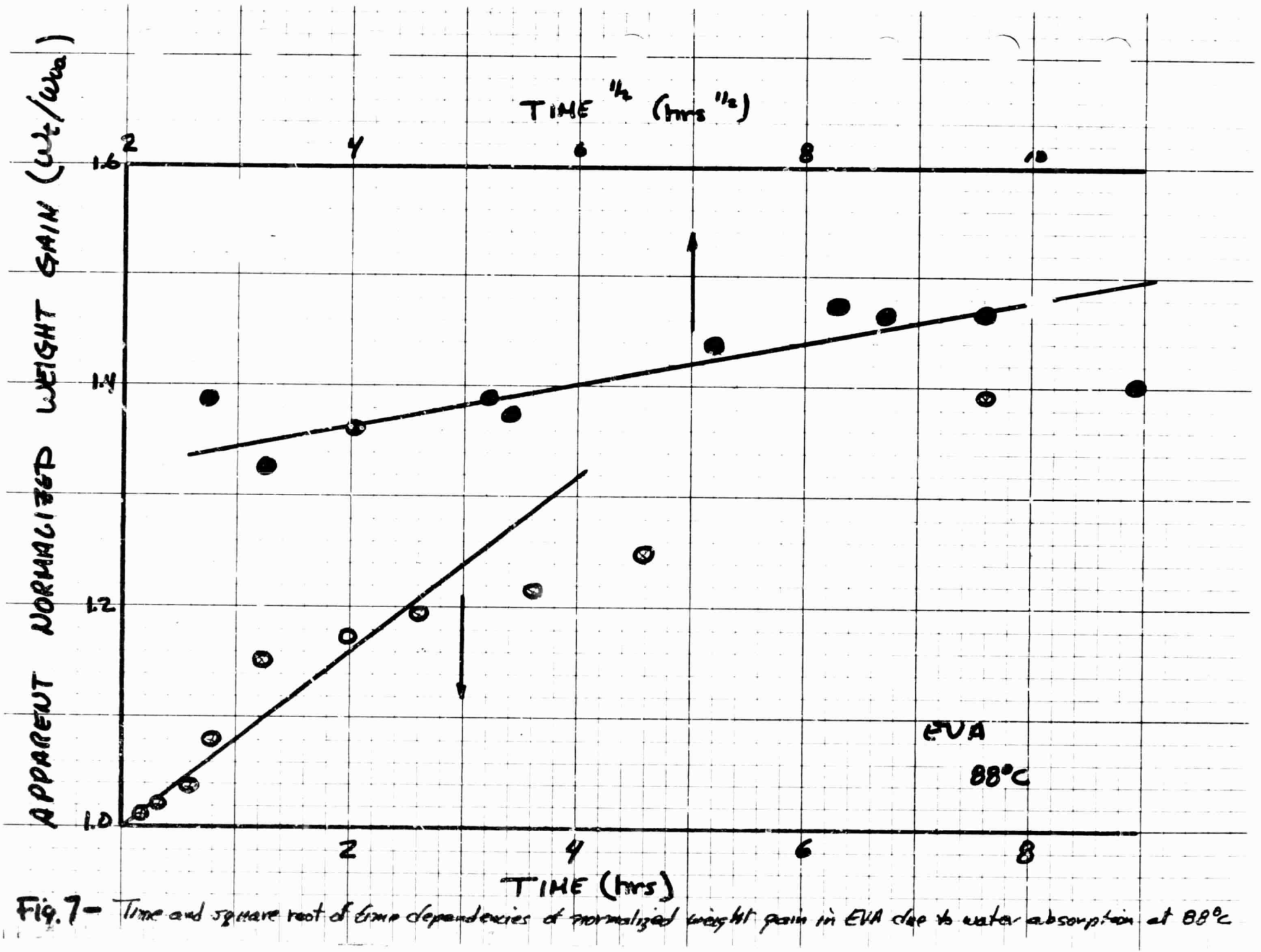

Fig. 7- Time and square root of time dependencies of normalized weight gain in EVA due to water absorption at 88°C

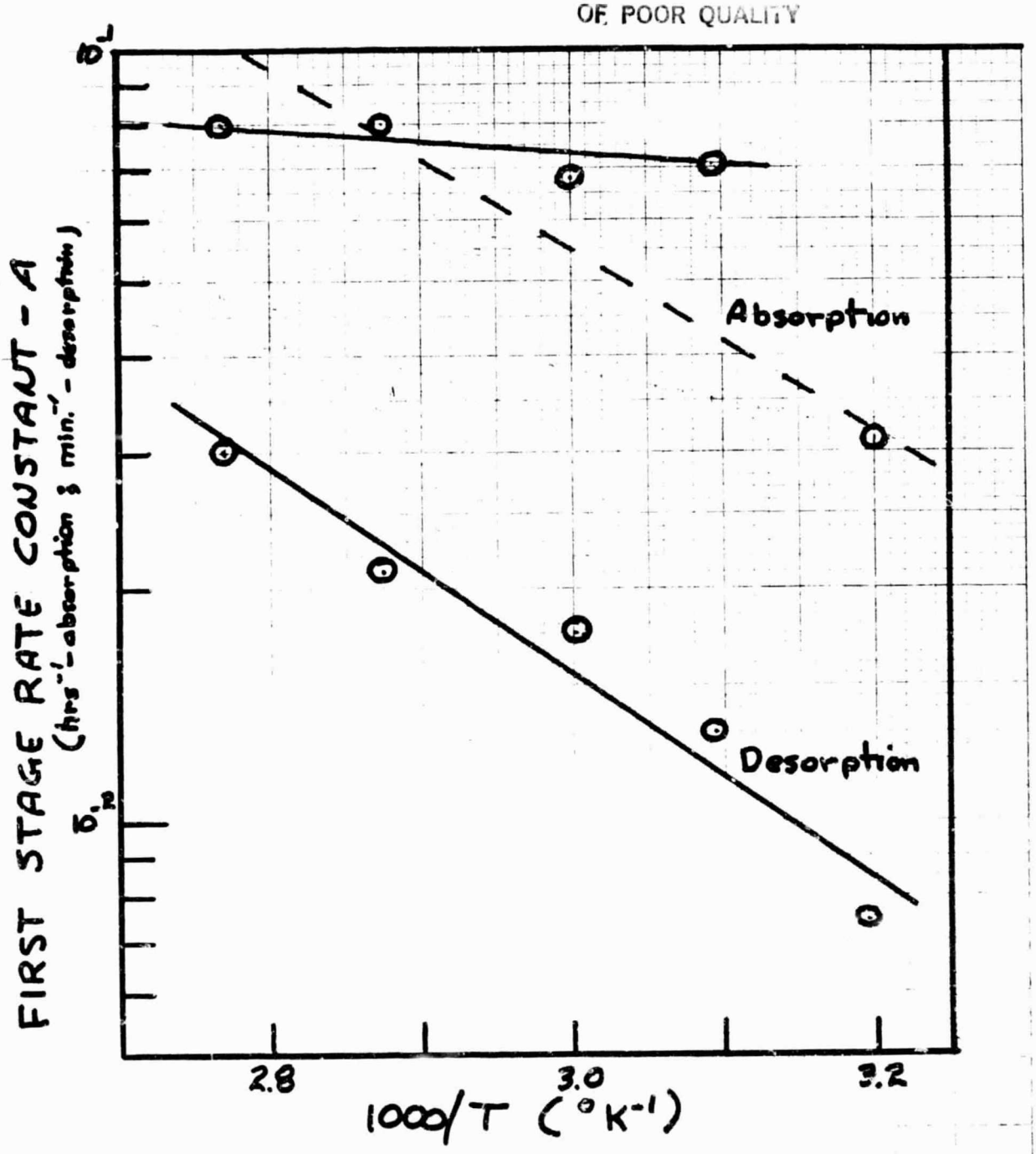

FIG. 8 — Temperature dependence of the rate constant for first stage water absorption and water desorption in EVA

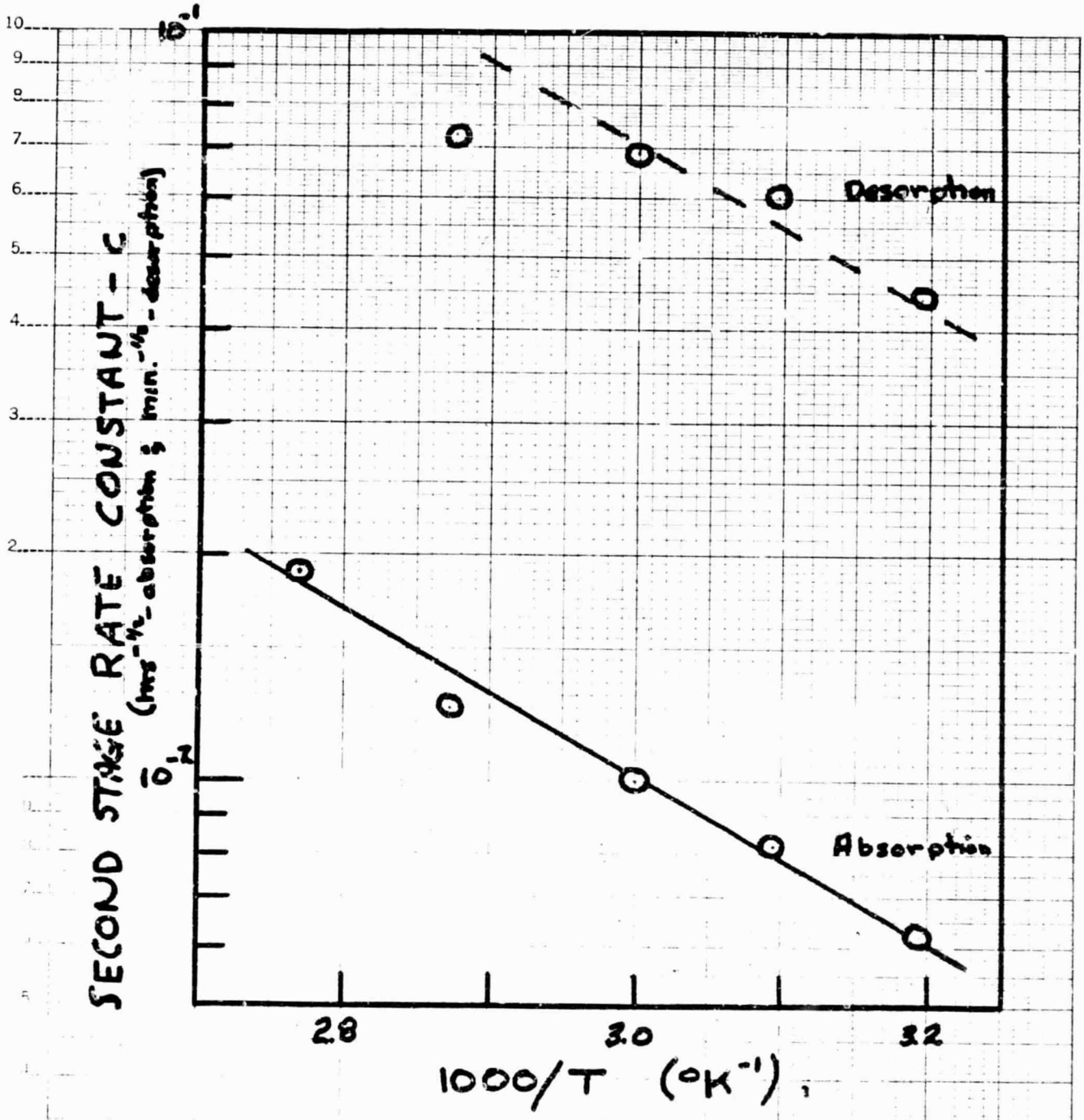

FIG. 8 - Temperature dependence of the rate constant for second stage water absorption and water desorption in EVA

Semi-Logarithmic
Cycles x 10 to the inch

Fig 10 — Temperature dependence of the normalized amount of water in the initially cast specimen as a function of water diffusion's equilibrium layer

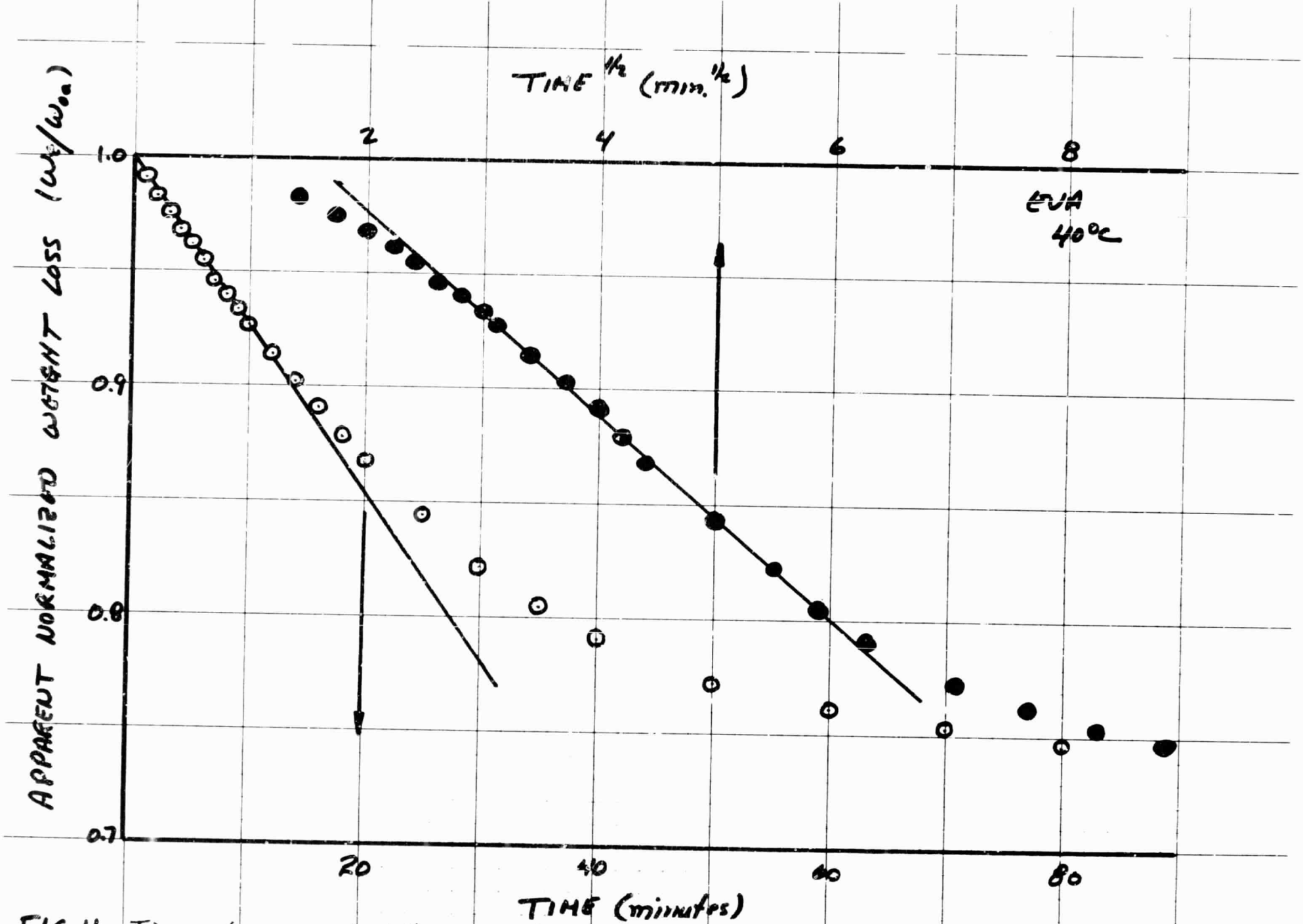

FIG. 11 — Time and square root of time dependencies of normalized weight loss in EVA due to water desorption at 40C

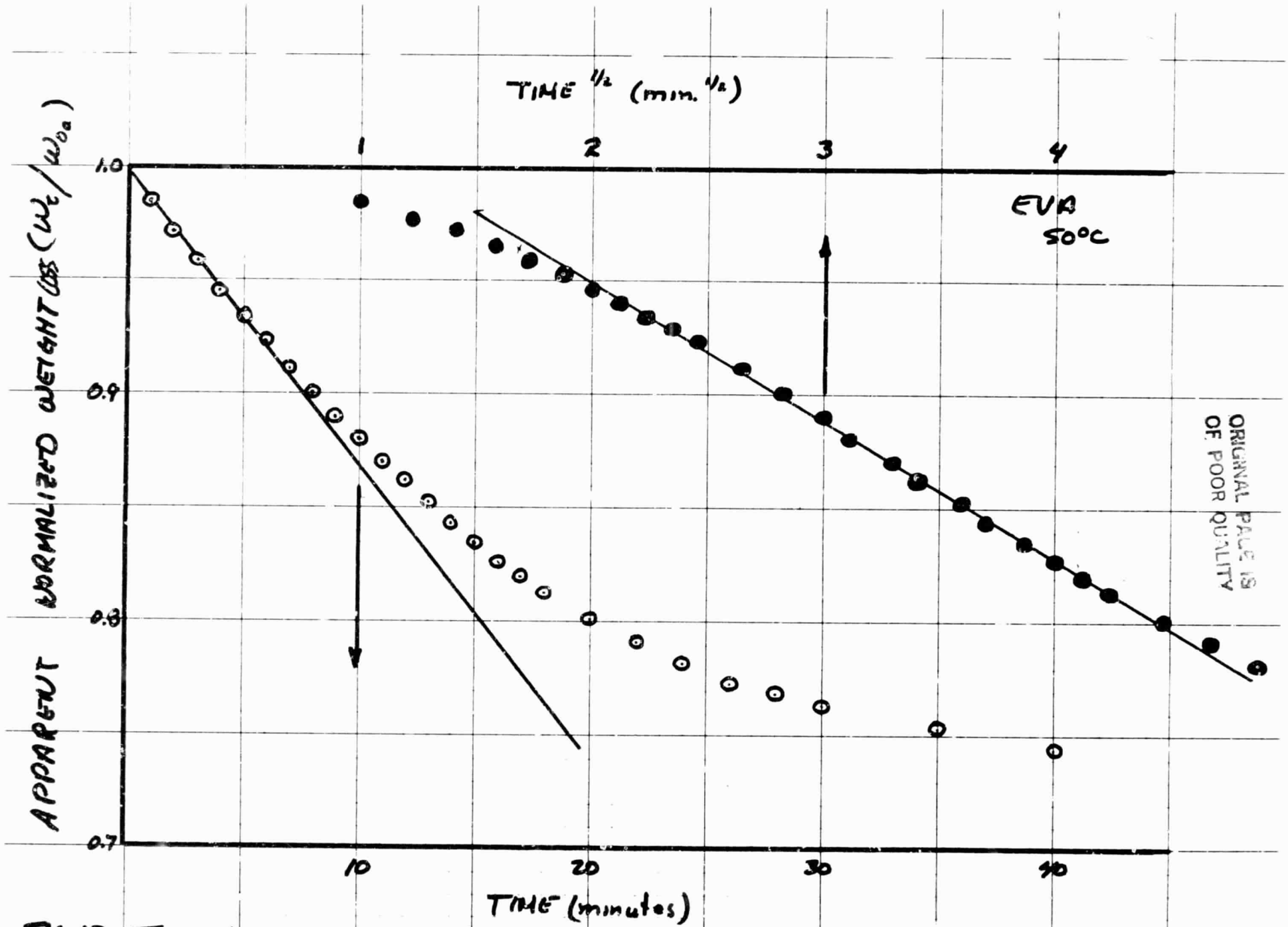

FIG. 12— Time and square root of time dependencies of normalized weight loss in EVA due to water desorption at 50°C

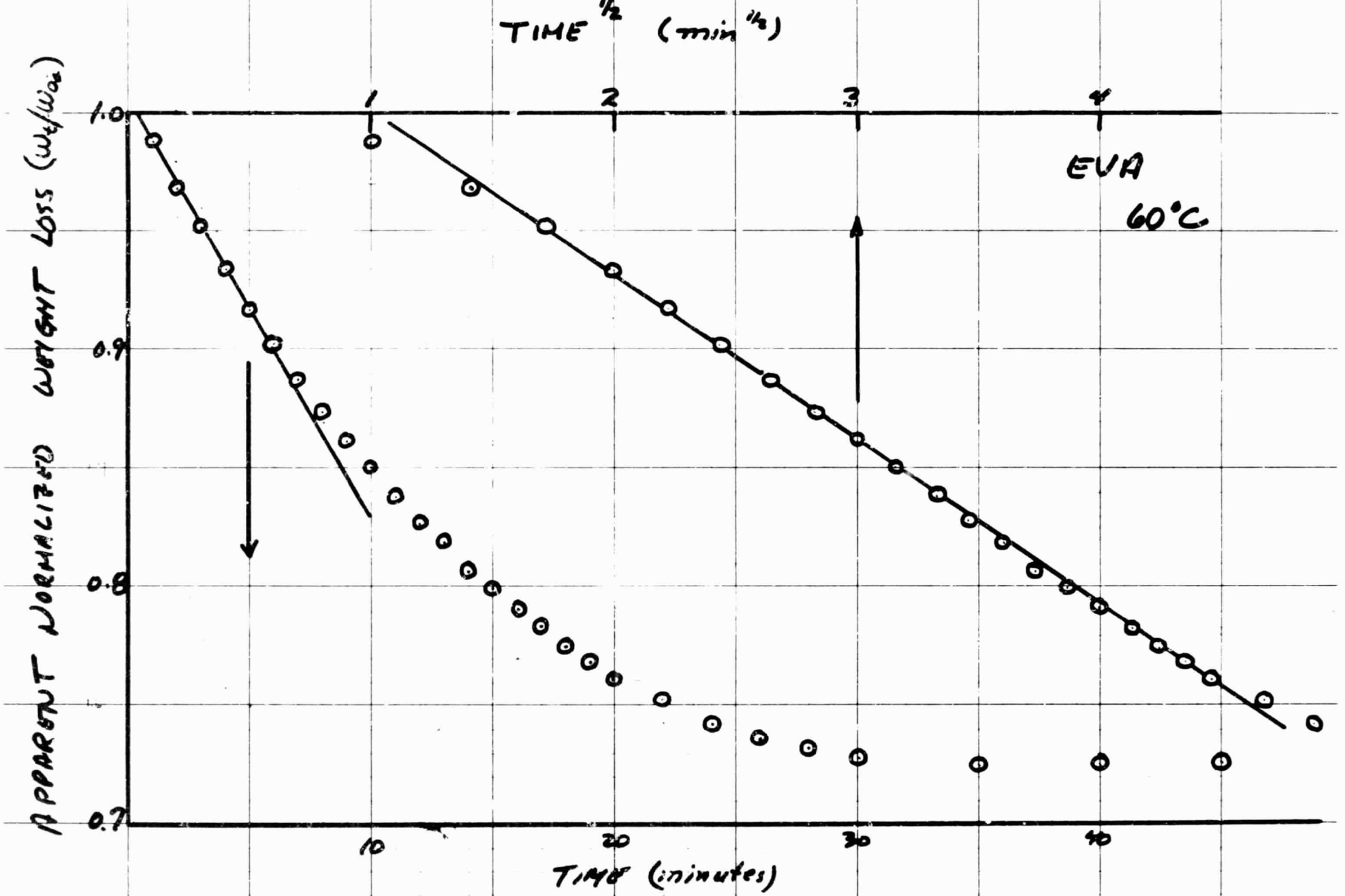

FIG. 13 — Time and square root of time dependencies of normalized weight loss in EVA due to water desorption at 60°C

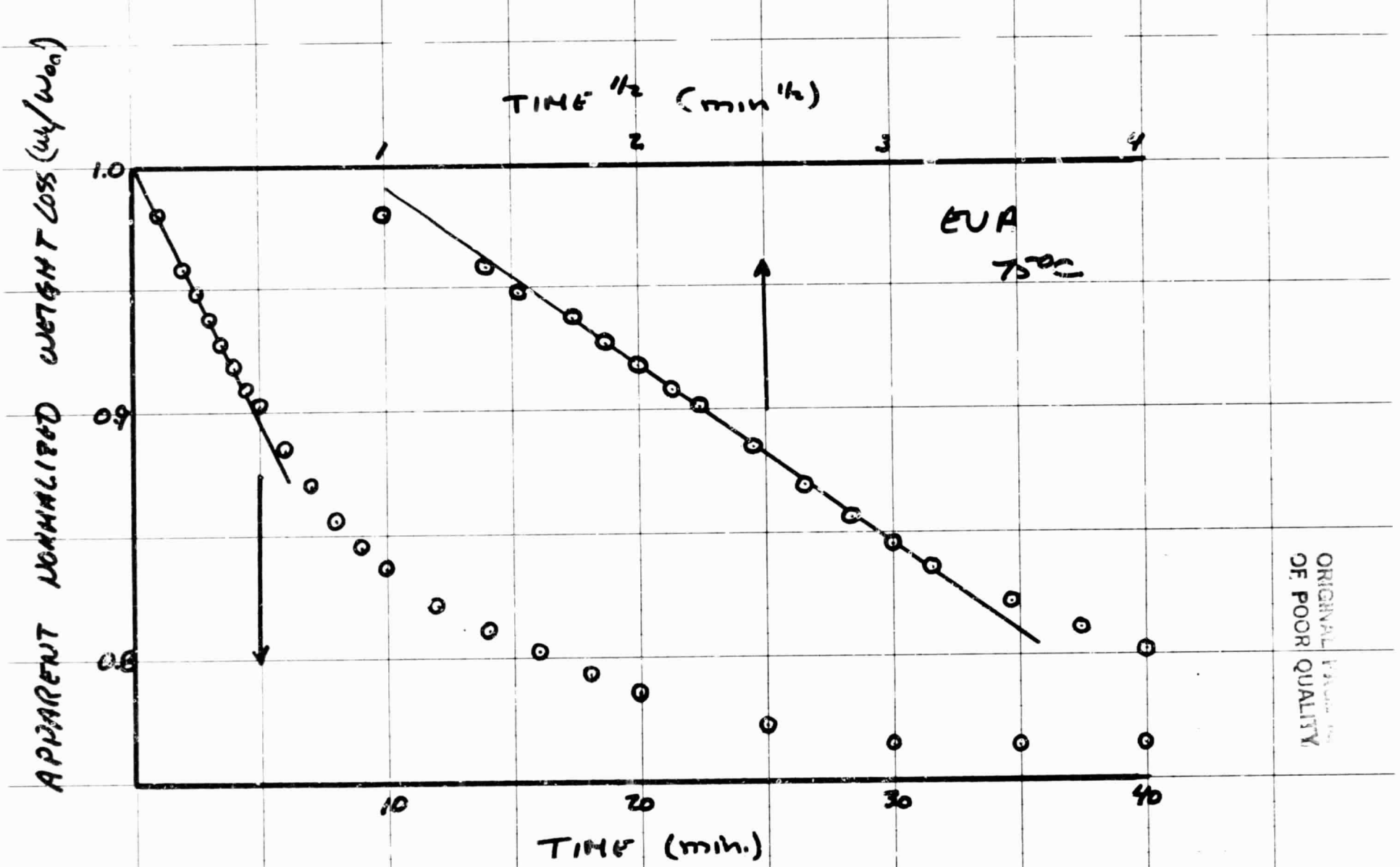

FIG. 14 — Time and square root of time dependencies of normalized weight loss in EVA due to water desorption at 75°C

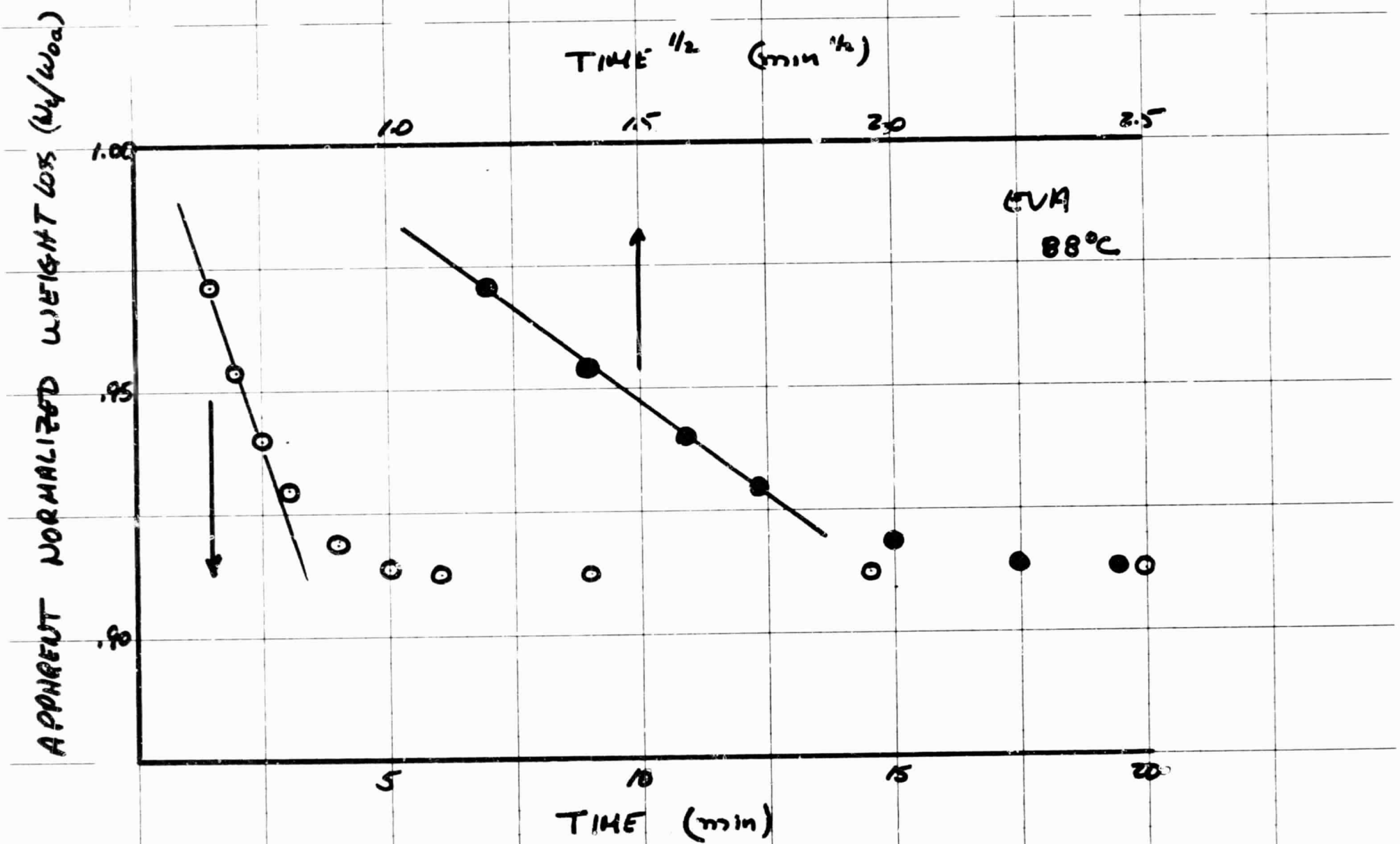

FIG. 15 - Time and square root of time dependencies of normalized weight loss in EVA due to water desorption at 88°C

WATER ABSORPTION MODEL

SEQUENTIAL REACTION STEPS:

STEP 1: CONDENSATION OF ATMOSPHERIC WATER AS A MONOLAYER ON SURFACE

REACTION: H_2O (in atmosphere) ⟶ H_2O (monolayer on surface)

SCHEMATIC ILLUSTRATION:

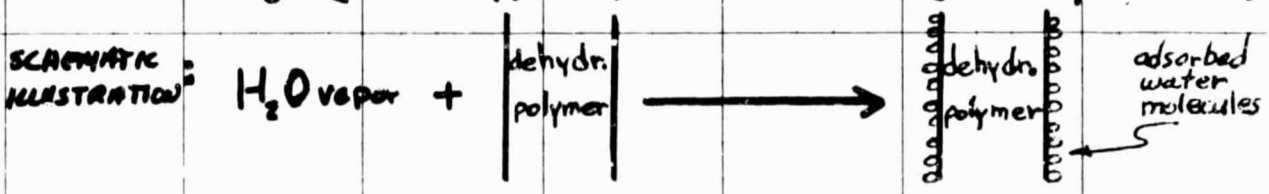

STEP 2a: CONDENSATION OF SUCCESSIVE MONOLAYERS TO FORM A SURFACE FILM

REACTION: H_2O (in atm.) + H_2O (monolayer) ⟶ H_2O (surface film)

SCHEMATIC ILLUSTRATION:

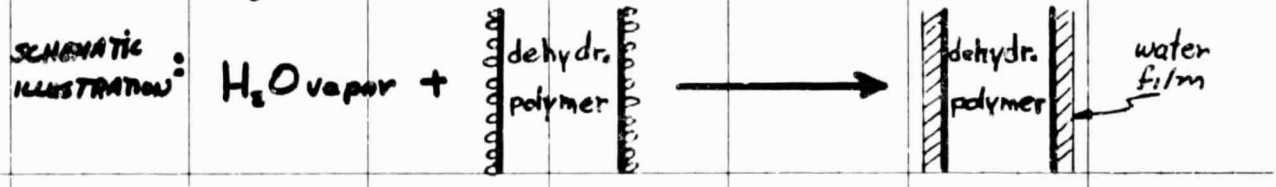

STEP 2b: DIFFUSION OF MONOLAYER INTO POLYMER

REACTION: H_2O (monolayer on surface) ⟶ H_2O (in polymer)

SCHEMATIC ILLUSTRATION:

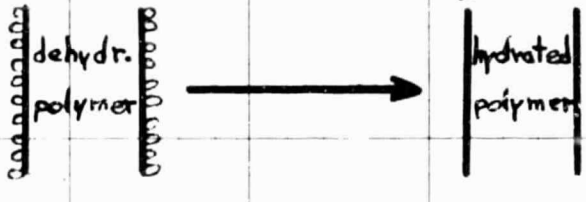

OVERALL REACTION: H_2O (in atmosphere) ⟶ H_2O (in polymer and in surface film)

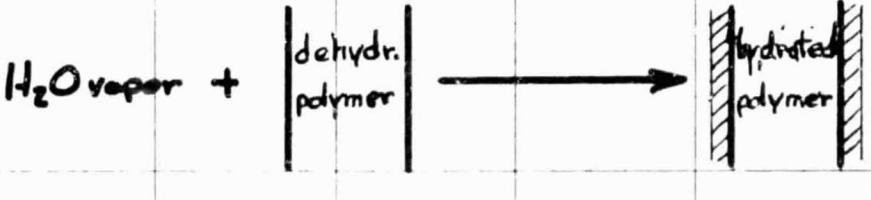

FIG. 16 – Schematic illustrations of reaction equations for water absorption in EVA

WATER DESORPTION MODEL

SEQUENTIAL REACTION STEPS:

STEP 1: EVAPORATION OF THE ADSORBED WATER FILM ON SURFACE

REACTION: H_2O (in polymer and in surface film) $\longrightarrow$ H_2O (in polymer) + H_2O (in atm.)

SCHEMATIC ILLUSTRATION:

STEP 2: VOLUME DIFFUSION OF WATER OUT OF POLYMER TO SURFACE

REACTION: H_2O (in polymer) $\longrightarrow$ H_2O (monolayer on surface)

SCHEMATIC ILLUSTRATION:

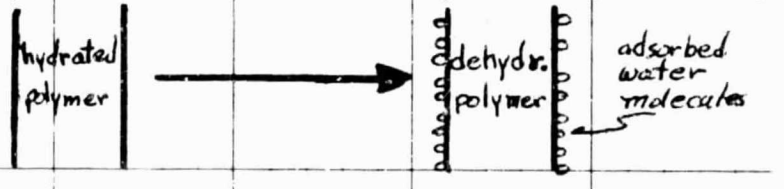

STEP 3: EVAPORATION OF WATER MONOLAYER ON SURFACE

REACTION: H_2O (monolayer on surface) $\longrightarrow$ H_2O (in atmos.)

SCHEMATIC ILLUSTRATION:

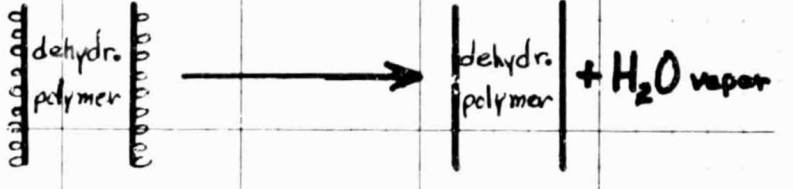

OVERALL REACTION: H_2O (in polymer and in surface film) $\longrightarrow$ H_2O (in atmos.)

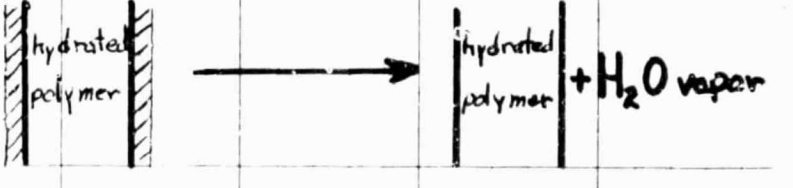

FIG. 17 - Schematic illustrations of reaction equation for water desorption in EVA

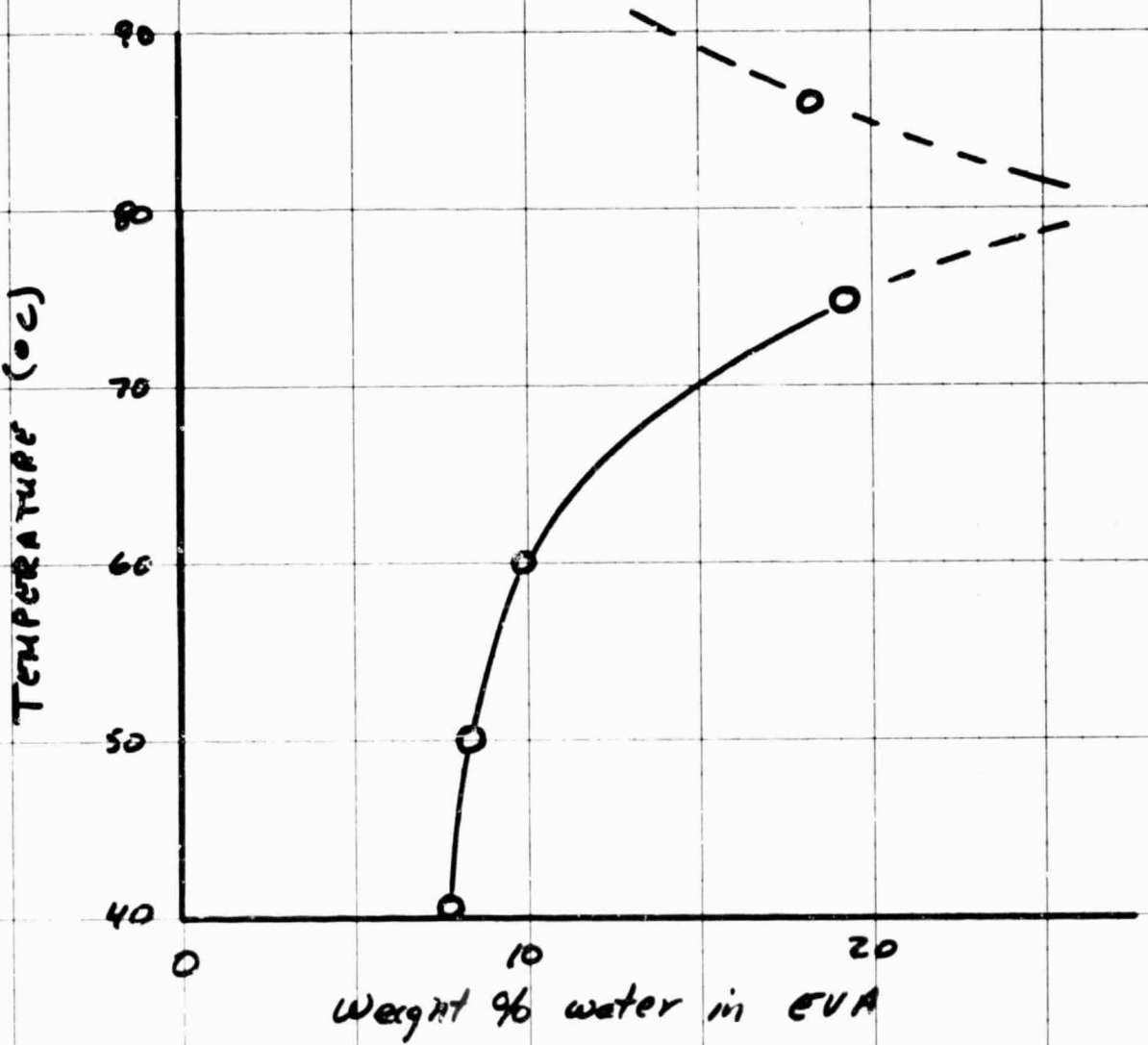

FIG. 18 — Partial phase diagram for the binary H_2O-EVA system where the solubility limit of H_2O in EVA as a function of temperature is shown

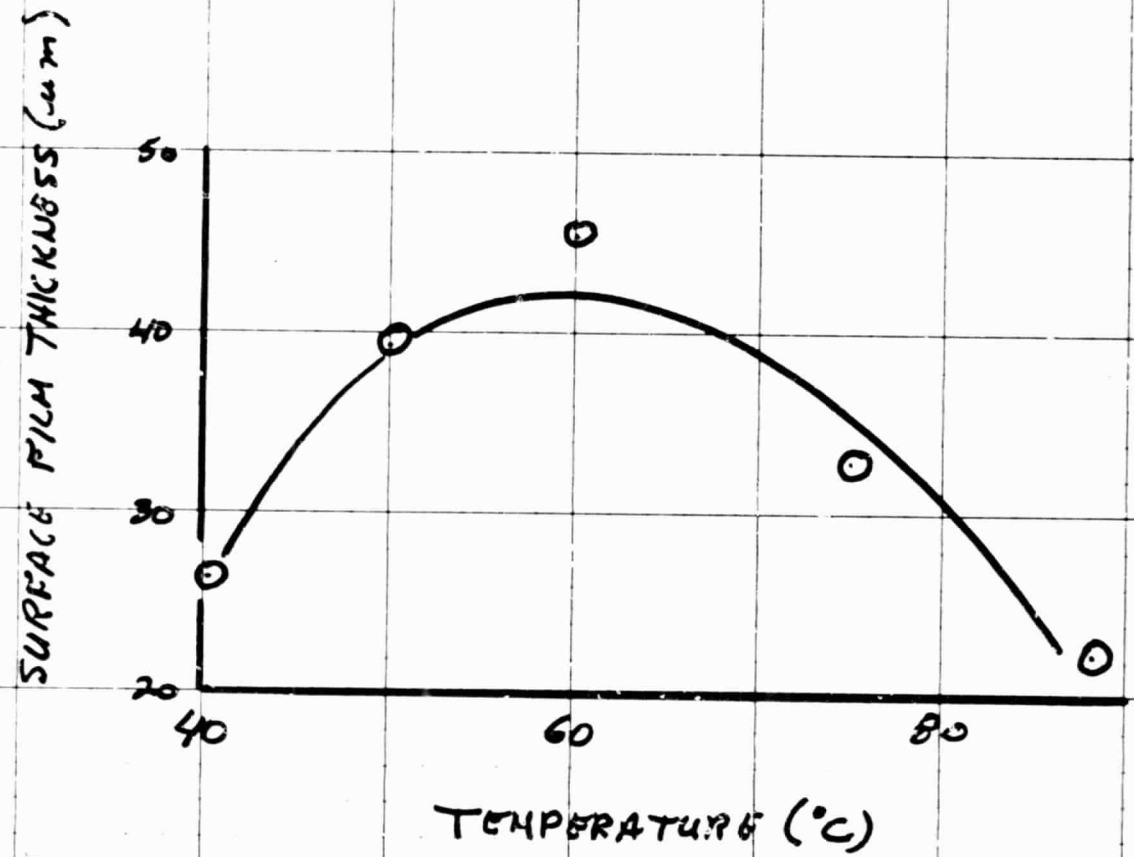

FIG.19 – Equilibrium thickness of adsorbed water film on EVA as a function of temperature.

CONDEUSATION

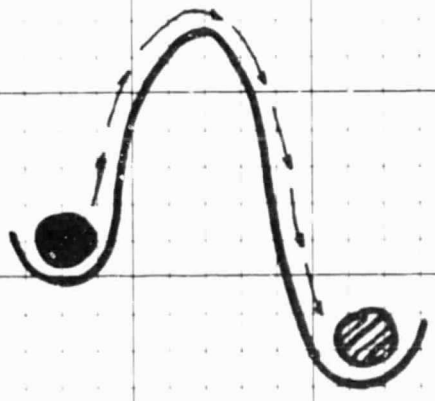

EVAPORATION

FIG. 20 – Schematic illustration of energy barrier for condensation and evaporation reactions during the Stage I kinetic response in water absorption and desorption on EVA

III. UV Light Effects on Water Absorption in PVB and EVA

Gravimetric techniques were employed to monitor the influence of UV radiation on the water asborption kinetics of PVB and EVA. The normalized weight response of plasticized PVB samples in a 100% humid environment at 75° and 50° C while being exposed to UV radiation is shown in Figure 1. For comparative purposes, the normalized weight response for non-irradiated PVB samples exposed to the same temperature/humidity environment is also shown in Figure 1. The experiemental arrangement proved to be awkward, and a considerable amount of scatter in the data was evident. Even with this uncertainty, the data clearly showed that non-irradiated PVB samples gained much more weight than the UV-irradiated samples. The other feature evident in the data is that at longer exposure times, the UV-irradiated samples lost weight. The implications of these data is that an exposure to UV light will hinder the water absorption characteristics of PVB and will accelerate the kinetics of plasticizer loss in PVB. These tentative conclusions are partially supported by simple observations of the samples after terminating the experiements. The non-irradiated samples had a non-transparent cloudy appearance which is typical of PVB containing a large amount of water. The UV-irradiated samples remained transparent throughout the entire experimental run, indicating that very little water was absorbed. After the runs were terminated, another noticeable distinction was apparent between the irradiated and nonirradiated samples. The UV-irradiated samples collapsed around the wire support picture frame across which they had been attached, while non-irradiated samples remained intact, stretched across the frame. Apparently, the PVB samples after UV light exposure at 100% humidity and temperatures in excess of 50°C, lost a considerable amount of strength as a probable result of chain scission by the UV light. The collapsed UV-irradiated PVB samples were soft and flexible indicating that chain scission could have occured or that the amount of plasticizer loss is these samples was minimal. A summary of the

contrasting characteristics between the irradiated and non-irradiated PVB samples is presented in Table I.

The water absorption characteristics of UV-irradiated and non-irradiated EVA at 75°C and 100% humidity are shown in Figure 2. The scatter in the data is again uncomfortably large, but the results clearly demonstrate that EVA absorbs a relativity small amount of water while it is being radiated with UV light, compared to the amount of water absorbed by the non-irradiated EVA sample. A visual comparison of the irradiated and non-irradiated EVA samples after terminating the experimental run did not reveal any distinguisable differences between the samples in their transparency or mechanical characteristics (Table I).

Table I

Characteristics of EVA and PVB samples after a 50 hour exposure to 100% humidity at temperature above 50°C

	UV-irradiated PVB	non-irradiated PVB	UV-irradiated EVA	non-irradiated EVA
color	transparent	cloudy	transparent	transparent
strength	weak	strong	strong	strong
water absorption	small	large	small	large

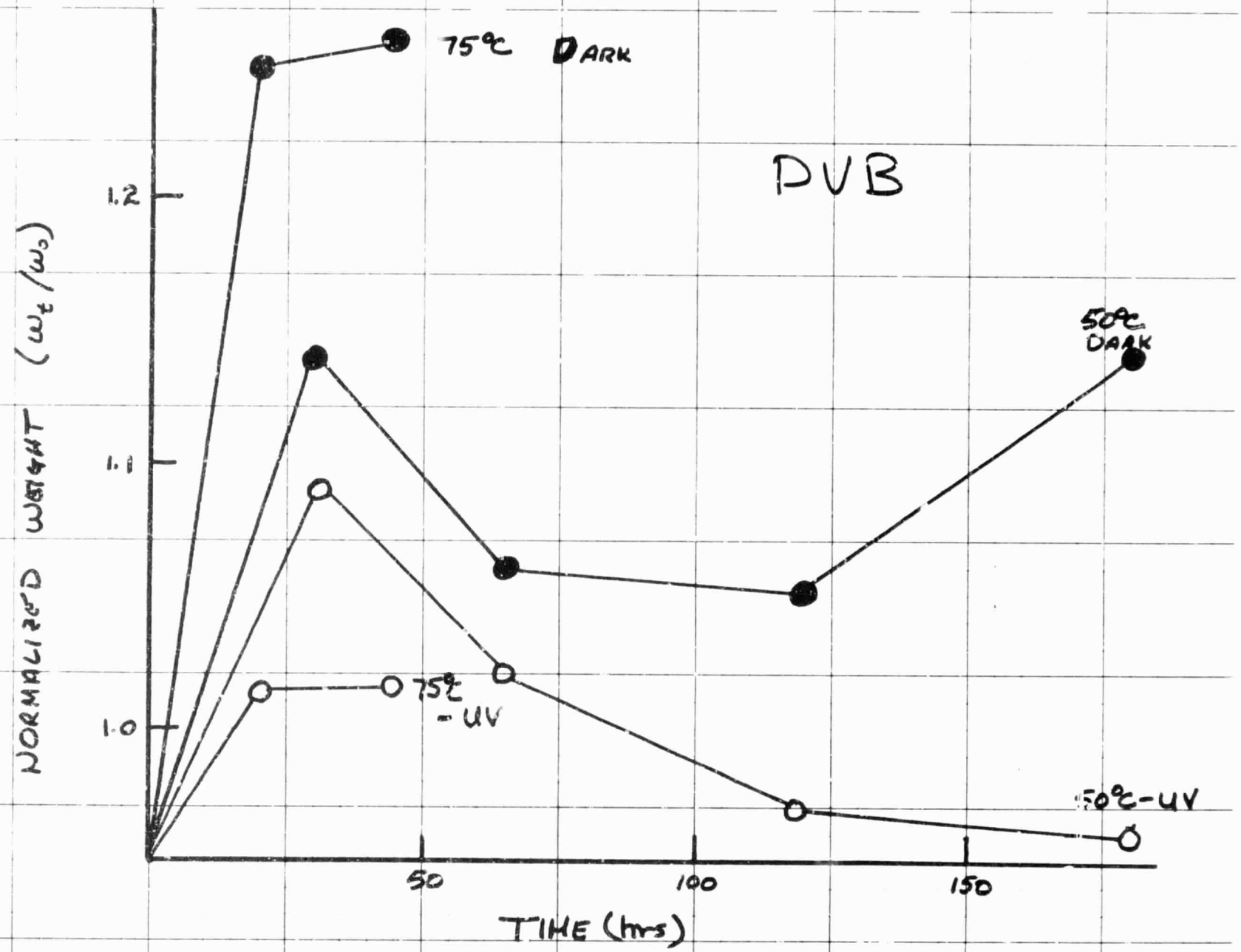

FIGURE 1 — Time dependence of normalized weight gain due to water absorption in PVB samples during UV light exposure and in unexposed PVB samples

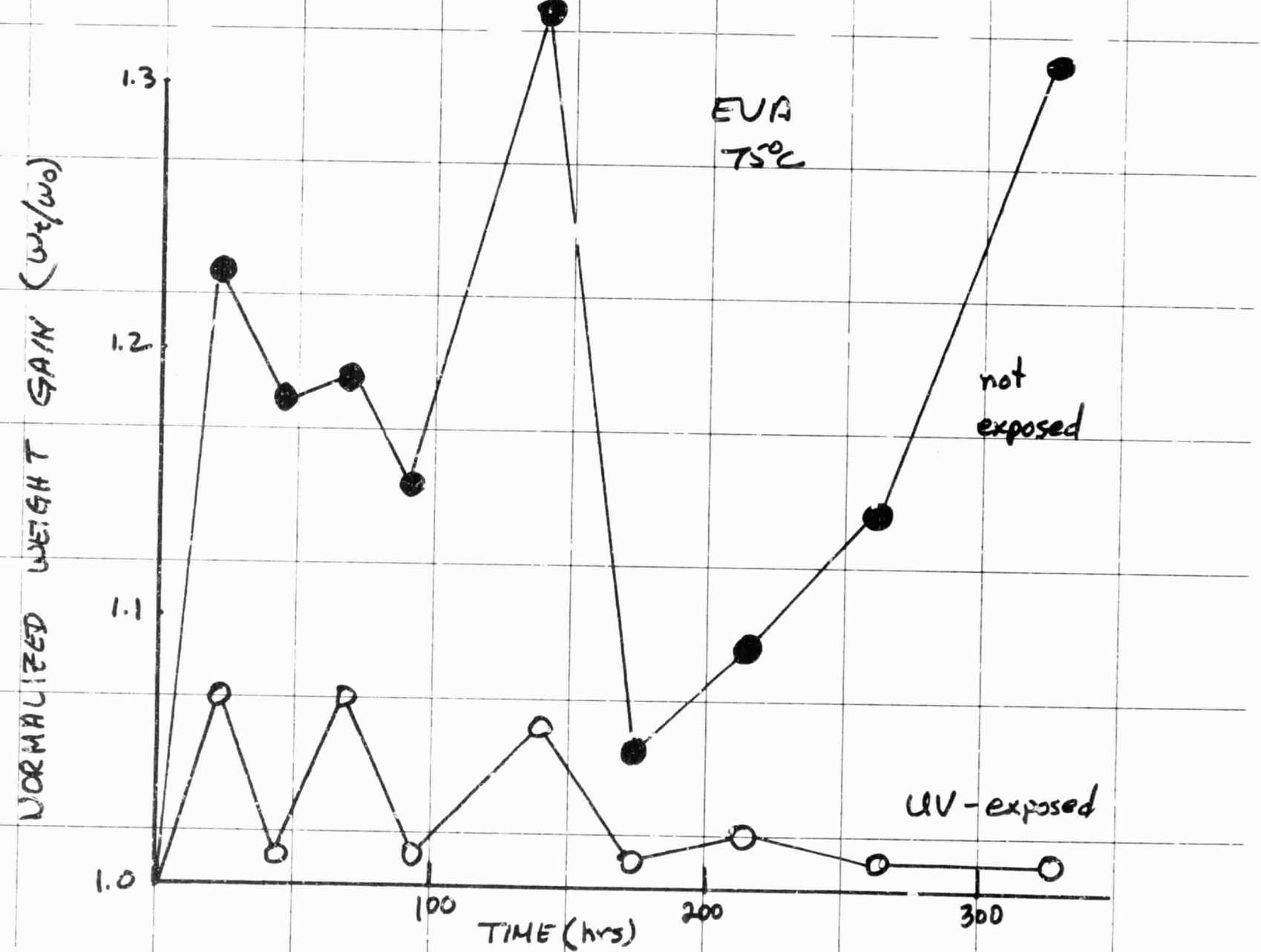

Figure 2 - Time dependence of normalized weight gain due to water absorption in an EVA sample during UV light exposure and in an unexposed EVA sample

IV. Influence of Plasticizer on Water Absorption in PVB

Previous progress reports showed that the plasticizer in PVB has an enormous influence on the resistivity. The plasticizer is also expected to influence the water absorption characteristics of PVB since plasticized PVB is expected to accommodate about 10 weight percent water while the unplasticized PVB in the absorption studies (May Progress Report) appears to saturate at a normalized weight of about 2.0 which corresponds to a 50 weight percent composition.

The water absorption characteristics of unplasticized PVB and plasticized PVB were evaluated. Samples of both materials were immersed in water at 25°C and the weight gain characteristics were monitored periodically over a time span of 500 hours. The results are shown in Figure 1. The unplasticized PVB absorbs considerably more water than the plasticized PVB. This result suggests that the plasticizer occupies an excludable volume in the PVB, and when the plasticizer is removed, this excludable volume can be occupied by water. Experimentally observed numbers appear to support this suggestion. Thirty weight percent of PVB is plasticizer, and plasticized PVB can absorb about 10 weight percent water. On an excludable volume-wight percent basis, unplasticized PVB would be expected to accommodate up to 40 weight percent water which is in reasonable agreement with the observed 50 weight percent saturation value. The numbers appear to add up correctly but there is no fundamental reason why they should.

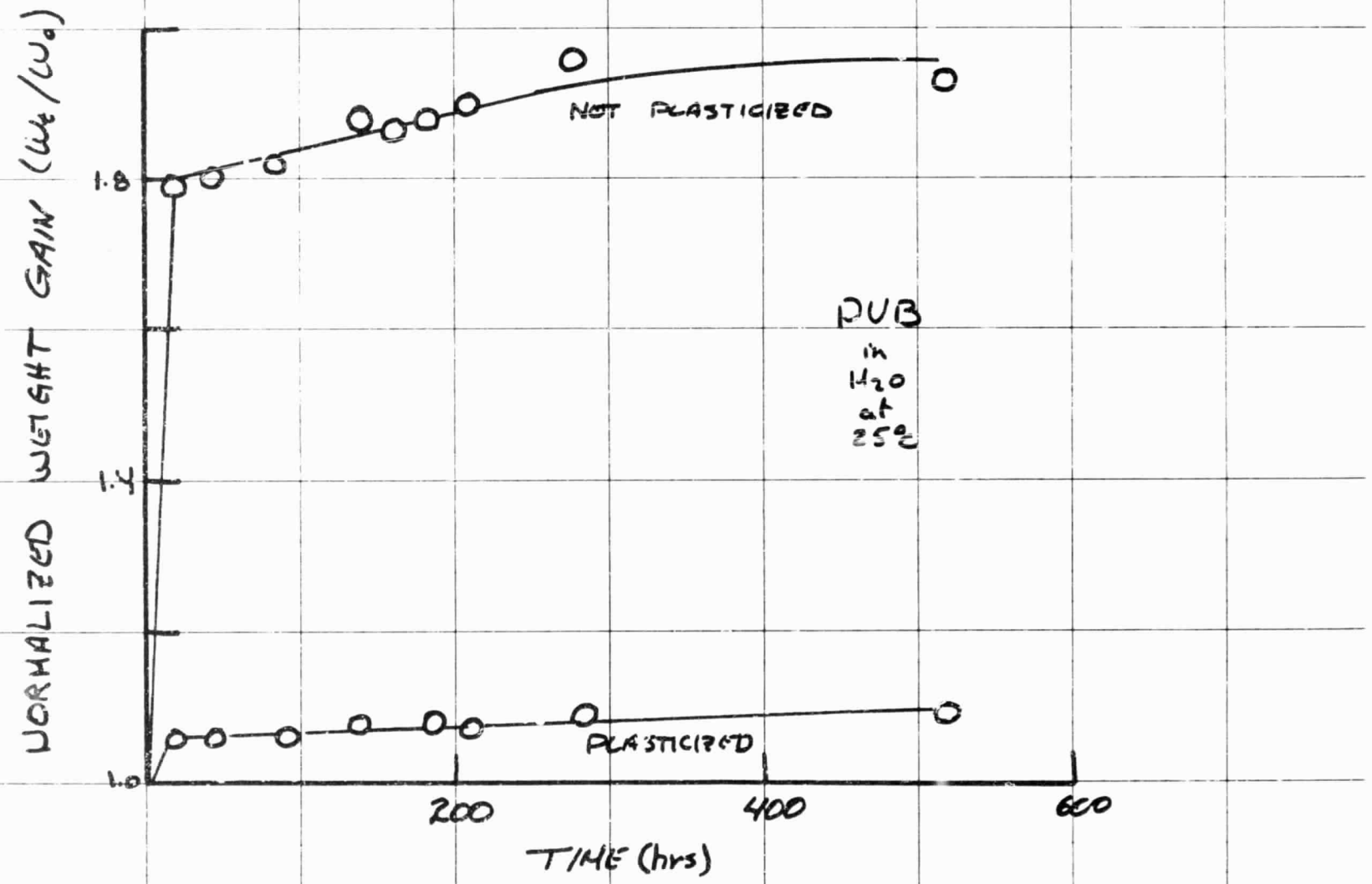

Figure 1 — TIME DEPENDENCE OF THE NORMALIZED WEIGHT GAIN DUE TO WATER ABSORPTION IN PLASTICIZED AND UNPLASTICIZED PVB SAMPLES

V — CORROSION EFFECTS IN SOLAR CELLS

A systematic study of corrosion effects in solar cells was initiated. A previous investigation indicated that corrosion in solar cells results from three major causes:

(i) Intracell galvanic action corrosion -- The composite structure of dissimilar materials: (metallization layers, anti-relection coating, silicon subststrate) in ohmic contact on a single cell will result in corrosion effects on that cell provided the encapsulating polymer can serve as an electrolyte.

(ii) Intercell impressedvoltage corrosion -- The potential differences that must exist between adjacent cells in an illumiated array, makes one solar cell anodic relative to its cathodic neighbor. In the presence of an electrolytic encapsulating polymer, the resulting oxidation reaction at the anodic solar cell is corrosive while the associated reduction reaction at the cathodic solar cell can result in plating. Both reactions are expected to degrade the output characteristics of their respective solar cells.

(iii) Intercell diode current corrosion -- The current that flows through the solar cells anjunction diode structure as a result of illumination can be corrosive on each individual cell as a result of the IR potential drop that must exist across each cell.

The ultimate questions to be resolved in a study of corrosion effects in solar cells are: What is the relative magnitude of each of these corrosion causing effects and how can these effects be minimized to obtain reliable-long lifetime cells?

The initial study attempts to evaluate the influence of each of these corrosion causing effects on the I-V characteristic response curves of the illuminated cells and on the visual physical features of the cells. Figure 21 illustrates the experimental arrangements used to separate and evaluate each corrosion effect. Arrangement #4 represents a single solar cell. When this cell is immersed in an electrolyte, the galvanic corrosion effect only is occurring and being evaluated in this

experimental arrangement. In arrangement #3, a single solar cell is forward biased to produce a diode current through the cell. When immersed in an electrolyte, both galvanic action and diode current corrosion effects are activated. A comparison of the corrosion characteristics of the cells in arrangements #3 and #4 yields the diode current corrosion effect. Arangement #2 consists of two solar cells properly connected to a power supply so a potential difference exists between the cells but no didode current flows through the cells. When immersed in an electrolyte, only a corrosion current flows between the cells.

A comparison of the corrosion characteristics of the cells in arrangements #2 and #4 give the impressed voltage corrosion effect at an anodic and a cathodic cell. Arrangement #1 is used to simulate actual corrosion conditions in solar cell arrays where all three corrosion effects are present. The solar cells used in these studies were supplied by ASEC.

The corrosion testing consisted of immersing one set of cells in these four arrangements, in water as an electrolyte at 25°C. Another set was encapsulated in EVA and then immersed in water at 85°C. The cells were allowed to corrode for 120 hours. During the corrosion time, the solar cells were removed occasionally from the bath and their I-V characteristic response curves were evaluated. The normalized short circuit response as a function of corrosion time is shown in Figures 22 and 23 for a qater electrolyte and a EVA electrolyte respectively. A visual inspection of the cells after the 120 hour corrosion treatment revealed a number of effects caused by the corrosion treatment. These effects for the various corrosion conditions are presented in Table V. A careful comparative examination of Table V and Figures 22 and 23 indicates that the intracell galvanic effect is not a major contributor to corrosion in solar cells. In general, the intracell diode current effect does not appear to be dominantly instrumental in causing corrosion degradation of the cells. Corrosion appears to result mostly from potential differences between adjacent cells. These conclusions are tentative since there was no real definitive trends apparent in the data, and since several cells were apparently of poor quality and went bad almost immediately during corrosion testing. One trend apparent when comparing Figure 22 with Figure

23, is that the cells in EVA degraded significantly faster than the cell tested in water. The only apparent reason for this behavior is that EVA with its absorbed water may be a more hostile electrolytic environment than water. A simple pH test appears to confirm this suggestion. A sample of EVA was placed in a beaker of water for three months. The pH of the water was originally 6.7 and after three months the ph was 6.2. A similar test using a PVB sample resulted in a final ph of 4.5 Table VI. Apparently water absorbed in EVA or PVB can be acidic, and corrosive to solar cells.

Corrosion Conditions	Corrodes (C) or Undermines (U) Grid Metalliz.	Attacks AR Coating	Discolors Backside Metalliz.	Lifts Backside Metalliz.
EVA ENCAPSULATED				
Galvanic, diode & voltage (anode)				X
Galvanic, diode & voltage (cathode)		X		X
Galvanic & voltage (anode)		X		X
Galvanic & voltage (cathode)		X		X
Galvanic & diode				
Galvanic				
NOT ENCAPSULATED (IN WATER)				
Galvanic, diode & voltage (anode)				
Galvanic, diode & voltage (cathode)				
Galvanic & voltage (anode)	X (U)		X	X
Galvanic & voltage (cathode)				
Galvanic & diode	X (C)	X	X	
Galvanic				

TABLE V.

Visual characterization of various corrosion effects in EVA encapsulated and water immersed solar cells.

	pH
Original Water	6.7
Water after three months with immersed EVA sample	6.4
Water after three months with immersed PVB sample	4.5

TABLE VI

The influence of immersed EVA and PVB samples on the pH of water.

ARRANGEMENT #1

0.85v

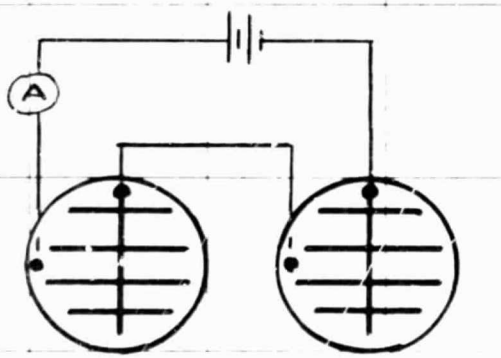

anode cathode

INTERCELL IMPRESSED VOLTAGE CORROSION; INTRACELL DIODE CURRENT CORROSION; AND INTRACELL GALVANIC CORROSION EFFECTS

$I = I_{diode} + I_{corrosion}$

ARRANGEMENT #2

0.85v

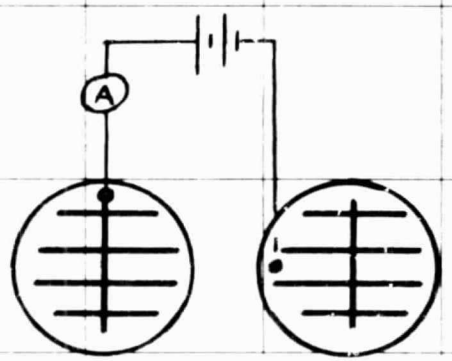

anode cathode

INTERCELL IMPRESSED VOLTAGE CORROSION AND INTRACELL GALVANIC CORROSION EFFECTS

$I = I_{corrosion}$

ARRANGEMENT #3

0.85v

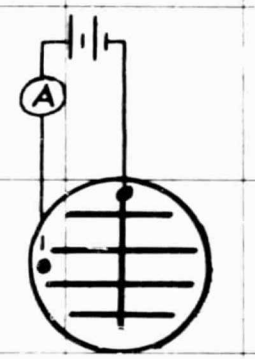

INTRACELL DIODE CURRENT CORROSION AND INTERCELL GALVANIC CORROSION EFFECTS

$I = I_{diode}$

ARRANGEMENT #4

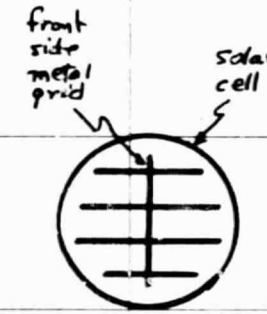

INTRACELL GALVANIC CORROSION EFFECT

$I = 0$

FIG. 21 – Biasing conditions of various solar cell arrangements for evaluating various corrosion effects.

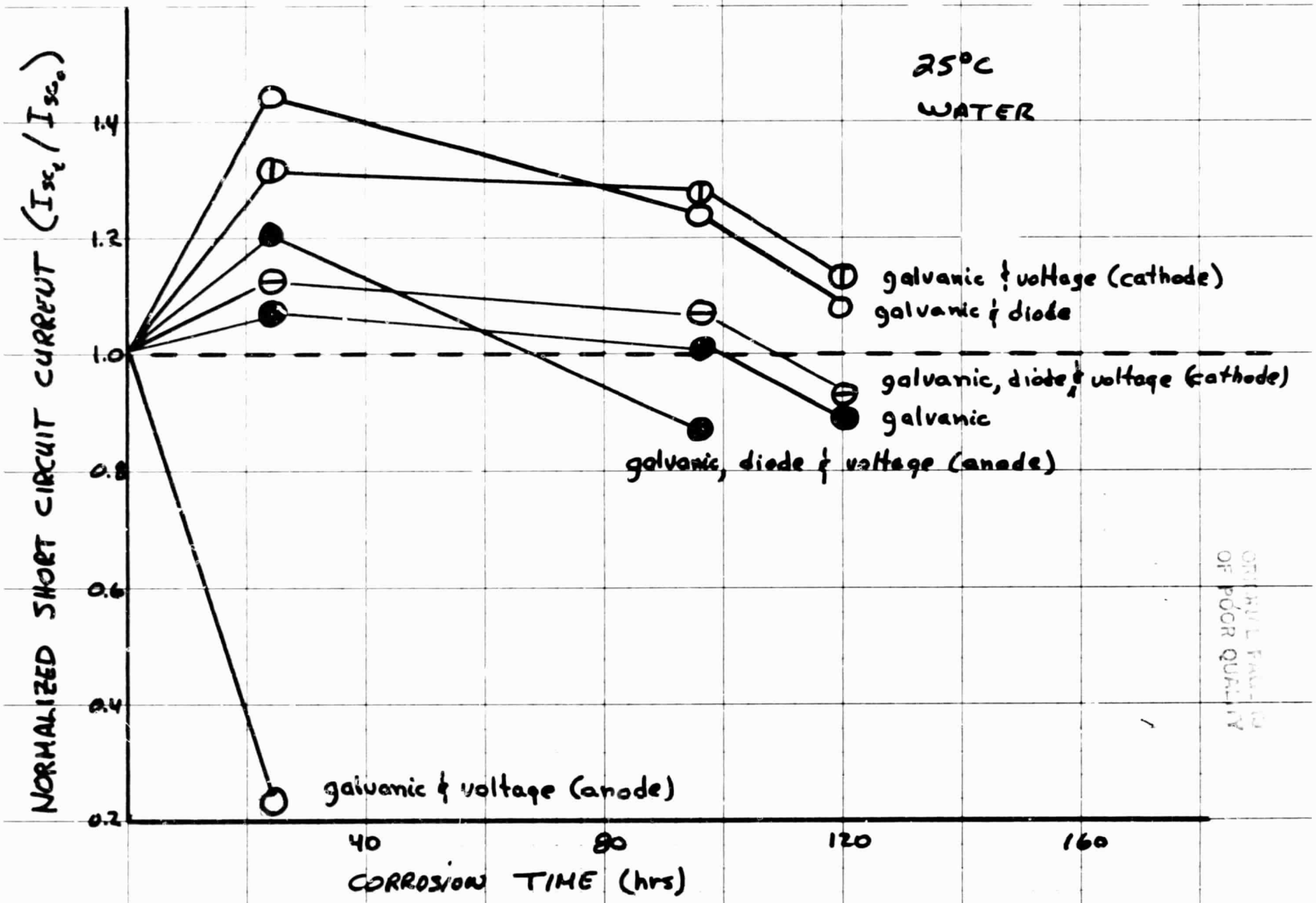

Fig. 22 – Normalized short circuit current as a function of corrosion time for solar cells subjected to the corrosion conditions of Fig. 21

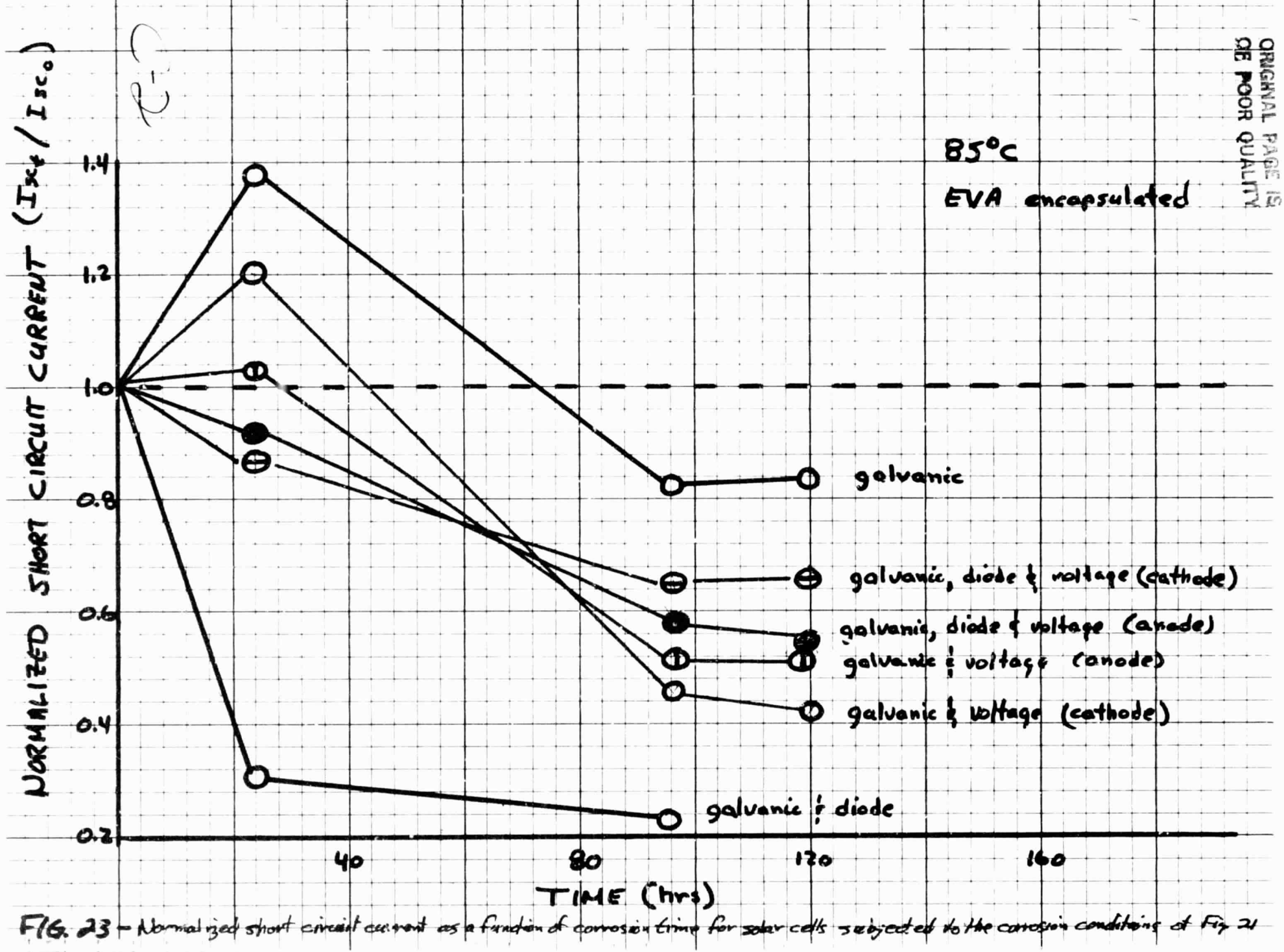

FIG. 23 – Normalized short circuit current as a function of corrosion time for solar cells subjected to the corrosion conditions of Fig 21